# Kinetics, mechanisms, and site requirements of olefin synthesis and conversion over metal oxide catalysts

A DISSERTATION
SUBMITTED TO THE FACULTY OF
UNIVERSITY OF MINNESOTA
BY

Joseph Francis DeWilde

IN PARTIAL FULFILLMENT OF THE REQUIREMENTS
FOR THE DEGREE OF
DOCTOR OF PHILOSOPHY

Adviser: Aditya Bhan

August, 2016

## *Acknowledgements*

Firstly, I would like to thank and acknowledge the tremendous effort put forth by my adviser, Aditya Bhan. He has always been patient with me and given helpful advice for the last 5+ years. His continued efforts to push me have made me develop into the scientist I am today. It has been a great pleasure to grow together, me as a researcher and him as a manager.

I would then like to acknowledge all of my former and current labmates: Samia Ilias, Elizabeth Mallon, Ian Hill, Mark Mazar, Srinivas Rangaragan, Sam Blass, Jeremy Bedard, Cha-Jung Chen, Minje Kang, Rachit Khare, Mark Sullivan, Udit Gupta, Anurag Kumar, Andrew Hwang, Linh Bui, Sukaran Arora, Brandon Foley, Wen-Sheng Lee, Dario Prieto, Mark Bachrach, and Praveen Bollini for all of their support and technical discussions throughout the years. I would also like to extend special thanks to Hsu Chiang and Jake Miller for being the two bookends for my time here by mentoring me and taking my work forward from now on, respectively. My undergraduate students, Christopher Ho, Christopher Czopinski, and Marcello Herrera deserve thanks as well for both their daily help around lab and for making me grow as a mentor and teacher. All of my classmates and friends, who are too numerous to list here, have supported me through times of stress and strife; this support has not gone unnoticed and I appreciate everything that they have given me.

I would also like to acknowledge my parents, Frank and Janice DeWilde; my brother, Robert Offutt; my close friends back in Oregon, Chris Germond and Josh Paul; and my new family, Pravin, Vandana, and Shruti Rangnekar for always keeping me grounded throughout my graduate education. Finally, I want my wife, Esha, to know how much she has meant to me for the last 4 years together. She has been my rock in the worst of times, my greatest source of joy in the best, and the most understanding person I know. I am excited to see where life takes us as we move forward to Michigan.

## *Dedication*

This thesis is dedicated to my wife, Esha, and parents, Janice and Francis DeWilde. Without their support, I could have never even begun to pursue my doctoral degree, much less successfully complete this body of work. I can never thank any of them enough for everything and I will carry their support throughout the rest of my ambitions in life. I would also like to dedicate this work to my adviser, Aditya Bhan. His continued encouragement of my work, challenges to my results, and faith in my abilities cannot be overstated.

## *Abstract*

We report the kinetics, mechanisms, and site densities of parallel ethanol dehydration and dehydrogenation over gamma-alumina ($\gamma$-$Al_2O_3$), a high surface area and thermally-stable metal oxide used both as a catalyst support and as a Lewis acid catalyst in industrial practice. We further extend our investigations to diethyl ether conversion over $\gamma$-$Al_2O_3$ to describe the reaction network for ethanol dehydration and dehydrogenation at conversions exceeding 10%.

Steady state measurements demonstrate that unimolecular and bimolecular ethanol dehydration rates are inhibited by water-ethanol co-adsorbed complexes at 488 K. Reactive surface intermediates, rather than co-adsorbed complexes, inhibit the rates of ethanol dehydration and dehydrogenation at industrially-relevant temperatures (>623 K). Co-processing pyridine with ethanol/water feed mixtures results in a reversible inhibition of both unimolecular and bimolecular ethanol conversion pathways; the synthesis rates of ethylene and acetaldehyde are inhibited to a greater extent than diethyl ether synthesis rates, establishing that unimolecular reactions occur on a pool of catalytic sites separate from the pool for bimolecular dehydration reactions. An observed 1:1 ratio of acetaldehyde and ethane in the eluent verifies that ethanol dehydrogenation proceeds via a hydrogen transfer mechanism.

We employ asymmetric ethers as probes to establish ether conversion on $\gamma$-$Al_2O_3$ occurs through a disproportionation pathway to form an olefin and an alcohol, rather than through a hydration pathway. Diethyl ether disproportionation rates were verified to (i)

possess an intrinsic rate constant that is within a factor of two of that of unimolecular ethanol dehydration and (ii) be inhibited by pyridine to the same extent as ethylene synthesis rates from ethanol dehydration. These observations are consistent with a proposed mechanism in which ether disproportionation and unimolecular alcohol dehydration occur through a common alkoxide reaction intermediate and on a common pool of catalytic sites. Our combined investigations of alcohol and ether conversion establish the existence of two distinct pools of catalytic centers, verify all unimolecular pathways of alcohol dehydration, dehydrogenation, and ether disproportionation occur on a common set of active sites, and provide a rigorous kinetic description of these pathways.

*Table of Contents*

## *List of Tables*

## *List of Figures*

# *Chapter 1: Introduction*

## 1.1 Ethanol conversion on $\gamma$-$Al_2O_3$

Gamma-alumina ($\gamma$-$Al_2O_3$) is a versatile, low cost, and industrially-ubiquitous solid acid catalyst and catalyst support[1,2]. Morterra and Magnacca[3] observed three infrared (IR) absorption bands at 1598, 1610-1620, and 1625 $cm^{-1}$ on $\gamma$-$Al_2O_3$ that was exposed to pyridine at ambient temperature; these bands were assigned to pyridine adsorbed onto surface aluminum atoms with a diversity of coordination environments. Similarly, three broad IR absorption bands (2195-2210, 2215-2220, and 2235-2240 $cm^{-1}$) attributed to CO bound onto different families of surface aluminum atoms occupying exposed tetrahedral lattice positions were measured on $\gamma$-$Al_2O_3$ samples dosed with CO at 300 K[3]. Wischert et al.[4] used Density Functional Theory (DFT, PW91 functional) to model the fully-dehydrated $\gamma$-$Al_2O_3$ surface and established that at least five different types of surface Al-O moieties are stable on the (110) surface facet alone, each with distinct water adsorption energies ranging between -125 and -226 kJ $mol^{-1}$. These spectroscopic and theoretical studies reveal that the surface of $\gamma$-$Al_2O_3$ is complex with a diversity of surface aluminum center environments, but do not verify the relevance of these centers during catalysis. Herein, we employ probe reactions and in-situ chemical titrations to investigate the surface complexity of $\gamma$-$Al_2O_3$ during reaction, overcoming the limitations of traditional ex-situ characterization techniques.

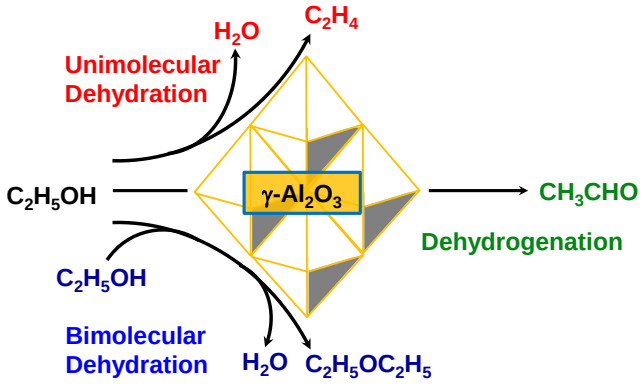


**Figure 1.** Schematic of the reaction pathways of ethanol on $\gamma$-$Al_2O_3$.

Acidic metal oxide catalysts, such as $\gamma$-$Al_2O_3$, are capable of selectively dehydrating alcohols to synthesize ethers and olefins[5-7]; specifically, ethanol dehydrates through a bimolecular pathway to produce diethyl ether (DEE) and through a unimolecular pathway to synthesize ethylene (Figure 1). Ethylene possesses a larger industrial demand than any other organic compound and is commonly used as a chemical platform for the syntheses of a number of consumer products, such as polymers, detergents, surfactants, and lubricants[8,9]. We, therefore, have selected ethanol conversion as the probe reaction used to investigate the surface complexity of $\gamma$-$Al_2O_3$.

The dehydration of alcohols on $\gamma$-$Al_2O_3$ has been studied for over five decades, led historically by Knözinger et al.[5,10-25] This body of work, however, is lacking in a mechanistic summary that can describe the simultaneous (i) 0-0.5 order alcohol and (ii) negative order water pressure dependencies of both the unimolecular and bimolecular dehydration rates for cyclohexanol, 1-propanol, and 2-propanol over $\gamma$-$Al_2O_3$ below 500 K[5,11-13,26]. Rate equations have been proposed to fit these observed dependencies but are empirical and incorporate terms with no physical interpretation[5,26]. Furthermore, the exact identity of the inhibitory water surface species is not fully detailed. We resolve these shortcomings by using in-situ titrations and kinetic measurements to determine that the

active sites for the two parallel dehydration reactions over γ-$Al_2O_3$ are (i) not equivalent and (ii) both inhibited by alcohol-water multimer complexes at 488 K, describing the simultaneous 0-0.5 alcohol and negative water reaction orders for both dehydration pathways.

In addition to dehydration, γ-$Al_2O_3$ also catalyzes the dehydrogenation of alcohols (Figure 1) to form aldehydes with low selectivities (<1.5% at 493 K)[27-29]. Acetaldehyde was observed to suppress the dehydration of ethanol on acidic catalysts (H-ZSM-5/γ-$Al_2O_3$) when added to the reactant feed (15 mol% of acetaldehyde in ethanol)[30]. Furthermore, acetaldehyde-dosed H-ZSM-5 samples exhibit broad IR bands ascribed to oligomerized species in spectroscopic measurements by Diaz and Gonzo[31], demonstrating the formation of bulky coke precursors capable of covering the catalyst surface. Given that this is problematic for the selective production of ethylene, we also investigate the mechanisms and site requirements of acetaldehyde synthesis from ethanol dehydrogenation over γ-$Al_2O_3$. Steady state kinetic measurements verify that only reactive precursors cover the dehydrogenation catalytic sites at temperatures >623 K, while in-situ chemical titrations reveal that dehydrogenation and unimolecular dehydration occur on the same pool of surface sites. We propose an indirect hydrogen transfer mechanism for ethanol dehydrogenation consistent with a measured 1:1 production of ethane and acetaldehyde in which ethylene is hydrogenated by surface hydrogen adatoms to regenerate the catalytic site. Recent DFT calculations (B3LYP exchange-correlation functional) estimate the activation barrier for the removal of surface

hydrogen adatoms formed from ethanol dehydrogenation over γ-$Al_2O_3$ to be 40 kcal $mol^{-1}$ for direct adatom desorption as hydrogen and 35 kcal $mol^{-1}$ if the adatoms were removed via ethylene hydrogenation[32], supporting our proposed mechanism.

No measurable quantities of ether were observed by Phung et al.[33] at complete conversion of ethanol over γ-$Al_2O_3$ at 623 K, revealing that γ-$Al_2O_3$ catalyzes ether conversion pathways at 623 K. Two potential ether conversion pathways have been proposed: (i) the disproportionation of the ether, synthesizing an alcohol and an olefin[16,33-35] and (ii) the reverse reaction of bimolecular alcohol dehydration, ether hydration. DEE conversion on γ-$Al_2O_3$ resulted in an ~1:1 ratio of ethylene and ethanol synthesis in steady state measurements by Morávek and Kraus[16] at 523 K, as well as by Phung and Busca[35] at 573 K, consistent with ether disproportionation being the dominant conversion pathway. Analysis of the mechanism and site requirements for ether disproportionation, however, is limited. In this work, we employ assymetric ethers to confirm that ether disproportionation is the prominent conversion pathway at industrially-relevant temperatures (>623 K). Steady state kinetic and in-situ pyridine inhibition measurements verify that DEE disproportionation and unimolecular ethanol dehydration occur on the same pool of sites and through a common ethoxide reaction intermediate.

## 1.2 Surface structure of $\gamma$-$Al_2O_3$

### *1.2.1 Bulk and Surface of $\gamma$-$Al_2O_3$*

X-ray Diffraction (XRD) measurements have classified $\gamma$-$Al_2O_3$ as a defective spinel with a near cubic closed packed arrangement of oxygen anions, consistent with its precursor parent structure of bohemite[36-39]. Classic spinels ($MgAl_2O_4$) possess a 3:4 cation:anion stoichiometry; the 2:3 cation:anion stoichiometry of $\gamma$-$Al_2O_3$, on the other hand, introduces an element of disorder for cation arrangement in the bulk lattice. As a result, XRD patterns of $\gamma$-$Al_2O_3$ display broad peaks[40]. In the bulk lattice of spinel structures, metal cations can be located in either octahedrally- or tetrahedrally-coordinated positions; Lee et al.[40] employed $^{27}$Al Nuclear Magnetic Resonance (NMR) spectroscopy and Monte Carlo simulations to ascertain (i) that the Al cations were arranged such that no long range order could be determined in their positions within the oxygen lattice and (ii) that, on average, 70% of the Al atoms were in octahedrally-coordinated lattice positions and the remainder occupied tetrahedral positions.

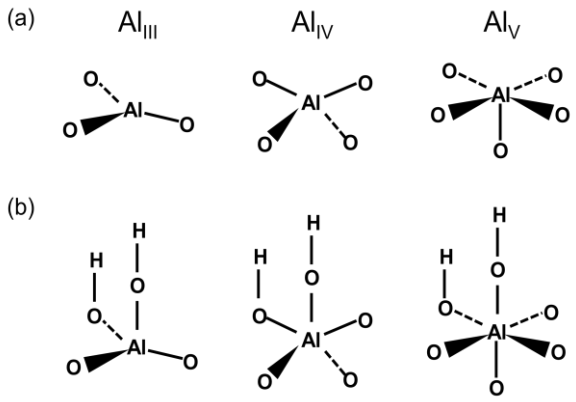


**Figure 2.** Schematic diagram of (a) the three-, four-, and five-coordinated aluminum surface sites of $\gamma$-$Al_2O_3$ and (b) hydroxyl groups formed from disassociation of water on the surface sites. Adapted from structures presented in[41,42].

Reactions occur on catalyst surfaces; therefore, characterization of solely the bulk material structure provides an incomplete assessment of catalytic reaction centers. For γ-$Al_2O_3$ specifically, the coordination of the surface aluminum atoms is of interest. DFT calculations (PW91 exchange-correlation functional) performed by Digne et al.[41,42] elucidated that four- ($Al_{IV}$) and five-coordinated ($Al_V$) aluminum centers formed from cations that occupied exposed octahedral positions and three-coordinated ($Al_{III}$) centers from atoms in tetrahedral positions are stable on the (100) and (110) surfaces of γ-$Al_2O_3$ (Figure 2a). An atom's ability to accept electrons, a measure of Lewis acidity, can be described by the energy of the lowest unoccupied state of the atom; Digne et al.[42] calculated that this energy increased (became more positive) as the coordination of the surface aluminum center increased (Table 1), displaying an inverse relationship between Lewis acidity and surface aluminum atom coordination. Furthermore, they determined that two- and three-coordinated surface oxygen atoms form basic sites, demonstrating that surface Al-O moieties can act as Lewis acid-base pairs to perform catalysis. The calculated distribution of acidity among surface sites has also been determined experimentally on pyridine-exposed γ-$Al_2O_3$ samples in which multiple IR absorption bands (1453 and 1459 $cm^{-1}$)[43] and $^{15}N$ NMR peaks (at 110 and 134 ppm)[44], attributed to pyridine adsorbed onto Lewis acid sites of differing strengths, were detected. The existence

**Table 1.** Energy levels of the lowest unoccupied state relative to vacuum level for multiple under-coordinated aluminum atoms on the surface. Adapted from[42].

| Surface Site | (110) $Al_{III}$ | (100) $Al_V$ | (110) $Al_{IV}$ | (110) $Al_{IV}$ | (100) $Al_V$ | (100) $Al_V$ |
|---|---|---|---|---|---|---|
| E (eV) | -2.5 | -1.6 | -1.5 | -1.1 | -0.7 | +0.1 |

of this diverse array of surface structures at ambient temperature and pressure does not implicate their existence and/or involvement in chemical catalysis. For this reason, we employ chemical titrations performed under reaction conditions to determine the density of the pools of identified catalytic sites.

The surface energies of the prominent facets of plate-like $\gamma$-$Al_2O_3$ were assigned by Kovarik et al.[25] to decrease in the proceeding order: (110), (111), and (100) based on thermally-induced surface transformations observed using transmission electron microscopy images and electron diffraction patterns. This observation is consistent with the postulate that the higher energy facets, (111) and (110), possess a larger portion of under-coordinated aluminum atoms (Table 1) and, consequently, a more acidic pool of catalytic sites compared to the (100) surface. Activation energies of ethylene synthesis on the (100), (110), and (111) facets calculated by Christiansen et al.[45] were 37, 30, and 28 kcal $mol^{-1}$, respectively, elucidating that unimolecular ethanol dehydration preferentially occurs the (110) and (111) surface facets. The calculated activation energies of DEE synthesis, however, was comparatively invariant with the modeled surface facet (35, 34, and 32 kcal $mol^{-1}$ on the (100), (110), and (111) facets, respectively), demonstrating that DEE synthesis is less sensitive to the surface energy of the facet compared to ethylene synthesis[45]. These approaches to determine the active aluminum facets, however, do not take into account which active sites are open to catalysis under reaction conditions in presence of water. We perform measurements using basic probe molecules during reaction, in presence of both ethanol and water, to show

that all unimolecular ethanol conversion reactions occur on a separate pool of catalytic sites of $\gamma$-$Al_2O_3$ than the pool active for bimolecular dehydration reactions.

### *1.2.2 Hydroxyl groups on the $\gamma$-$Al_2O_3$ surface*

Another degree of surface complexity arises when considering the possible existence of stable surface species, such as hydroxyl groups. Hydroxyl groups are observed to be both prominent and persistent on $\gamma$-$Al_2O_3$[3,4,23,41,43,46-48]. Specifically, Hendricksen et al.[49] measured the hydroxyl group density of thermally-treated water-doused $\gamma$-$Al_2O_3$ samples using deuterium exchange and observed that the density decreased from 16.7 to 1.83 OH $nm^{-2}$ as the initial thermal treatment temperature was increased from 373 to 673 K. These results indicate that hydroxyl groups are removed from the surface of $\gamma$-$Al_2O_3$ upon heating. Hendricksen et al.[49] further employed microcalorimetric techniques on these samples and measured that the adsorption enthalpy of water on $\gamma$-$Al_2O_3$ at 298 K increased from -192 to -66.1 kJ $mol^{-1}$ with increasing surface coverage, and, thus, decreasing treatment temperature. These measurements are consistent with a hypothesis in which water preferentially adsorbs and disassociates on the stronger (highly under-coordinated) surface aluminum centers (Figure 2b). DFT calculations performed by Digne et al.[41,42] mirrored this result, as they calculated that water preferentially disassociates on strong Lewis acidic $Al_{III}$ sites (Table 1) with an adsorption enthalpy of -240 kJ $mol^{-1}$ and additional water molecules dissociate on the next strongest Lewis acid center with increasing enthalpies from -191 to -65 kJ $mol^{-1}$.

These calculations confirm that water, a product of ethanol dehydration, will disassociate on the strongest Lewis acid sites of the surface and block these reaction centers (Figure 2b).

As hydroxyl groups are present on the $\gamma$-$Al_2O_3$ surface under catalytic applications, an evaluation of whether these surface species act as Brønsted acid sites during ethanol conversion is apposite. The presence of Brønsted acid sites is commonly evaluated using basic probe molecules, often pyridine, in conjunction with spectroscopy or magnetic resonance measurements[43]. The IR absorption band[23] and $^{15}N$ NMR peak[44] attributed to adsorbed pyridinium ions (at 1540 $cm^{-1}$ [3,43] and 174 ppm[44], respectively) are absent on water- and pyridine-exposed $\gamma$-$Al_2O_3$ samples, verifying that hydroxyl groups on $\gamma$-$Al_2O_3$ are not acidic enough to protonate pyridine. Therefore, we conclude that ethanol conversion is instead entirely catalyzed by Lewis acid centers and that hydroxyl groups serve only to block highly under-coordinated aluminum atoms during reaction. We confirm this hypothesis by observing that the rates of both of the parallel ethanol dehydration reactions on $\gamma$-$Al_2O_3$ samples that have been exposed to water for 1 h are lower than the rates on $\gamma$-$Al_2O_3$ samples that did not undergo this catalyst pretreatment. Moreover, ethylene synthesis rates were reduced by water exposure to a larger extent than DEE synthesis rates, revealing that hydroxyl groups preferentially cover catalytic sites active for unimolecular dehydration.

# *Chapter 2: Kinetics and Mechanism of Ethanol Dehydration on γ-$Al_2O_3$: The Critical Role of Dimer Inhibition*

## 2.1 Introduction

Gamma alumina (γ-$Al_2O_3$) is an industrially relevant solid catalyst because of its high surface area (50-300 $m^2 g^{-1}$) and thermal stability up to 873 K[1,2,36,50,51]. Alcohols dehydrate over γ-$Al_2O_3$ to form either olefins or ethers through unimolecular or bimolecular pathways, respectively; both pathways result in the production of water as a byproduct[5,52]. The dehydration of alcohols over γ-$Al_2O_3$, thus, can serve as a probe to elucidate the catalytic site requirements and molecular reaction mechanisms on this important material.

The surface of γ-$Al_2O_3$ contains hydroxyl groups, Lewis acid sites in the form of surface aluminum (Al) atoms, as well as surface oxygen (O) atoms capable of behaving as basic sites[3,53,54]. Pyridine is often used a basic probe molecule to titrate both Brønsted and Lewis acid sites on catalytic surfaces[43,55,56]. The infrared spectroscopic band associated with the presence of pyridinium ions on the surface of pyridine-exposed γ-$Al_2O_3$ samples (1540 $cm^{-1}$) was not observed by Parry[43] at ambient temperatures while a band associated with pyridine bonded to Lewis acid sites (1450 $cm^{-1}$) was observed, leading the authors to conclude that surface hydroxyl groups are unable to protonate pyridine and, by extension, the less basic alcohol molecules; thereby demonstrating that acid sites required for alcohol dehydration over γ-$Al_2O_3$ are likely to be Lewis acidic

rather than Brønsted acidic. Furthermore, upon evacuation of the sample at 423 K, Parry[11] observed the band at 1450 $cm^{-1}$ split into two distinct bands verifying the existence of multiple Lewis acid sites on $\gamma$-$Al_2O_3$. The conclusion that $\gamma$-$Al_2O_3$ is not Brønsted acidic is further supported by $^{15}N$ Nuclear Magnetic Resonance (NMR) measurements on pyridine exposed $\gamma$-$Al_2O_3$ performed by Ripmeester[44] in which the pyridinium ion (peak at 170 ppm) was also not observed. Additionally, Kwak et al.[57] observed a near 1:1 correlation with the decrease in the intensity the $^{27}Al$ NMR peak attributed to surface penta-coordinated aluminum atoms (~23 ppm) and the BaO loading of BaO loaded $\gamma$-$Al_2O_3$ samples, indicating that BaO acts as a selective titrant of penta-coordinated alumina atoms. Furthermore, Kwak et al.[58] observed the dehydration rates of methanol into dimethyl ether on BaO/$\gamma$-$Al_2O_3$ at 573 K decreased with BaO loading, suggesting that Lewis acidic penta-coordinated surface alumina atoms play an important role in the synthesis of ethers from alcohol dehydration on $\gamma$-$Al_2O_3$.

Pines and Haag[59] found that the cis/trans ratio among 2-butene isomers produced from 2-butanol dehydration (cis/trans = 4.3) was nearly equivalent to that from 1-butene double-bond isomerization (cis/trans = 4.4) over η-alumina at 523 K; on this basis the authors concluded that the two reactions occur through the same intermediate. The authors proposed a proton olefin complex on the surface formed from the decomposition of a surface bound oxonium ion as the intermediate for olefin formation to explain the high cis/trans ratios observed. Knözinger and Scheglila[60] alternatively concluded olefin formation occurs through an E-2 type elimination of the alcohol rather than through a

proton-olefin complex intermediate based upon the measured kinetic isotope effects (KIE) for the dehydration of deuterated *tert*-butanol, *sec*-butanol, and *iso*-butanol into butenes between 393 K and 483 K. Knözinger et al.[13] proposed the alcohol undergoes this elimination across a surface hydroxyl group and a basic center. An olefin in absence of water, however, would be unable to reform the proposed reaction intermediate; the active sites, therefore, would not be appropriate for olefin double bond isomerization. Thus, the mechanism proposed by Knözinger et al.[13] is unable to fully explain the same cis/trans ratios for dehydration and double bond- isomerization measured by Pines and Haag[59].

Steady state kinetic measurements performed by Knözinger et al. on the rate of olefin formation from the dehydration of cyclohexanol[5] (10 - 33 kPa at 433 K and 453 K) and the rate of ether formation from the dehydration of methanol[26] (7 – 35 kPa methanol pressures at 433 - 468 K) over $\gamma$-$Al_2O_3$ with varying alcohol and water partial pressures showed that the rates of olefin and ether synthesis were inhibited by water and increased with alcohol pressure before becoming independent of alcohol pressure. The empirical rate expression shown in Equation 1 was proposed by the authors to fit the resulting data for both reactions.

$$r = r_0 \frac{\sqrt{P_A}}{\sqrt{P_A} + bP_W} \qquad (1)$$

*r* is the rate of olefin or ether formation, $r_0$ is the rate of olefin or ether formation at the zero order in alcohol pressure limit, $P_A$ and $P_W$ are the partial pressures of alcohol and water, respectively, and b is an empirical constant. The square root dependence in ethanol pressure of proposed expression, however, implies the dissociation of the alcohol

molecule into two equivalent surface species, which is not consistent with their proposed mechanisms for dehydration. Conversely, Shi and Davis[18] observed, upon dehydration of 2-butanol and methanol at a constant total alcohol pressure at 503 K, the selectivity of di-2-butyl and dimethyl ether increased proportionally with the square of the partial pressure of 2-butanol and methanol, respectively. Alternatively, De Morgues et al.[11] proposed that olefin formation occurred over two sites, one of which is inhibited by water surface species based upon their observation that the rate of propene synthesis from 2-propanol dehydration was inversely proportional to water pressure (in the range of 0.0 kPa to 1.2 kPa) and independent of 2-propanol pressure (in the range of 1.1 kPa to 3.1 kPa) between 373 and 433 K. A mechanism consistent with the observed inhibitory kinetic effects of water and the pressure dependence of both ether and olefin synthesis rates on alcohol pressure has not been reported in the literature.

In this work, steady state kinetic measurements demonstrate ethylene and diethyl ether (DEE) synthesis from the dehydration of ethanol over $\gamma$-$Al_2O_3$ at 488 K are both inhibited by the formation of ethanol-water dimer species at ethanol pressures between 1.9 kPa and 7.0 kPa and water partial pressures between 0.4 kPa and 2.2 kPa. Water was determined to irreversibly poison a fraction of the active sites for ethylene and DEE formation. Pyridine was found to reversibly inhibit the rate of both ethylene and DEE synthesis to different degrees; indicating the active sites are acidic in nature and are not identical for the two dehydration products. Kinetic mechanisms consistent with these conclusions are presented and evaluated.

## 2.2 Materials and methods

### *2.2.1 Catalyst preparation*

$\gamma$-$Al_2O_3$ (Alfa Aesar, BET surface area = 155 $m^2/g^{-1}$, pore volume = 0.257 $cm^3g^{-1}$) was treated for 3 h in a 1M $NH_4NO_3$ solution at 353 K prior to its use in kinetic experiments as previously described by Roy et al.[23]. Catalyst particle sizes between 180 and 425 μm (40–80 mesh) were obtained by pressing and sieving the $\gamma$-$Al_2O_3$ powder. Acid-washed quartz sand (0.5-0.7 g, 152–422 μm particle size, Acros Organics) was mixed with the catalyst samples (0.02-0.2 g) to form the reactor bed. The catalyst was then treated in dry air (1.67 $cm^3$ $s^{-1}$ at NTP conditions, Ind. Grade, Matheson Tri-gas) for 4 h at 723 K after heating the catalyst from ambient conditions with a rate of 0.017 K $s^{-1}$. The catalyst samples were then cooled in dry air (1.67 $cm^3$ $s^{-1}$) to the reaction temperature (488 K). The regeneration of the catalyst after kinetic experiments was also achieved using the same treatment in air.

### *2.2.2 Steady state kinetic measurements of ethanol dehydration over $\gamma$-$Al_2O_3$*

The rate of ethanol dehydration was measured using a quartz tube packed bed reactor (10 mm inner diameter, 1.6 $cm^3$ bed volume) system. The bed temperature was measured with a type K thermocouple located on the external surface of the reactor and maintained at reaction temperature (488 K) using a tube furnace (National Electric

Furnace FA120 type) and a Watlow temperature controller (96 series).

Ethanol dehydration was carried out at 488 K and ambient pressure under a carrier gas consisting of He (1.7-3.2 $cm^3\ s^{-1}$ at NTP conditions, Grade 4.7, Minneapolis Oxygen Company) and an internal standard mixture for analysis (25.0% $CH_4$ and balance Ar, 0.017 $cm^3\ s^{-1}$ at NTP conditions, Minneapolis oxygen) and under differential reaction conditions (<10% conversion). The catalyst was exposed to 2.2 kPa of deionized water diluted with the carrier gas (1.7 $cm^3\ s^{-1}$) for 1 h at 488 K prior to reaction.

Liquid pyridine (99+%, Sigma Aldrich), $C_2H_5OH$ (99.5%, Decon Laboratories, Inc.), $C_2H_5OD$ (99.5 at.% D, Sigma–Aldrich), $C_2D_5OD$ (99.5 at.% D, Sigma-Aldrich), and deionized water were fed into the carrier gas stream at 405 K via syringe pumps (KD scientific KDS -100 and Cole Parmer). Feed partial pressures (0.0-0.3 kPa pyridine, 0.9-7.0 kPa $C_2H_5OH$, 1.3 kPa $C_2H_5OD$, 1.0 kPa $C_2D_5OD$, and 0.4-2.3 kPa deionized water) were controlled by adjusting the liquid flowrates into the system. Condensation of the reactants and products was avoided via the resistive heating of the transfer lines to temperatures greater than 343 K.

The composition of the reactor effluent was analyzed using an online mass spectrometer (MKS Cirrus 200 Quadrupole) and a gas chromatograph (Agilent 6890 N GC) with both a flame ionization detector fed through a methyl-siloxane capillary column (HP-1, 50.0 m x 320 μm x 0.52 μm) and a thermal conductivity detector fed through a packed column (SUPELCO HAYESEP R 80/100 mesh packed column, 12 ft). Error bars in reported figures correspond to the 95% confidence intervals based upon successive gas

chromatograph injections taken without changing the experimental conditions.

A reactor containing only quartz sand diluent (0.793 g) generates, on average, 1.1 x $10^{-9}$ mol $s^{-1}$ of DEE and no ethylene upon feeding ethanol (2.6 kPa) and water (1.1 kPa) at 488 K. The production of DEE on the quartz sand diluent (~10 % of the total rate of DEE production) was accounted for and removed when calculating the reported rates of DEE synthesis. Exposure to pyridine (0.1 kPa) was observed to completely and irreversibly deactivate the production of DEE on the diluent alone; the rate of DEE production was, therefore, not adjusted in measurements in which pyridine was co-fed with ethanol (Section 2.3.2).

*2.2.3 In-Situ chemical titration of diethyl ether active sites using pyridine*

Pyridine (0.02 and 0.05 kPa) was introduced to a reactant stream containing ethanol (1.5 kPa) and water (1.1 kPa) flowing over 0.2 g of catalyst (exposed to 2.2 kPa of water at 488 K for 1 h) at 488 K and the resulting transient production of DEE was monitored using an in-line mass spectrometer (MKS Cirrus 200 Quadrupole mass spectrometer system). The pyridine uptake that would eliminate DEE synthesis was determined by extrapolating the deactivation profile (see Section 2.3.2).

*2.2.4 Parameter estimation techniques for kinetic modeling*

Kinetic parameters were optimized and uncertainties (95% marginal highest posterior density intervals) were determined using the Athena Visual Studio (v14.2, W.

E. Stewart and M. Caracotsios) statistical software package and Bayesian statistical estimation techniques. Replicates for fit analysis were provided by independent kinetic measurements at the same ethanol and water pressure but for experimental measurements taken at constant water or constant ethanol pressure discussed in Section 2.3.4.

## 2.3 Results and discussion

### *2.3.1 Effects of prior exposure of γ-$Al_2O_3$ to water on ethanol dehydration rates*

The rates of ethylene and diethyl ether synthesis from the dehydration of ethanol at 488 K were found to be 59 and 34% lower, respectively, for catalyst samples that have undergone treatment in water prior to reaction (exposed to 2.2 kPa of water at 488 K for 1 h) than catalyst samples which have not (Table 2), demonstrating water is capable of deactivating some of the active sites and inhibiting the rate of ethylene and DEE

**Table 2.** Ethylene and DEE synthesis rates for ethanol dehydration at an ethanol pressure of 1.2 kPa and a total gas flowrate of 3.2 $cm^3$ $s^{-1}$ over 0.02 g of γ-$Al_2O_3$ at 488 K for a catalyst sample which was not exposed to water prior to reaction, a catalyst sample exposed to 2.2 kPa water for 1 h prior to reaction, and the water exposed sample regenerated in air (1.67 $cm^3$ $s^{-1}$ for 4 h at 723 K).

| Catalyst Sample | Ethylene Synthesis Rate ($/10^{-7}$ mol $s^{-1}$ $g^{-1}$) | DEE Synthesis Rate ($/10^{-6}$ mol $s^{-1}$ $g^{-1}$) |
|---|---|---|
| **No $H_2O$ Exposure** | 2.22 | 5.29 |
| **$H_2O$ Exposed** | 0.90 | 3.49 |
| **Regenerated** | 2.42 | 5.49 |

formation either by irreversibly adsorbing onto the active sites or by causing a structural change in the surface of the catalyst. This conclusion is supported by the Temperature Programmed Desorption (TPD) experiments performed by Roy et al.[23] in which the amount of 2-propanol adsorbed onto the surface of their $\gamma$-$Al_2O_3$ samples was found to be 73% lower for samples with prior exposure to water (exposed to 0.4 kPa water vapor at 373 K) than for samples without any prior water exposure. Additionally, Roy et al.[23] observed the temperature at which olefin was formed was unchanged between the samples; leading the authors to conclude water simply blocked adsorption sites on the $\gamma$-$Al_2O_3$ surface rather than altering structure of the active sites. Density Functional Theory (DFT) calculations (Perdew–Wang 91 generalized gradient-corrected exchange–correlation functional) by Digne et al.[41,42] and by Wischert et al.[4] both demonstrate water is capable of irreversibly disassociating on the under-coordinated aluminum atoms on the catalyst surface to form stable surface hydroxyl species, preferentially on highly under-coordinated (three- or four-coordinated) aluminum atoms[41,42]. Furthermore, Wischert et al.[4] observed that the number of sites for methane and hydrogen adsorption on $\gamma$-$Al_2O_3$ decreased with hydroxyl group coverage for samples pretreated at temperatures less than 923 K, demonstrating that these hydroxyl groups are capable of blocking potential catalytic active sites.

The rates of ethylene and DEE synthesis are restored upon treatment of the water exposed catalyst in air (1.67 $cm^3$ $s^{-1}$) for 4 h at 723 K (Table 2), demonstrating that thermal treatment can recover active sites for ethanol dehydration.

All subsequent experiments and measurements were performed on catalyst samples that have undergone water treatment to investigate the kinetics of ethanol dehydration in absence of the irreversible deactivation caused by the water product.

### *2.3.2 Titration of active sites for ethanol dehydration*

The rates of ethylene and DEE synthesis were observed to be inhibited by pyridine, but were found to return to the values measured prior to the introduction of pyridine after the pyridine feed was stopped (Figure 3a). These observations demonstrate: (1) either Lewis acidic Al atoms or hydroxyl groups comprise the active sites for both ethylene and DEE formation and (2) pyridine can reversibly bind to these active sites during ethanol dehydration; thus, inhibiting the reaction, but is incapable of irreversibly adsorbing onto these sites under reaction conditions.

The rate of formation of both ethylene and DEE normalized to the formation rate measured in the absence of a pyridine co-feed at different pyridine pressures is shown in Figure 3b. The rate of ethylene formation was found to be inhibited to a greater extent than the rate of DEE formation; indicating a difference in the equilibrium surface coverage of pyridine on the active sites of DEE and ethylene synthesis. The acidic active sites for ethylene and DEE synthesis are, therefore, not equivalent, although their uniqueness cannot be proven with inhibition experiments alone.

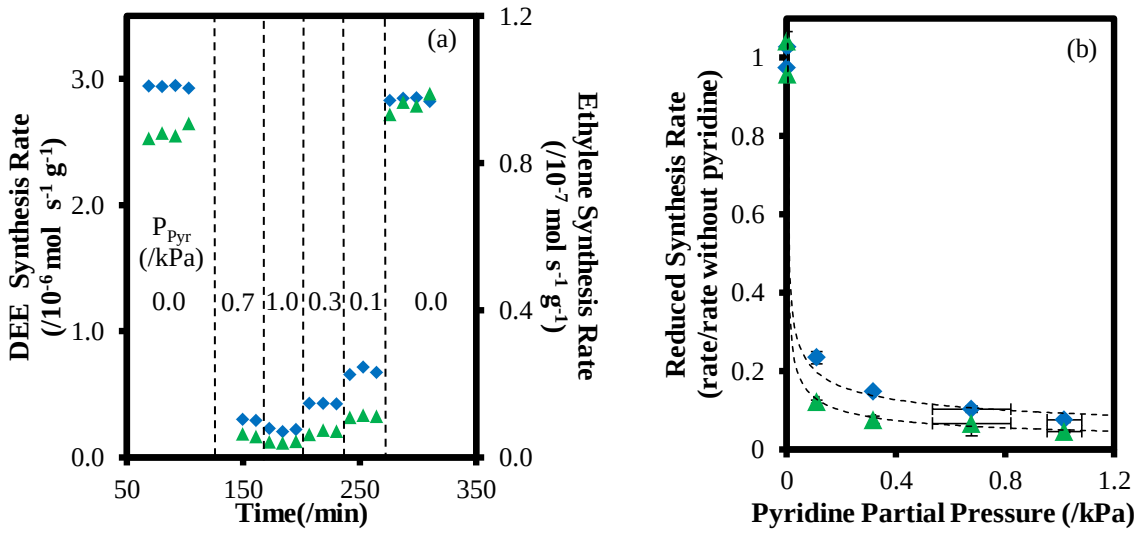


**Figure 3.** Ethylene (▲) and DEE (◆) (a) synthesis rates with respect to reaction time and (b) reduced synthesis rates normalized to the measured synthesis rates with no pyridine co-feed as a function of pyridine pressure for the dehydration of 0.9 kPa of ethanol over 0.02 g of $\gamma$-$Al_2O_3$ (total volumetric flowrate = 3.2 $cm^3$ $s^{-1}$) at 488 K. The dashed lines serve as a guide for the eye.

The amount of pyridine it would take to completely deactivate DEE synthesis was estimated by linearly extrapolating the initial slope of the measured DEE synthesis rate, considering pyridine adsorption to be irreversible and all DEE active sites to exhibit similar activity in the linear regime (Figure 4). The residual synthesis of DEE is most likely a result of the dynamic reversibility of pyridine adsorption and inhibition demonstrated in Figure 3. On average, 2.7 x $10^{-5}$ mol $g^{-1}$ (~0.10 sites $nm^{-2}$) of pyridine is estimated to completely deactivate DEE synthesis; this value is consistent across different pyridine pressures (0.02 and 0.05 kPa) and space velocities (1.1 and 2.0 $s^{-1}$) (Table 3). The number of pyridine adsorption sites for complete deactivation may not correlate directly with the number of active sites for DEE formation for two reasons: (1) it is possible that pyridine could adsorb onto sites other than the active sites for ethanol

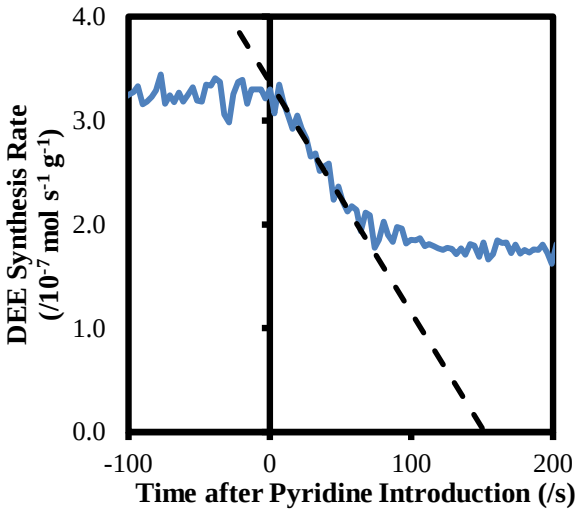


**Figure 4.** DEE synthesis rates as a function of time after introduction of 0.03 kPa of pyridine for the dehydration of ethanol (1.5 kPa and 1.1 kPa ethanol and water partial pressures, respectively) over 0.2 g of $\gamma$-$Al_2O_3$ (total volumetric flowrate = 1.7 $cm^3$ $s^{-1}$) at 488 K. The dashed line shows the linear extrapolation used to determine pyridine uptake for complete deactivation.

**Table 3.** Pyridine uptake necessary for complete deactivation of DEE synthesis rate determined from in-situ titrations performed at differing pyridine pressures and space velocities over 0.2 g of $\gamma$-$Al_2O_3$ at 488 K. The 95% confidence intervals were determined based upon independent titrations.

| Space Velocity (/$s^{-1}$) | Pyridine Pressure (/kPa) | Pyridine Uptake (/$10^{-5}$ mol $g^{-1}$) |
|---|---|---|
| 1.1 | 0.05 | 2.7 ± 0.5 |
| 1.1 | 0.02 | 2.2 ± 0.9 |
| 2.0 | 0.05 | 3.2 ± 1.6 |
| 2.0 | 0.02 | 2.7 ± 0.3 |

dehydration; and (2) the quantity of sites for either ethylene or DEE formation cannot be independently inhibited using an unspecific titrant such as pyridine.

Electron Paramagnetic Resonance measurements performed by Zotov et al.[61] on anthracene-exposed $\gamma$-$Al_2O_3$ samples determined ~0.002 molecules $nm^{-2}$ of anthracene

underwent radicalization on weak electron acceptor sites, which have been demonstrated to possess a linear correlation with the rate of ethylene formation from ethanol dehydration on doped $\gamma$-$Al_2O_3$ samples. The site density estimated by Zotov et al.[61] (~0.002 sites $nm^{-2}$) provides a lower bound to the active site density, as additional active sites for dehydration may exist that are not active for anthracene radicalization, while the estimation based upon in-situ pyridine titration (~0.1 sites $nm^{-2}$) provides an upper bound to the active site density.

*2.3.3 Kinetic isotope effects for ethanol dehydration*

The rates of ethylene and DEE formation from $C_2H_5OH$ relative to the rates of formation using $C_2D_5OD$ and $C_2H_5OD$ ($r_H/r_D$) reactants at 488 K are presented in Table 4. No statistically significant effect on the rate of DEE formation is observed when using either deuterated reactant, demonstrating the rate-limiting step of DEE formation does not involve the cleavage of a C-H bond or the cleavage of one of the O-H bonds. Bimolecular dehydration of ethanol to form DEE, therefore, involves either the cleavage of the $C_\alpha$-O bond or an Al-O bond in the rate-limiting step. Similarly, no kinetic isotope effects were observed by Knözinger et al.[62] for dimethyl ether formation from the dehydration of methanol, $CH_3OD$, and $CD_3OD$ over $\gamma$-$Al_2O_3$.

**Table 4.** Measured kinetic isotope effects for ethylene and diethyl ether formation at 488 K for the dehydration of $C_2H_5OD$ and $C_2D_5OD$ over $\gamma$-$Al_2O_3$.

| Product \ Reactant | $C_2H_5OD$[†] | $C_2D_5OD$[‡] |
|---|---|---|
| **Ethylene KIE ($r_H/r_D$)** | 0.89 ± 0.14 | 2.42 ± 0.19 |
| **Diethyl Ether KIE ($r_H/r_D$)** | 0.97 ± 0.12 | 1.01 ± 0.14 |

[†]Reactions performed under 1.3 kPa of $C_2H_5OH$ or $C_2H_5OD$ with no water co-feed.
[‡]Reactions performed under 1.0 kPa of $C_2H_5OH$ or $C_2D_5OD$ with 1.2 kPa water co-feed.

No statistically significant difference was observed between the rates of ethylene formation from the dehydration of $C_2H_5OH$ and $C_2H_5OD$, demonstrating O-H bond cleavage is not kinetically limiting for ethylene formation. A primary isotope effect, however, was observed for the dehydration of $C_2D_5OD$, verifying the rate-limiting step of ethylene formation involves either the breaking of a C-H bond (likely the more acidic $C_\beta$-H bond) or the desorption of a water molecule from the surface of the alumina in which a surface O-H bond is broken with the hydrogen atom originating from the ethanol molecule. Knözinger and Scheglila[60] similarly observed a primary kinetic isotope effect for *tert*-butanol, *sec*-butanol, and *iso*-butanol dehydration over $\gamma$-$Al_2O_3$ only when the $C_\beta$ atom was deuterated.

*2.3.4 Kinetics and mechanism of ethanol dehydration*

The formation rates of both ethylene and DEE formation were observed to be inhibited by water at 488 K; the rates of both DEE and ethylene synthesis, however, recovered to their initial value upon restoring the initial water pressure as shown in Figure 5, demonstrating water is capable of reversibly inhibiting ethylene and DEE

synthesis in addition to irreversibly deactivating a fraction of the active sites of $\gamma$-$Al_2O_3$.

The rate of ethylene synthesis upon co-feeding ethanol and water at 488 K was found to be zero order with respect to ethanol pressure for the majority of the ethanol and water pressures investigated (between 1.9 kPa and 7.0 kPa ethanol partial pressure and 0.4 kPa and 2.2 kPa water partial pressure); becoming positive order (0.4) in ethanol only at low ethanol pressures ($\leq$2 kPa) and at the tested highest water pressure (2.2 kPa) as shown in Figure 6a. A negative order dependence on water pressure for the rate of ethylene formation is still observed, however, in the regime where ethylene synthesis is invariant with ethanol pressure. These observations are consistent with the conclusion that the formation of ethylene must be inhibited at least partially by the formation of ethanol-water dimers in order to maintain the observed dependencies.

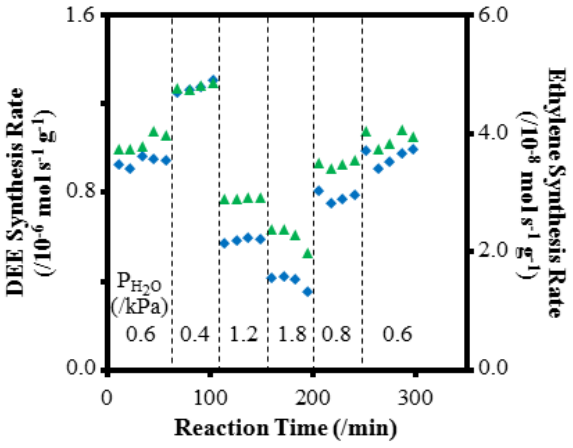


**Figure 5.** Ethylene (▲) and DEE (◆) synthesis rates from the dehydration of 4.2 kPa of ethanol over 0.02 g of $\gamma$-$Al_2O_3$ (volumetric flowrate = 3.2 $cm^3$ $s^{-1}$) at 488 K as a function of reaction time and water pressure.

The inhibition of the rate of ethylene synthesis by water (0.4 kPa to 1.9 kPa) was found to decrease with increasing ethanol pressure (0.9 kPa to 4.2 kPa) and was found to have, on average, an order less than one (between -0.9 and -0.5) (Figure 7). A competitive occupation of the

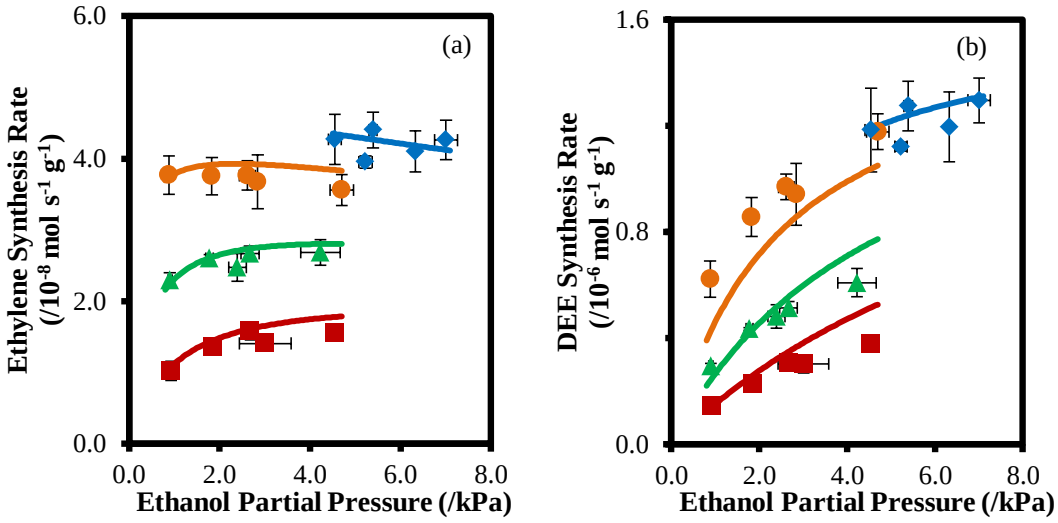


**Figure 6.** (a) Ethylene and (b) DEE synthesis rates for ethanol dehydration at 488 K on γ-$Al_2O_3$ as a function of ethanol partial pressure with 0.4 kPa (◆), 0.6 kPa (●), 1.2 kPa (▲), and 2.2 kPa (■) water co-feeds (total gas flowrate = 3.2 $cm^3$ $s^{-1}$). The solid lines represent the model fits to Equations (a) 3 and (b) 5.

surface sites by single molecule ethanol species, ethanol-water dimers, and water dimer surface species provides a consistent kinetic scheme capable of describing these observations.

A positive order dependence (between 0.0 and 0.8) in ethanol partial pressure was observed for the rate of DEE formation over the tested range of ethanol and water partial pressures (Figure 6b); with the exception of the highest tested ethanol pressures (>4 kPa) and the lowest tested water partial pressure (0.4 kPa), where the rate of DEE formation was found to be independent of ethanol pressure. The observed reaction order for DEE synthesis with respect to ethanol decreased with increasing ethanol pressure and decreasing water pressure. These observations can be explained by the competition between ethanol-water dimers and adsorbed ethanol dimers. This conclusion is further supported by the observation that the reaction order with respect to water pressure

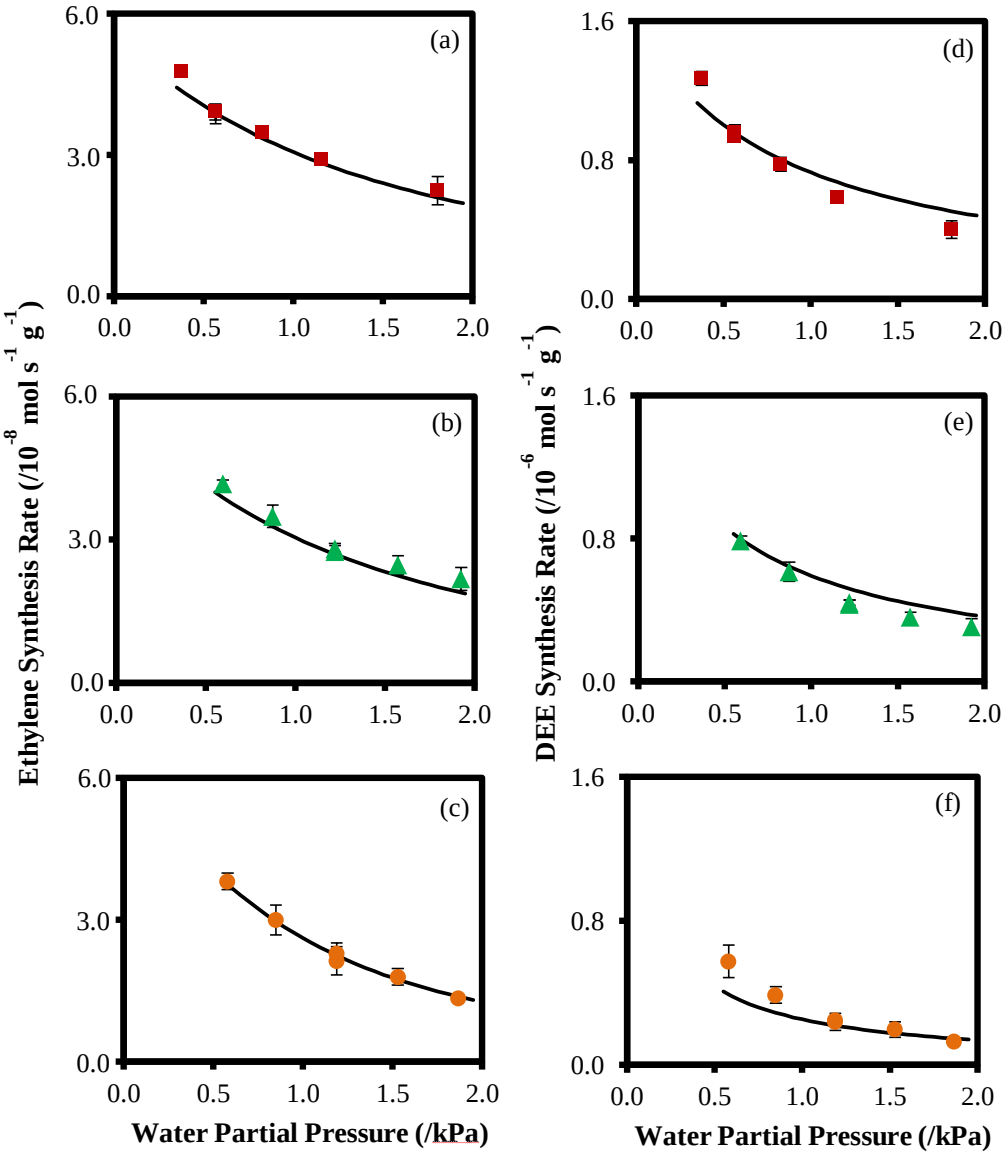


**Figure 7.** (a-c) Ethylene and (d-f) DEE synthesis rates for ethanol dehydration at 488 K over γ-$Al_2O_3$ as a function of water partial pressure with (a,d) 4.2 kPa (■), (b,e) 3.0 kPa (▲), and (c,f) 0.9 kPa (●) ethanol co-feeds (total gas flowrate = 3.2 $cm^3$ $s^{-1}$). The solid lines represent fits to the experimental data with the models presented in Equations (a-c) 3 and (d-f) 5.

decreases with increasing ethanol pressure (0.9 kPa to 4.2 kPa) from -1.3 to -0.7 (Figure 7).

The rate of ethylene and DEE synthesis was found to be in the zero order regime with respect to ethanol pressure above 4 kPa of ethanol and at 0.4 kPa of water (Figure 6b) despite ethylene synthesis being a unimolecular reaction and DEE synthesis being a bimolecular reaction; implying the active site sites for ethylene and DEE formation are inhibited by different surface species. This observation, in addition to the observed differences in pyridine inhibition of the synthesis rates for the two dehydration products, leads us to postulate that the site requirements for ethylene and DEE synthesis are distinct.

The observed site requirements and the measured kinetic dependencies for ethylene formation can be explained with the proposed ethoxide mediated mechanism shown in Figure 8. In this mechanism, an ethanol molecule initially adsorbs onto a Lewis acid site of $\gamma$-$Al_2O_3$ (Step 1, Figure 8) and dissociates on the surface to form an ethoxide species and a hydroxyl group comprised of the hydrogen atom from ethanol and a surface oxygen atom on the same Lewis acid site (Step 2, Figure 8). The $C_\beta$-H and $C_\alpha$-O bonds are subsequently cleaved as the ethoxide species desorbs from the surface to form an ethylene molecule and a hydroxyl group on the $\gamma$-$Al_2O_3$ surface in the rate-limiting step (Step 3, Figure 8). Desorption of the hydroxyl group and a surface proton forms a water molecule; regenerating the catalyst surface and completing the catalytic cycle (Step 4, Figure 8). The active site can be inhibited by the adsorption a water molecule (Step 5,

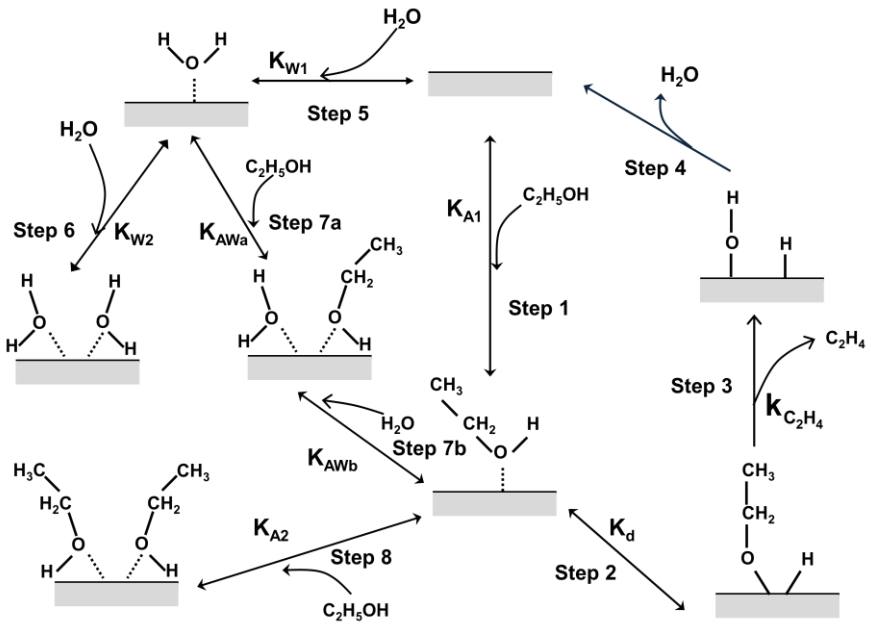


**Figure 8.** Ethoxide desorption limited mechanism for ethylene formation from ethanol dehydration over γ-$Al_2O_3$.

Figure 8) along with the subsequent adsorption of an additional water or ethanol molecule to form either a water dimer (Step 6, Figure 8) or an ethanol-water dimer (Step 7a, Figure 8), respectively. The ethanol-water dimer could alternatively be formed from the adsorption of a water molecule onto an active site occupied by a surface bound ethanol molecule (Step 7b, Figure 8). These two routes for the formation of the ethanol-water dimer, however, cannot be kinetically distinguished. The active site could also be inhibited by an ethanol dimer species formed from the adsorption of a second ethanol molecule after the formation of the surface bound ethanol species (Step 8, Figure 8).

The kinetic expression for the rate of ethylene formation ( $r_{C_2H_4}$ ) presented in Equation 2 can be derived from the mechanism presented in Figure 8 assuming quasi-equilibrium is achieved for all steps prior to the proposed rate limiting desorption of the

ethylene molecule (Step 3, Figure 8).

$$r_{C_2H_4} = \frac{k_{C_2H_4} K_{A1} K_d P_{EtOH}}{1 + K_{A1} K_d P_{EtOH} + K_{W1} P_{H_2O} + (K_{W1} K_{AWa} + K_{A1} K_{AWb}) P_{EtOH} P_{H_2O} + K_{A1} K_{A2} P_{EtOH}^2 + K_{W1} K_{W2} P_{H_2O}^2} \quad (2)$$

$P_{EtOH}$ and $P_{H_2O}$ denote the partial pressures of ethanol and water, respectively. The kinetic parameter $k_{C_2H_4}$ represents the rate constant associated with the formation of ethylene by desorption of ethoxide species. The parameters $K_{A1}$, $K_d$, $K_{A2}$, $K_{W1}$, $K_{W2}$ denote the equilibrium constants for the formation of adsorbed ethanol species, dissociation of the ethanol species to form a surface ethoxide species, formation of ethanol dimer complexes, the adsorption of water onto the active sites, and subsequent adsorption of an additional water molecules to form water dimer complexes, respectively. $K_{AWa}$ and $K_{AWb}$ are the equilibrium constants for the kinetically indistinguishable routes for the formation of the ethanol-water dimers from the adsorption of an ethanol molecule to an active site occupied by a surface bound water molecule or the adsorption of a water molecule to an active site occupied by an ethanol molecule, respectively.

If surface bound ethoxide species, ethanol-water dimer species, water dimer species, and surface bound ethanol dimer species are considered to be the dominant surface species under the conditions investigated in this kinetic study, Equation 2 can be simplified into Equation 3.

$$r_{C_2H_4} = \frac{k_{C_2H_4} P_{EtOH}}{P_{EtOH} + \frac{K'_{AW}}{K_{A1} K_d} P_{EtOH} P_{H_2O} + \frac{K_{A1} K_{A2}}{K_{A1} K_d} P_{EtOH}^2 + \frac{K_{W1} K_{W2}}{K_{A1} K_d} P_{H_2O}^2} \quad (3)$$

**Table 5.** Estimated values for the kinetic parameters of ethylene formation over $\gamma$-$Al_2O_3$ at 488 K using the model presented in Equation 3 and the data from Figures 6 and 7.

| **Parameter** | $\mathbf{k_{C_2H_4}}$ **(mol$_{C_2H_4}$ s$^{-1}$ g$^{-1}$)** | $\frac{\mathbf{K'_{AW}}}{\mathbf{K_{A1}K_d}}$ **(kPa$^{-1}$)** | $\frac{\mathbf{K_{A1}K_{A2}}}{\mathbf{K_{A1}K_d}}$ **(kPa$^{-1}$)** | $\frac{\mathbf{K_{W1}K_{W2}}}{\mathbf{K_{A1}K_d}}$ **(kPa$^{-1}$)** |
|---|---|---|---|---|
| **Estimated Value** | $(6.42 \pm 0.90)\text{x}10^{-8}$ | $0.81 \pm 0.27$ | $0.035 \pm 0.028$ | $0.57 \pm 0.19$ |

The new parameter $K'_{AW}$ represents the sum of the equilibrium constants for the two indistinguishable mechanisms for the formation of the ethanol-water dimer species ($K'_{AW} = K_{W1}K_{AWa} + K_{A1}K_{AWb}$). Equation 3 is consistent with the observation that the rate of ethylene synthesis is largely independent of ethanol pressure (between 1.9 kPa and 7.0 kPa ethanol partial pressure and 0.4 kPa and 2.2 kPa water partial pressure), becoming slightly positive order only at low ethanol pressures (less than 1.9 kPa ethanol) at the highest water pressure tested (2.2 kPa), while being inhibited by water with an average order less than one. The parameters in Equation 3 were fit to the experimental data and their values are shown in Table 5. The parity plot of the fitted model, shown in Figure 9a, demonstrates the proposed model is capable of describing the data accurately. The normal probability plot and lag plot for the residual error in the model are presented and discussed in Section 6.1.

The value of $\frac{K_{W1}K_{W2}}{K_{A1}K_d}$ (0.57 kPa$^{-1}$) relative to the value of $\frac{K'_{AW}}{K_{A1}K_d}$ (0.81 kPa$^{-1}$)

signifies that water dimers will become more abundant on the surface of $\gamma$-$Al_2O_3$ than the ethanol-water dimers when the ratio of water to ethanol pressure exceeds 1.5; which explains why a positive order dependence of ethanol on the rate of ethylene formation

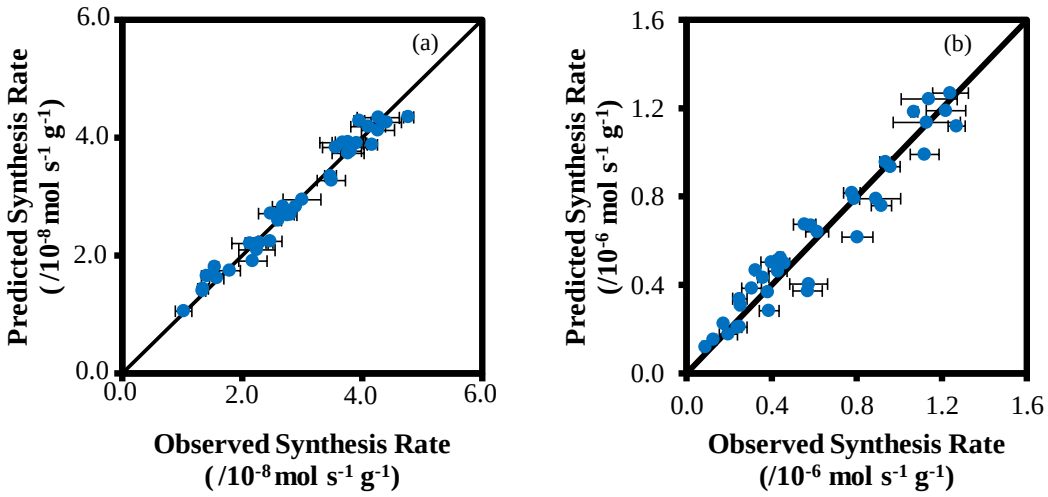


**Figure 9.** Parity plots for the kinetic models presented in (a) Equation 3 for ethylene formation and (b) Equation 5 for diethyl ether formation at 488 K. The solid line represents a perfect prediction of the observed synthesis rates.

was observed only when the water pressure was equivalent to or exceeded the ethanol partial pressure (Figure 6a).

The lower value of $\frac{K_{A1}K_{A2}}{K_{A1}K_d}$ (0.035 $kPa^{-1}$) relative to both $\frac{K_{W1}K_{W2}}{K_{A1}K_d}$ and $\frac{K'_{AW}}{K_{A1}K_d}$

signifies that only a small fraction of the surface is occupied with ethanol dimers except at the highest ethanol pressures and lowest water pressure tested. For this reason, the number of tested conditions in which this term is significant is much smaller than the other terms in the denominator of the rate expression which results in a relatively large confidence interval (80 % of the parameter value).

The proposed desorption of the ethoxide species is consistent with the E2-like rate-limiting step for olefin formation proposed by Knözinger and Scheglila[60] based upon the observed KIE. The formation of ethoxides is supported by the observation of Greenler[10] that the infrared (IR) spectra of alumina exposed to ethanol before evacuation contained

similar bands to those found in the IR spectra of $Al(OCH_2CH_3)_3$. Furthermore, Gabrienko et al.[24] observed chemical shifts indicative of the formation of alkoxide species on different Lewis acid sites in $^{13}C$ solid state NMR measurements of $\gamma$-$Al_2O_3$ exposed to $^{13}C$ labeled propene, n-butene, and isobutene (63 and 79 ppm, 69 and 74 ppm, and 67 ppm, respectively). Thus, the desorption of a surface ethoxide species (step 3) is proposed to be rate-limiting rather than the subsequent desorption of water (step 4) which could also produce the observed KIE (Section 2.3.3). The existence of surface ethoxides does not, however, guarantee their involvement in the synthesis of ethylene; thus, a kinetically equivalent mechanism in which the adsorbed ethanol monomer formed in step 2 directly undergoes an E2-elimination to form ethylene could also be proposed and cannot be distinguished with kinetic measurements alone.

A similar mechanism (Figure 10) can be proposed for the formation of DEE. Initially, an ethanol molecule adsorbs onto the active site of the catalyst (Step 1, Figure 10). The adsorption of another ethanol molecule forms an ethanol dimer complex on the surface (Step 2, Figure 10). This dimer complex then decomposes in a rate-limiting step involving the cleavage of either a C-O or Al-O bond to form a gas phase DEE molecule and a water molecule, regenerating the catalyst surface in the process (Step 3, Figure 10); although this process is expected to be comprised of many fundamental steps, these steps are not kinetically observable. Alternatively, a water molecule can competitively adsorb onto the active site (Step 4, Figure 10), and subsequent adsorption of an additional water molecule or an ethanol molecule forms a water dimer (Step 5, Figure 10) or an ethanol-

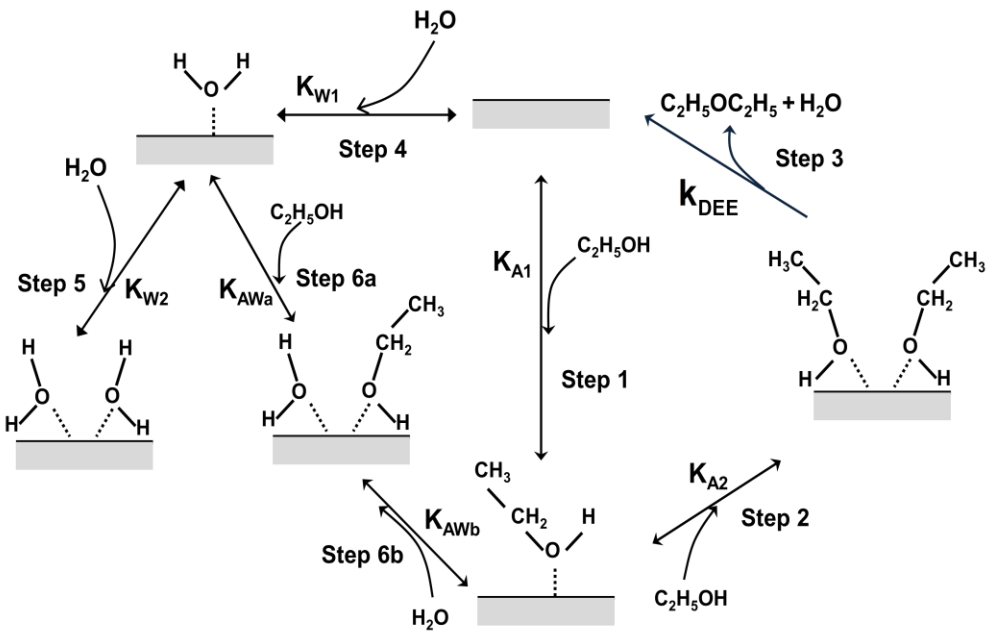


**Figure 10.** Bimolecular mechanism for diethyl ether formation from ethanol dehydration over $\gamma$-$Al_2O_3$.

water dimer species (Step 6a, Figure 10), respectively, capable of inhibiting the rate of DEE formation. As was the case with ethylene formation, the ethanol-water dimer could alternatively be formed from the adsorption of a water molecule onto a site occupied by a surface bound ethanol molecule (Step 6b, Figure 10).

Equation 4 shows the kinetic expression for the rate of DEE formation ( $r_{DEE}$ ) derived from the proposed mechanism.

$$r_{DEE} = \frac{k_{DEE} K_{A1} K_{A2} P_{EtOH}^2}{1 + K_{A1} P_{EtOH} + K_{W1} P_{H_2O} + (K_{W1} K_{AWa} + K_{A1} K_{AWb}) P_{EtOH} P_{H_2O} + K_{A1} K_{A2} P_{EtOH}^2 + K_{W1} K_{W2} P_{H_2O}^2} \quad (4)$$

The rate constant for DEE formation is denoted by $k_{DEE}$. Equation 4 can be simplified into Equation 5 assuming that ethanol-water and ethanol dimer species are more abundant than the other surface species depicted in Figure 10.

$$r_{DEE} = \frac{k_{DEE} P_{EtOH}^2}{P_{EtOH}^2 + \frac{K'_{AW}}{K_{A1} K_{A2}} P_{EtOH} P_{H_2O}} \quad (5)$$

The rate expression presented in Equation 5 can describe the observed less-than-one reaction order in ethanol pressure on the rate of DEE formation and the observation that the order decreased with increasing ethanol pressure and decreasing water pressure until becoming independent of ethanol pressure. The parameters in Equation 5 were estimated with a Bayesian fit to the experimental data collected at 488 K and are shown in Table 6. The model accurately describes the data between 0.9 and 3.0 kPa in ethanol partial pressure and between 1.2 and 2.2 kPa water partial pressures as well as describing the zero order regime at ethanol pressures >4.5 kPa and at a water pressure of 0.4 kPa (Figures 6b and 7b). The parity plot for the model and the collected data is presented in Figure 9b. The normal probability plot and lag plot associated with the residual error in the model are presented and discussed in the Section 6.1.

The value of the combined parameter $\frac{K'_{AW}}{K_{A1} K_{A2}}$ (5.05) signifies, under the experimental conditions, ethanol-water dimers are the most abundant surface species unless the ethanol pressure is four or more times greater than the water pressure, explaining

**Table 6.** Estimated values for the kinetic parameters of DEE formation over $\gamma$-$Al_2O_3$ at 488 K using the model presented in Equation 5 and the data from Figures 6 and 7.

| **Parameter** | $\mathbf{k_{DEE}}$ **($\mathbf{mol_{DEE}\ s^{-1}\ g^{-1}}$)** | $\frac{\mathbf{K'_{AW}}}{\mathbf{K_{A1}K_{A2}}}$ |
|---|---|---|
| **Estimated Value** | $(1.60 \pm 0.18)\text{x}10^{-6}$ | $5.05 \pm 1.24$ |

why the rate of DEE formation was found to be independent of ethanol partial pressure only when the ethanol partial pressure was an order of magnitude larger than the water partial pressure.

Pyridine titration studies elucidated both the acidic and non-equivalent nature of the active sites for the formation of ethylene and DEE; whether the active sites consist of a single adsorption site or two adjacent adsorption sites, however, could not be determined based upon kinetic experiments or pyridine titration studies alone. The ethanol dimers, water dimers, and ethanol-water dimers could represent either two molecules adsorbed onto the same adsorption site, as shown to form on acidic zeolites[6,40,63], or adsorbed onto two adjacent adsorption sites both of which are necessary for the formation of ethylene and DEE and comprise the active site for dehydration. These two possibilities, however, are kinetically equivalent and, thus, cannot be distinguished using the information presented in this work. The existence of two adjacent adsorption sites has been previously suggested by De Mourgues et al.[11] to explain the observed independence in isopropanol pressure and simultaneous inhibition by water for the rate of propene formation from isopropanol dehydration over $\gamma$-$Al_2O_3$. De Mourges et al.[11] proposed that one site exclusively adsorbs ethanol, while the other is exclusively inhibited by water. De Mourges's model, however, does not allow for the inhibition of olefin formation by water dimers and, thus, is unable to fully explain the observed -1.6 order inhibition of the rate of ethylene synthesis by water at the lowest ethanol pressure (0.9 kPa) and highest measured water pressures (1.5 kPa and 1.9 kPa).

The measured inhibitory effects of water and the kinetic effects of ethanol for ethylene and DEE synthesis demonstrate the kinetic importance of water, ethanol-water, and ethanol molecular pairs, either in the form of adsorbed dimers or in the form of molecules adsorbed on adjacent active sites, in the dehydration of ethanol over $\gamma$-$Al_2O_3$. The observed inhibition by ethanol-water dimers for both ethylene and DEE formation on Lewis-acidic $\gamma$-$Al_2O_3$ was not observed for the same chemistry performed over Brønsted acidic zeolite catalysts[6], highlighting the important fundamental mechanistic differences between these catalytic systems. Our findings demonstrate the kinetic importance of molecular dimers for the dehydration of ethanol over $\gamma$-$Al_2O_3$ and provide important considerations for future catalytic research with this common catalytic system.

## 2.4 Conclusions

Kinetic measurements of ethanol dehydration over $\gamma$-$Al_2O_3$ at 488 K on both samples exposed to water before reaction and untreated samples established water is capable of irreversibly deactivating some of the active sites involved in the formation of both ethylene and DEE. Steady state kinetic measurements on samples treated with water demonstrated water is capable of reversibly inhibiting the rate of both ethylene and DEE synthesis on the remaining active sites. Pyridine and ethanol co-feed kinetic experiments indicated pyridine reversibly inhibits the rate of ethylene and DEE formation to different extents, demonstrating the active sites for ethylene and DEE formation are acidic and non-equivalent. In-situ pyridine titration studies estimated $2.7 \times 10^{-5}$ mol $g^{-1}$ of pyridine

are required to adsorb onto the surface of water-treated $\gamma$-$Al_2O_3$ to completely deactivate the synthesis of DEE; this value provides an upper estimate of active site density for the formation of DEE (0.10 sites $nm^{-2}$). A primary kinetic isotope effect was observed for the rate of ethylene formation when $C_2D_5OD$ was used as the reactant but not when $C_2H_5OD$ was employed, indicating the rate-limiting step for ethylene formation from ethanol dehydration over $\gamma$-$Al_2O_3$ involves either the cleavage of a C-H bond (likely the acidic $C_\beta$-H bond) of ethanol or the subsequent desorption of water from the surface of $\gamma$-$Al_2O_3$. No significant kinetic isotope effect was observed for the rate of DEE formation for either of the deuterated reactants, elucidating the formation of DEE from ethanol dehydration over $\gamma$-$Al_2O_3$ is limited by either $C_\alpha$-O or Al-O bond cleavage. Steady state kinetic measurements of the formation of ethylene and DEE at various ethanol and water partial pressures at 488 K demonstrated: (1) the rate of ethylene formation was independent of ethanol pressure for most of the ethanol and water pressures tested while being inhibited by water, (2) the rate of DEE formation was found to be a positive, less than first order dependence in ethanol pressure except at very high ethanol pressure and low water pressures where the rate of DEE formation became independent of ethanol pressure, and (3) the order of the inhibition by water decreased with increasing ethanol pressure for both ethylene and DEE formation. The proposed mechanisms and associated rate equations, in which, at the reaction conditions, the formation of ethylene and DEE is inhibited mostly by bimolecular surface species, are consistent with the experimental observations.

**Acknowledgments**

We thank Christopher Ho for his support and effort in this work as well as The Dow Chemical Company for their financial support. H. C. was supported as part of the Catalysis Center for Energy Innovation, an Energy Frontier Research Center funded by the U.S. Department of Energy, Office of Science, Office of Basic Energy Sciences under Award no. DE-SC0001004. Reprinted with permission from DeWilde et al., *ACS Catal.* **2013**, *3* (4), pp 798–807. 

# *Chapter 3: Ethanol Dehydration and Dehydrogenation on γ-$Al_2O_3$: Mechanism of Acetaldehyde Formation*

## 3.1 Introduction

Gamma alumina (γ-$Al_2O_3$), a thermally stable (up to 873 K) and high surface area (50-300 $m^2$ $g^{-1}$) Lewis acidic material, is a catalyst for the industrial production of ethylene from the dehydration of ethanol[1,2,36,50,51,58,64]. Ethanol can dehydrate on γ-$Al_2O_3$ through two parallel pathways: a unimolecular pathway to form ethylene and water and a bimolecular pathway to form diethyl ether (DEE) and water[5-7,11-14,16-18,22,23,42,65]. Knözinger et al. measured the rate of cyclohexene formation from cyclohexanol dehydration and the rate of dimethyl ether formation from methanol dehydration on γ-$Al_2O_3$ as a function of methanol and water pressure between 433 K and 468 K[12,26]. These authors observed that rates of both unimolecular and bimolecular dehydration were inhibited by water and possessed alcohol partial pressure dependences between 0 and 0.5 (7-35 kPa alcohol pressure) and described observed alcohol dehydration rates with an empirical rate equation shown below (Equation 1 from Section 2.1).

$$r = r_0 \frac{\sqrt{P_A}}{\sqrt{P_A} + bP_W} \quad (1)$$

*r* is the synthesis rates of either olefin or ether formation and $r_0$ is the synthesis rate of the products after the surface is fully saturated with alcohol (zero order in ethanol) in mol $s^{-1}$ $g^{-1}$, while $P_W$ and $P_A$ are the partial pressures of water and alcohol in torr, respectively. *b*

represents an empirically evaluated constant used to fit the measured water pressure dependence with units of $torr^{-0.5}$. Steady state kinetics of 2-propanol dehydration measured by De Morgues et al. showed that the rate of propylene synthesis at 373-433 K was independent of the partial pressure of 2-propanol (1.1-3.1 kPa) but was inversely proportional to co-fed water partial pressures (0.0-1.2 kPa), leading the authors to conclude that olefin synthesis occurs by a two-site mechanism in which water can selectively titrate one of these sites[11]. The inhibitory role of water is further supported by the combined temperature programmed desorption and thermogravimetric analysis (TPD-TGA) measurements of 2-propanol-doused $\gamma$-$Al_2O_3$ samples by Roy et al. in which catalyst samples exposed to water at 373 K absorbed less 2-propanol and produced less propylene than those that were not[23]. Additionally, density functional theory (DFT) calculations performed by Jenness et al. show that water acts to inhibit ethanol dehydration on $\gamma$-$Al_2O_3$ by forming surface hydroxyl groups that block the C-H bond cleavage sites necessary for olefin synthesis at 500 K[66]. Shi and Davis investigated methanol and 2-butanol dehydration at a higher temperature (503 K) and found that the rates of both di-2-butyl and dimethyl ether synthesis possessed a square dependence on the alcohol pressure[18]. In previous work, we reported that synthesis rates of ethylene and DEE from ethanol dehydration on $\gamma$-$Al_2O_3$ at 488 K can be described with a proposed dimer-inhibited mechanism for alcohol dehydration in which ethanol dimers and ethanol-water co-adsorbed complexes inhibited the rate of both dehydration pathways[65]. Our study aims to extend these prior investigations to industrially relevant temperatures (>

623 K) and, in particular, to investigate the kinetic role of water and the dominant surface species at these temperatures.

Dehydration, however, is not the only pathway for alcohol conversion on $\gamma$-$Al_2O_3$, as alcohols can also dehydrogenate to form ketones and aldehydes[27-29]. Chokkaram et al. reported that octanone was synthesized with a selectivity between 0.3 and 0.5 % from the conversion of 2-octanol on $\gamma$-$Al_2O_3$ at 523 K, but did not observe significant production of octanone at lower reaction temperatures[28]. Acetaldehyde synthesis was observed by Kieffer et al. upon degassing ethanol-doused samples of $\gamma$-$Al_2O_3$ at 473 K; the authors proposed that acetaldehyde is formed from the cleavage of a $C_\alpha$-H bond of an absorbed ethoxy species[27]. DFT calculations (PW91 functional) of propane metathesis on $\gamma$-$Al_2O_3$ supported tungsten carbyne structures performed by Joubert et al. confirmed that the $\gamma$-$Al_2O_3$ support was responsible for the initial dehydrogenation of propane before continued metathesis on the organometallic complex[29], further demonstrating the capability of $\gamma$-$Al_2O_3$ to activate C-H bonds for dehydrogenation. The conversion of ethanol on 0.20 g of H-ZSM-5/$\gamma$-$Al_2O_3$ at 623 K (total volumetric flowrate = 50 $cm^3$ $s^{-1}$) was observed to drop from 75% to 25% upon addition of 15 mol% of acetaldehyde to a liquid ethanol feed stream (0.015 $cm^3$ $s^{-1}$), demonstrating that acetaldehyde can deactivate ethanol dehydration on acidic catalytic systems[30]. Additionally, Diaz et al. noted that bands between 1300 and 1800 $cm^{-1}$ associated with carbonyl bending modes in infrared (IR) spectra of acetaldehyde absorbed onto H-ZSM-5 at 313 K broadened and became indistinguishable when the gas phase acetaldehyde pressure was raised above 0.4 kPa.

The authors attributed this broadening to the formation of large conjugated surface species produced by the condensation of acetaldehyde[31]. These large surface species are proposed to act as coke precursors responsible for catalyst deactivation[30]. The site requirements and mechanism of acetaldehyde synthesis, a critical component in understanding deactivation of ethanol conversion on acidic catalytic systems, was probed in this work with isotope labeling and in-situ chemical titration studies.

In this work, the observed reactant pressure dependencies of ethylene, DEE, acetaldehyde and ethane synthesis rates suggest that ethanol dehydrogenation operates by an indirect hydrogen transfer mechanism to form acetaldehyde and ethane and that observed rates are inhibited only by surface ethanol monomer species. The synthesis rates of ethylene, acetaldehyde, and ethane were inhibited to the same extent by pyridine, demonstrating that kinetic pathways for unimolecular dehydration and dehydrogenation of ethanol possess a common surface intermediate. The catalytic sites responsible for the bimolecular dehydration of ethanol were determined to be not equivalent to and possess a surface density an order of magnitude larger than those responsible for unimolecular dehydration using transient pyridine uptake measurements.

## 3.2 Materials and methods

### *3.2.1 Catalyst preparation*

$\gamma$-$Al_2O_3$ was used as purchased from the manufacturer (18HPa-150 Catalox, BET

surface area = 141 $m^2/g^{-1}$, pore volume = 0.786 $cm^3g^{-1}$) for each kinetic measurement. Catalyst particles between 180 and 420 μm (40-80 mesh) for steady state kinetic measurements at 623 K and between 180 and 250 μm (60-80 mesh) for all other measurements were collected after sieving compressed γ-$Al_2O_3$ powder. The catalysts particles were then individually counted and weighed to obtain the small catalyst amounts used in the kinetic measurements (0.3-1.0 mg). The catalyst bed was then combined with acid-washed quartz sand and treated in air as previously described[65]. Prior to each experiment, the catalyst was exposed to 2.2 kPa of deionized water in He (total flowrate = 1.7 $cm^3$ $s^{-1}$) to induce the previously observed partial deactivation of the catalytic surface by water adsorption[65].

*3.2.2 Steady state kinetic measurements of ethanol conversion over γ-$Al_2O_3$*

Steady state kinetic measurements of ethanol conversion on γ-$Al_2O_3$ were performed using the reactor system described previously[65]. Ethanol conversion kinetic measurements were carried out at 623 K, 648 K, and 673 K using a He carrier gas (Grade 4.7, Minneapolis Oxygen Company) with a flowrate of 9.9 $cm^3$ $s^{-1}$ at ambient pressure. An internal standard mixture of 25.0 % $CH_4$ with a balance of Ar (Minneapolis Oxygen Company) was also fed at 0.017 $cm^3$ $s^{-1}$ at NTP conditions for gas chromatography analysis. Differential conversion of ethanol (< 10%) was maintained by using 0.3-1.0 mg of catalyst at temperatures between 623 K and 673 K.

The partial pressure of ethanol (99.5% Decon Laboratories, Inc.) in the feed was

varied between 1.0 and 16.2 kPa for kinetic investigations and was maintained by controlling the liquid flowrate into the system. Pyridine (99+%, Sigma Aldrich) was similarly fed to maintain a feed partial pressure between 0.0 and 0.7 kPa for steady state pyridine inhibition measurements at 673 K. Kinetic isotope studies using $C_2H_5OD$ and $C_2D_5OD$ (99.5 at.% D, Sigma-Aldrich) reagents were done at 3.1 kPa partial pressure of the alcohol reactant. For all experiments, a deionized water co-feed was maintained between 0.5 and 1.7 kPa. All steady state kinetic measurements were compared and normalized to the initial experimental condition that was repeated after every change in the feed composition and was used as a reference to account for any deactivation of the catalyst during the reaction (Section 6.2).

The composition of the reactor effluent was determined using both a gas chromatograph (GC) and an on-line mass spectrometer (MS) as described previously[65]. Reported errors were determined by evaluating the 95% confidence interval of repeated titrations or successive GC measurements at the same experimental set points.

### *3.2.3 In-situ pyridine titration of catalytic sites responsible for ethanol dehydration*

The transient profile of ethylene and DEE production from the dehydration of 3.0 kPa of ethanol with a deionized water co-feed of 1.3 kPa over 0.0015 to 0.020 g of γ-$Al_2O_3$ at 623 K was measured using on-line mass spectrometry after the introduction of a steady 0.05-0.10 kPa stream of pyridine. The measured transient effluent composition profile was used with the evaluated kinetics for ethylene and DEE formation to determine

the uptake of pyridine necessary to completely deactivate both dehydration pathways and thereby estimate the surface density of catalytic sites responsible for the formation of the two products.

### *3.2.4 Evaluation of reported kinetic parameters*

The kinetic parameters presented in Table 7 were estimated by optimizing the model fits to the data presented in Section 3.1 using Bayesian statistical optimization techniques and the Athena Visual Studio (v14.2, W. E. Stewart and M. Caracotsios) statistical software package. The reported uncertainties represent the 95% marginal highest posterior density intervals. Experimental replicates were provided from repeated independent measurements of ethanol dehydration and dehydrogenation rates on fresh catalyst samples.

## 3.3 Results and discussion

### *3.3.1 Kinetics of ethylene, DEE, and acetaldehyde synthesis above 623 K*

The synthesis rates of ethylene and diethyl ether (DEE) from ethanol dehydration on $\gamma$-$Al_2O_3$ between 623 K and 673 K possess ethanol partial pressure dependences with an order between 0.2 and 0.6 for ethylene synthesis and between 0.6 and 1.5 for DEE synthesis (ethanol pressures between 1.0 and 16.2 kPa; Figure 11). Additionally, both ethylene and DEE synthesis rates are independent of co-fed water partial pressure at water pressures less than 1.7 kPa at these temperatures (Figure 12), consistent with

Langmuir-Hinshelwood mechanisms for both unimolecular and bimolecular ethanol dehydration pathways in which only the reactive precursor before the rate-limiting step (ethanol monomers for ethylene synthesis and ethanol dimers for DEE synthesis) inhibits observed rates.

In a previous report, we noted that both the unimolecular and bimolecular dehydration of ethanol on $\gamma$-$Al_2O_3$ at 488 K could be described by surface mechanisms in which the reactions were inhibited by dimer species composed of ethanol and water surface species[65]. The observed kinetic dependences on ethanol and water pressure suggest that dimeric surface species are not sufficiently stable at temperatures above 623 K to have a measurable effect on the rate of dehydration.

In addition to ethylene and DEE from the dehydration of ethanol at temperatures above 623 K, acetaldehyde is observed as a product of ethanol dehydrogenation on $\gamma$-$Al_2O_3$ at a rate that is more than two orders of magnitude slower than that of the unimolecular dehydration of ethanol. Acetaldehyde synthesis occurs at a rate that is independent of co-fed water partial pressure and possesses an ethanol partial pressure dependence of orders between 0.4 and 1.0 (Figures 11 and 12), indicating that, much like ethylene synthesis, acetaldehyde synthesis can be modeled considering a surface mechanism inhibited by only a reactive intermediate surface species.

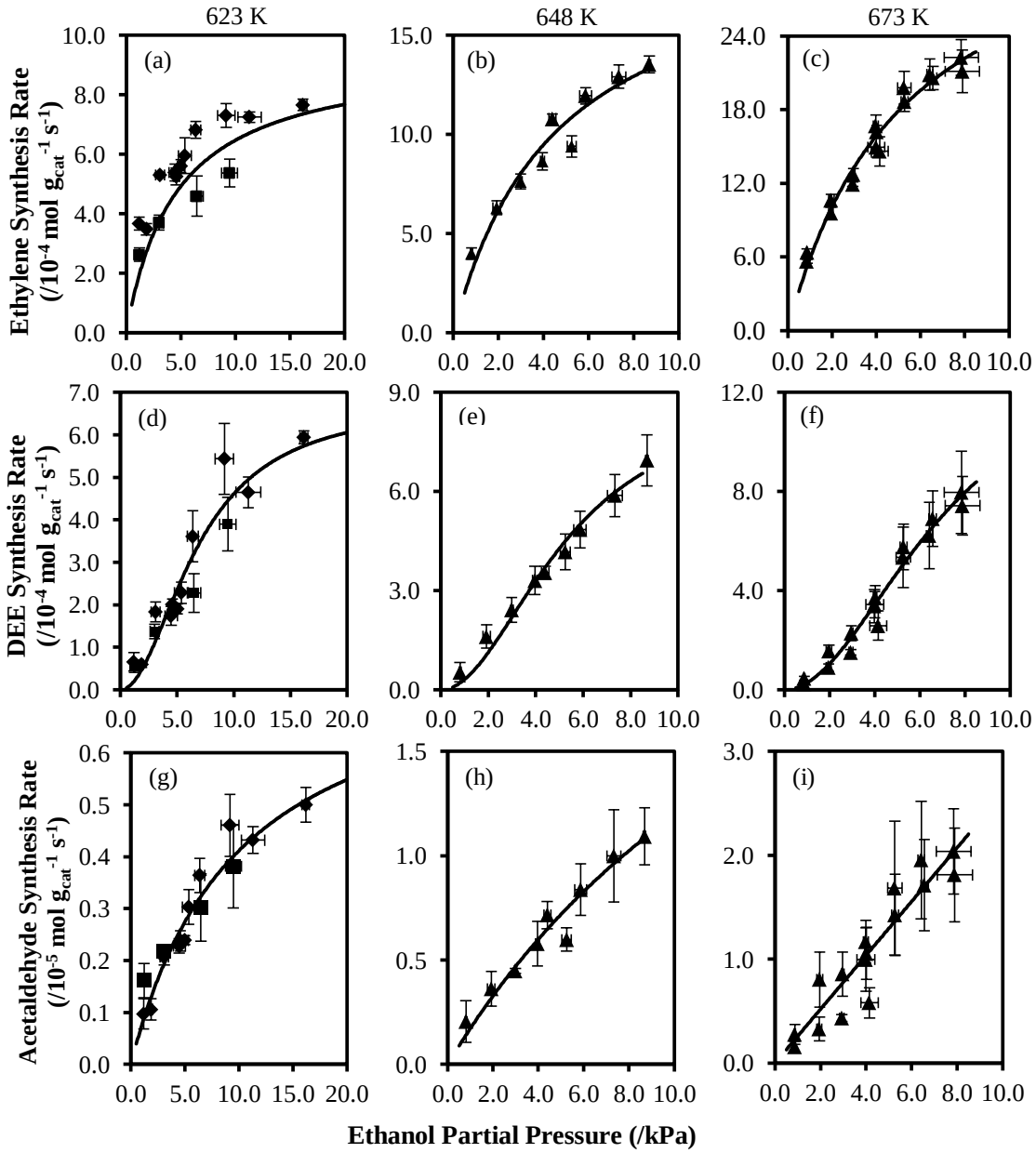


**Figure 11**. (a-c) Ethylene, (d-f) DEE, and (g-i) acetaldehyde synthesis rates as a function of ethanol pressure at (a,d,g) 623 K, (b,e,h) 648 K, and (c,f,i) 673 K and with 1.5 kPa (◆), 0.6 kPa (■), and 0.4 kPa (▲) of co-fed water partial pressure over (a,d,g) 1.0 mg, (b,e,h) 0.5 mg, and (c,f,i) 0.3 mg of γ-$Al_2O_3$ (total volumetric flowrate = 9.9 $cm^3$ $s^{-1}$). The solid lines represent model fits to Equations (a-c) 6, (d-f) 7, and (g-i) 8.

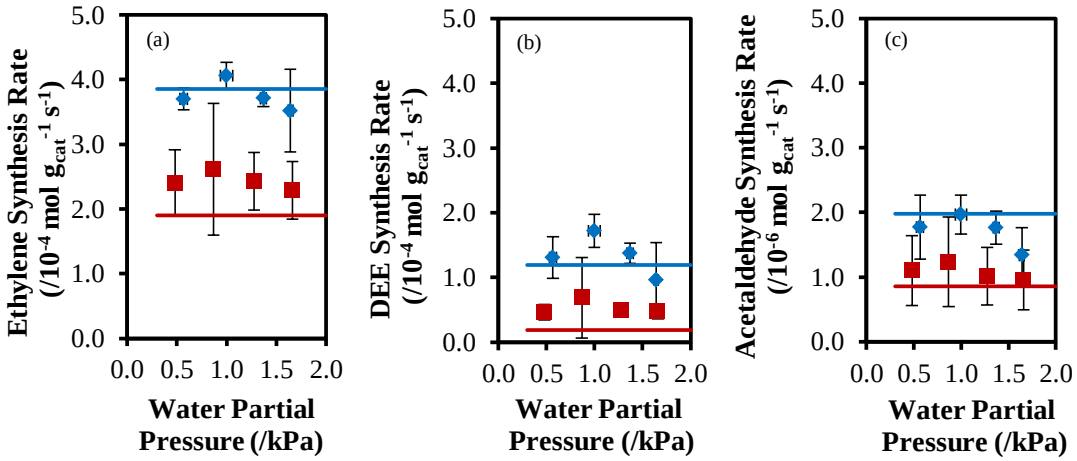


**Figure 12.** (a) Ethylene, (b) DEE, and (c) acetaldehyde synthesis rates from the conversion of 3.2 kPa (◆) and 1.2 kPa (■) of ethanol as a function of co-fed water partial pressure over 1.0 mg of γ-$Al_2O_3$ (total volumetric flowrate = 9.9 $cm^3$ $s^{-1}$) at 623 K. The solid lines represent model fits to Equations (a) 6, (b) 7, and (c) 8.

The kinetic models for ethylene, DEE, and acetaldehyde synthesis presented in Equations 6, 7, and 8, respectively can be derived by assuming that: (1) the rate-limiting step is the decomposition of a surface species to form each product[65], (2) the only significant surface species is the reactive surface intermediate (an ethanol monomer species for ethylene and acetaldehyde synthesis and a bimolecular co-adsorbed ethanol dimer species for DEE synthesis), and (3) these reactive surface intermediates are in quasi-equilibrium with gaseous ethanol.

$$r_{C_2H_4} = \frac{k_{C_2H_4} K_{A1} P_{EtOH}}{1 + K_{A1} P_{EtOH}} \tag{6}$$

$$r_{DEE} = \frac{k_{DEE} K_{A1} K_{A2} P_{EtOH}^2}{1 + K_{A1} K_{A2} P_{EtOH}^2} \tag{7}$$

$$r_{CH_3CHO} = \frac{k_{CH_3CHO} K_{A1} P_{EtOH}}{1 + K_{A1} P_{EtOH}} \tag{8}$$

$r_{C_2H_4}$, $r_{DEE}$, and $r_{CH_3CHO}$ are the synthesis rates of ethylene, DEE, and acetaldehyde, respectively. $k_{C_2H_4}$, $k_{DEE}$, and $k_{CH_3CHO}$ represent the intrinsic rate constants for each reaction. $K_{A1}$ represents the equilibrium constant of adsorption to form a reactive ethanol monomer surface species from gas phase ethanol, hypothesized to be either a surface ethoxy species[65] or a strongly adsorbed ethanol molecule[67], while $K_{A2}$ is the equilibrium constant for a second gas phase molecule to adsorb onto the first ethanol surface species to form a reactive co-adsorbed ethanol dimer surface species for DEE synthesis[65]. Finally, $P_{EtOH}$ is the gas phase ethanol pressure. The values of each of the kinetic parameters at 623 K, 648 K, and 673 K were estimated using the data presented in Figures 11 and 12 and are reported in Table 7. The solid lines in Figures 11 and 12 show the model fit to the experimental data. Parity, lag, and normal probability plots for the models at each temperature are presented in Section 6.3.

An alternative rate expression to the one presented in Equation 7 for DEE synthesis that includes the surface coverage of ethanol monomer species can also be proposed. This rate expression, however, does not statistically reduce the residual error or improve the model's ability to describe the measured kinetics over the one presented in Equation 7, indicating that the ethanol pressure range in which ethanol monomer species dominate the catalyst surface is relatively small compared to our ability to accurately measure the rate. The mathematically simpler model presented in Equation 7 was chosen as the rate expression to minimize the number of kinetic parameters needed to describe the

measured synthesis rates.

The high relative uncertainties of the reported equilibrium constants of adsorption are a result of the relatively few measured data points in which the coverage of reactive surface species is kinetically relevant. Over the majority of the tested ethanol pressures, the surface coverage of adsorbates was sparse and empty sites were the predominantly prevalent surface species. Furthermore, the coverage of reactive surface species for acetaldehyde synthesis was not observed to be kinetically relevant at any of the tested ethanol pressures at 673 K. Reactive precursors only became kinetically relevant at ethanol pressures above 5.0 kPa at 623 K.

The large uncertainty in acetaldehyde formation rates (Figures 11 and 12) and in the associated kinetic parameters (Table 7) are a result of the small amount of acetaldehyde generated in this process (<100 ppm of the effluent stream) making accurate

**Table 7**. Estimated values for the kinetic parameters of ethylene, DEE, and acetaldehyde formation over $\gamma$-$Al_2O_3$ at 623 K, 648 K, and 673 K using the models presented in Equations 6-8 and the data from Figures 11 and 12.

| **Parameter** | **Ethylene (Equation 6)** | | **DEE (Equation 7)** | | **Acetaldehyde (Equation 8)** | |
|---|---|---|---|---|---|---|
| | $k_{C_2H_4}$ ($/10^{-4}$ $mol_{C_2H_4}$ $s^{-1}$ $g^{-1}$) | $K_{A1}$ ($kPa^{-1}$) | $k_{DEE}$ ($/10^{-4}$ $mol_{DEE}$ $s^{-1}$ $g^{-1}$) | $K_{A1}K_{A2}$ ($kPa^{-2}$) | $k_{CH_3CHO}$ ($/10^{-5}$ $mol_{CH_3CHO}$ $s^{-1}$ $g^{-1}$) | $K_{A1}$ ($kPa^{-1}$) |
| **Value (623 K)** | 9.4 ± 3.3 | 0.22 ± 0.17 | 6.8 ± 1.2 | 0.021 ± 0.009 | 0.82 ± 0.19 | 0.10 ± 0.04 |
| **Value (648 K)** | 20.4 ± 6.5 | 0.22 ± 0.15 | 9.1 ± 1.8 | 0.035 ± 0.015 | 3.5 ± 3.6 | 0.05 ± 0.07 |
| **Value (673 K)** | 37.0 ± 5.9 | 0.19 ± 0.06 | 14.2 ± 3.6 | 0.020 ± 0.009 | $k_{CH_3CHO}K_{A1}$ = 0.26 ± 0.03 | |

quantitation difficult. The small concentrations, however, may still be sufficient to induce deactivation of the catalyst during reaction (Section 6.2).

*3.3.2 Kinetic isotope effects for the conversion of ethanol at 623 K*

Kinetic isotope effects (KIE) at 623 K for ethylene, DEE, and acetaldehyde from the conversion of $C_2H_5OD$ and $C_2D_5OD$ on $\gamma$-$Al_2O_3$ are reported in Table 8. A primary kinetic isotope effect ($k_H/k_D$ = 1.9) is observed for ethylene synthesis when $C_2D_5OD$ is fed but not when $C_2H_5OD$ is used as a reactant, verifying that either C-H bond cleavage or the removal of water from the $\gamma$-$Al_2O_3$ surface is rate limiting for unimolecular ethanol dehydration. Conversely, no kinetic isotope effect was observed for either labeled reactant for DEE synthesis, demonstrating that either C-O bond cleavage or Al-O bond cleavage of a surface intermediate is the rate-limiting step for the bimolecular dehydration of ethanol. These KIEs and conclusions are consistent with our previous investigation at 488 K[65] and with observed KIEs of the dehydration of deuterium-labeled methanol, *iso*-butanol, *tert*-butanol, and *sec*-butanol reported by Knözinger et al.[60,62].

**Table 8**. Measured kinetic isotope effects for ethylene and diethyl ether formation at 623 K for the dehydration of 3.1 kPa of $C_2H_5OD$ and $C_2D_5OD$ over 1.0 mg $\gamma$-$Al_2O_3$ and 1.5 kPa of water co-feed.

| Product \ Reactant | $C_2H_5OD$ | $C_2D_5OD$ |
|---|---|---|
| **Ethylene KIE ($r_H/r_D$)** | 0.99 ± 0.01 | 1.9 ± 0.1 |
| **Diethyl Ether KIE ($r_H/r_D$)** | 0.98 ± 0.03 | 1.0 ± 0.2 |
| **Acetaldehyde KIE ($r_H/r_D$)** | 1.09 ± 0.02 | 1.6 ± 0.2 |

DFT calculations (PW91 functional with generalized gradient approximation) of ethanol dehydration on $\gamma$-$Al_2O_3$ performed by Christiansen et al. also note that $C_\beta$-H bond cleavage is limiting in ethylene synthesis (activation energy = 37 kcal $mol^{-1}$) and that an $S_N2$ reaction step involving the cleavage of the C-O bond of ethanol is rate limiting in DEE synthesis (activation energy = 35 kcal $mol^{-1}$)[67].

Much like ethylene synthesis, a primary kinetic isotope effect was observed for acetaldehyde synthesis ($k_H/k_D$ = 1.6) only for the fully deuterated reactant and not for $C_2H_5OD$, indicating that acetaldehyde synthesis is similarly limited by the cleavage of either an O-H bond of a surface bound hydrogen adatom or a C-H bond. We postulate that ethanol dehydrogenation on $\gamma$-$Al_2O_3$ is limited by the cleavage of a $C_\alpha$-H bond of an adsorbed ethoxy species rather than by the cleavage of the $C_\beta$-H bond to form a surface enolate that subsequently undergoes rapid hydride transfer to form acetaldehyde. Measured KIEs of $(CH_3)_2CDOH$ dehydrogenation into acetone over Ni/$\gamma$-$Al_2O_3$ at 333 K observed by Shimizu et al.[68] ($k_H/k_D$ = 2.0) and over $Cr_2O_3$ at 623 K by Nondek and Sedláček ($k_H/k_D$ = 1.9)[69] mirror our proposed rate-limiting step for alcohol dehydrogenation on $\gamma$-$Al_2O_3$. Additionally, prominent infrared bands associated with surface ethoxy species (1000-1100 and 2800-3000 $cm^{-1}$) and the corresponding production of acetaldehyde was observed in in-situ IR spectroscopic measurements of $CeO_2$ in presence of flowing ethanol at 523 K by Li et al., leading the authors to also conclude that acetaldehyde synthesis is limited by the $C_\alpha$-H bond cleavage of an absorbed ethoxide species[70].

*3.3.3 Ethane synthesis and acetaldehyde formation mechanism*

Ethane is also seen as a product of ethanol conversion above 623 K and is synthesized at rates that are in a 1:1 ratio with acetaldehyde production within experimental error (Figure 13), signifying that ethane is a co-product of acetaldehyde synthesis. Ethane was also observed by Phung et al. as a product of ethanol conversion on $\gamma$-$Al_2O_3$ at 623 K with a similar selectivity (~1.0%)[33]. Furthermore, the synthesis rates of both ethane and acetaldehyde at 673 K are independent of co-fed ethylene pressure up to 1.5 kPa (Figure 14), indicating acetaldehyde is not formed by a direct hydrogen transfer pathway in which ethanol transfers hydrogen to ethylene in the rate-limiting step.

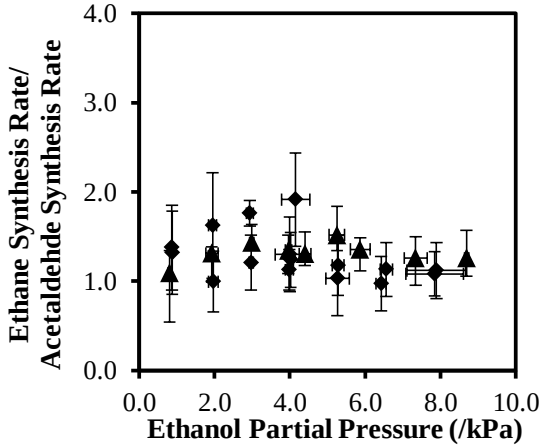


**Figure 13.** The ratio of the ethane and acetaldehyde synthesis rates formed from ethanol dehydrogenation over 0.3 mg of $\gamma$-$Al_2O_3$ (total volumetric flowrate = 9.9 $cm^3$ $s^{-1}$) at 648 K (▲) and 673 K (◆) with a water co-feed of 0.4 kPa as a function of ethanol pressure.

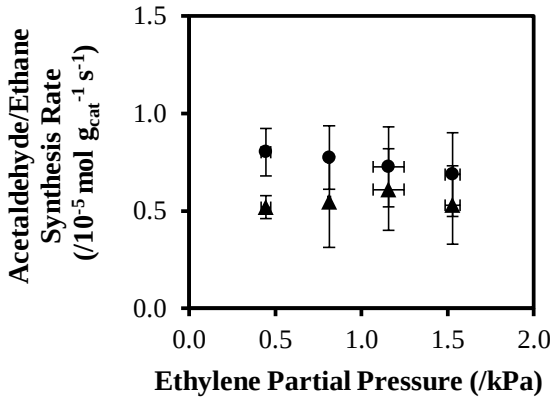


**Figure 15.** Acetaldehyde (▲) and ethane (●) synthesis rates from the conversion of 3.0 kPa of ethanol over 0.3 mg of γ-$Al_2O_3$ at 673 K with a water co-feed of 0.4 kPa as a function of co-fed ethylene partial pressure.

Two mechanisms for acetaldehyde synthesis consistent with the measured KIE for acetaldehyde formation, the 1:1 stoichiometric production of ethane, and the independence of acetaldehyde synthesis rates on ethylene partial pressure are presented in Figure 15. Figure 15a

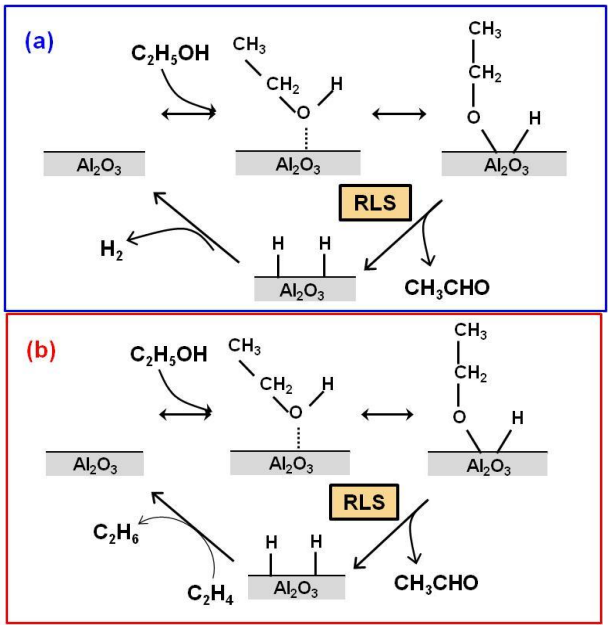


**Figure 14.** Acetaldehyde synthesis mechanisms from ethanol dehydrogenation over γ-$Al_2O_3$ through (a) a direct dehydrogenation pathway forming gaseous hydrogen and (b) an indirect hydrogen transfer pathway forming ethane.

shows the dehydrogenation of ethanol limited by $C_\alpha$-H bond cleavage of a surface ethoxy species to form acetaldehyde and two surface-bound hydrogen adatoms which subsequently desorb to form gas phase hydrogen. Ethylene would then undergo hydrogenation with the molecular hydrogen formed in a microscopic reverse of the dehydrogenation of alkanes investigated in DFT calculations by Wischert et al.[4,48] and as demonstrated in the reactive TPD experiments of ethylene-exposed $\gamma$-$Al_2O_3$ in the presence of hydrogen gas at room temperature by Amenomiya et al.[71]. Figure 15b displays an indirect hydrogen transfer mechanism which is also limited by the cleavage of the $C_\alpha$-H of a surface ethoxy species. Ethylene is instead hydrogenated by hydrogen adatoms to regenerate the catalytic surface. The synthesis of ethane was not observed to be catalyzed by $\gamma$-$Al_2O_3$ upon feeding 0.8 kPa of ethylene and 4.2 kPa of hydrogen in independent kinetic studies (hydrogen pressures used are 4000 times higher than the outlet pressure of acetaldehyde at 673 K), over 0.3 mg of catalyst at 673 K, favoring the indirect hydrogen transfer mechanism depicted in Figure 15b.

*3.3.4 Site density measurements for ethanol dehydration on $\gamma$-$Al_2O_3$*

Previously, we employed in-situ titration with pyridine to estimate the surface density of catalytic sites responsible for DEE formation at 488 K and under differential catalytic conditions (~0.1 sites $nm^{-2}$)[65]. At temperatures above 623 K, the small catalyst loading required to achieve differential ethanol conversions (~1.0 mg) is insufficient for accurate titration in the method previously described[65]; therefore, in-situ titrations with pyridine must be performed at higher conversions (up to 70%). The transient effluent composition of the reactor can be used to determine the active catalyst mass in the reactor using Equations 6-8 by assuming a plug flow reactor model. Assuming that far from equilibrium every molecule of pyridine that enters the bed of the reactor titrates a catalytically active site and that each active site contributes equally to the catalytic activity, the transient profile of the active catalyst mass should decrease linearly upon introduction to a constant feed of pyridine until an equilibrium coverage of pyridine is achieved (Figure 16). The total uptake of pyridine necessary to completely shut down the production of either ethylene or DEE was estimated by extrapolating this linear inhibition regime. The estimated pyridine surface density needed to completely deactivate the synthesis of ethylene and DEE and, thus, the density of catalytic sites responsible for these reactions at different pyridine pressures and catalyst loadings are presented in Table 9.

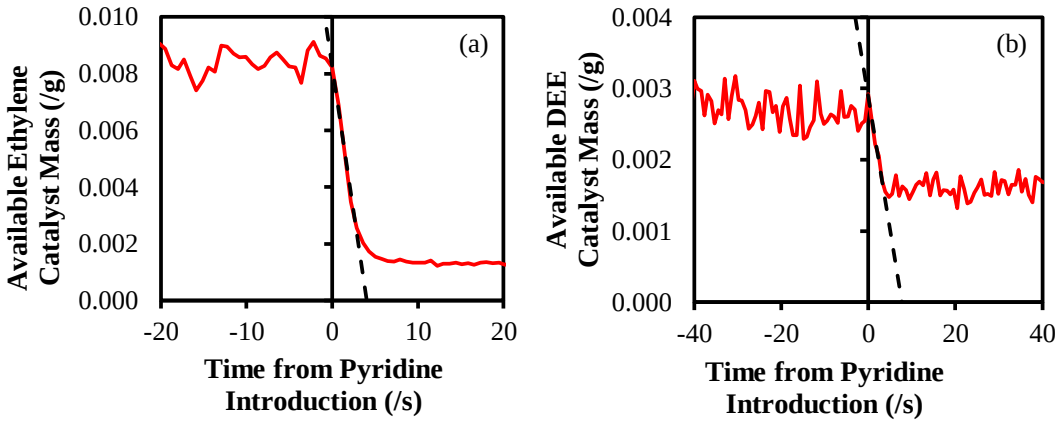


**Figure 16.** Available catalyst mass for the synthesis of (a) ethylene and (b) DEE from the dehydration of 3.0 kPa of ethanol on (a) 0.010 g and (b) 0.0022 g of γ-$Al_2O_3$ at 623 K with a 1.3 kPa water co-feed as function of time after introduction to 0.10 kPa of pyridine in the gas stream (total gas flowrate = 9.9 $cm^3$ $s^{-1}$). The available catalyst mass was estimated from Equations (a) 6 and (b) 7 and the parameters in Table 7. The dashed line shows the linear extrapolation used to estimate the total catalytic site density for ethylene synthesis.

The estimated density of catalytic sites responsible for the formation of ethylene was consistent within error across multiple catalyst loadings and pyridine pressure with an average site density of $(4.1 \pm 0.3)x10^{-5}$ mol $g^{-1}$ (~0.18 sites $nm^{-2}$). The estimated density of sites responsible for DEE synthesis appears to be a function of fed pyridine pressure, signifying that the estimated density has some systematic inaccuracies likely

**Table 9.** Catalytic site density for ethylene and DEE synthesis from ethanol dehydration on γ-$Al_2O_3$ at 623 K estimated from extrapolation of in-situ titrations using pyridine performed at different catalyst loadings and pyridine partial pressures. The reported errors are 95% confidence intervals determined using independent titrations.

| **Catalytic Site Density (/$10^{-5}$ mol $g^{-1}$)** | **Ethylene Synthesis** | | **DEE Synthesis** | |
|---|---|---|---|---|
| **Pyridine Pressure** | **0.020 g of Catalyst** | **0.010 g of Catalyst** | **0.0022 g of Catalyst** | **0.0015 g of Catalyst** |
| **0.10 kPa** | 4.2 ± 0.5 | 5.0 ± 0.9 | 51 ± 7 | 54 ± 33 |
| **0.05 kPa** | 3.8 ± 0.8 | 4.1 ± 0.0 | 32 ± 8 | 31 ± 4 |

caused by (i) uncertainties in the kinetic model for DEE synthesis causing the catalytic site density to be underestimated at lower pyridine pressures or (ii) non-uniformities in active site reactivities leading to an incomplete titration of less reactive surface sites at lower pyridine pressures. The average density of sites responsible for DEE production, however, is an order of magnitude greater than that of sites responsible for ethylene production, $(4.2 \pm 0.9)x10^{-4}$ mol $g^{-1}$ or ~1.8 sites $nm^{-2}$. The large difference in site densities is consistent with steady state kinetic measurements in presence of pyridine in previous investigations[65] which indicate that the sites that catalyze ethylene and DEE synthesis are not equivalent. These results are insufficient, however, to determine whether the sites responsible for ethylene synthesis are a subset of those responsible for DEE synthesis as pyridine is an unspecific titrant for the two dehydration pathways. The values presented in Table 9 represent an upper bound of catalytic site density as pyridine could also be adsorbing onto non-catalytic surface sites in addition to the active sites. This technique, however, presents a method to estimate the density of catalytic active sites under reaction conditions and, thus, is useful as a probe for assessing catalytic site requirements and can provide a more realistic estimate of surface density than ex-situ measurements. The structure of the active sites is not elucidated using this technique and other analytical techniques will need to be applied to provide a complete picture of the catalytic system.

The density of sites responsible for DEE synthesis at 488 K was estimated to be ~0.1 sites $nm^{-2}$ in previous investigations using the same in-situ titration technique, an

order of magnitude less than the density estimated at 623 K[65]. This increase in active site density with temperature is reflected in DFT calculations (PW91 functional) by Digne et al. in which the stable surface coverage of hydroxyl groups formed from dissociated water decreased from 8.8 to 0 OH $nm^{-2}$ and from 11.8 to 8.9 OH $nm^{-2}$ on the (100) and (110) facets of $\gamma$-$Al_2O_3$, respectively, upon increasing the temperature from 488 K to 623 K[41,42]. We postulate that the additional surface Al atoms on the dehydrated $\gamma$-$Al_2O_3$ surface at 623 K act as catalytic sites for DEE synthesis and explain the estimated increase in site density. Weak Lewis acid sites that become catalytically active only at elevated temperatures present another potential source for the additional catalytic sites measured at 623 K.

### *3.3.5 Site requirements for acetaldehyde synthesis on $\gamma$-$Al_2O_3$*

Pyridine was found to inhibit the syntheses of ethylene and DEE to different extents at 488 K, indicating that the catalytic sites of unimolecular and bimolecular ethanol dehydration are both acidic and non-equivalent[65]. This result is consistent with steady state kinetic measurements of ethanol conversion in presence of pyridine on $\gamma$-$Al_2O_3$ at 673 K (Figure 17). The appearance of multiple infrared adsorption bands around 1450 $cm^{-1}$ upon the exposure of pyridine to $\gamma$-$Al_2O_3$ led Parry[43] and Morterra and Magnacca[3] to conclude that acid sites with a distribution of strengths are present on the catalyst surface. A distribution of water adsorption and dissociation energies and, thus, acid site strengths on the $\gamma$-$Al_2O_3$ surface was also observed in DFT calculations (PW 91 functional) by

Digne et al.[42] and Wischert et al.[4], supporting the conclusion that different sets of catalytic sites exist on the surface of $\gamma$-$Al_2O_3$. Additionally, simulated and experimental $^{1}\{H\}^{27}Al$ cross-polarization nuclear magnetic resonance (NMR) measurements performed by Wischert et al. found that both chemical shift (10-70 ppm) and quadropolar coupling constants (5-38 MHz) are dependent on surface aluminum atom coordination and hydration state and that a distribution of these NMR parameters and, thus, potential catalytic sites can be observed on the $\gamma$-$Al_2O_3$ samples treated at 573 and 773 K[72].

Acetaldehyde, ethylene, and ethane production are inhibited to the same extent by pyridine (Figure 17), leading us to infer that acetaldehyde and ethane formation requires acidic surface sites and that the synthesis mechanisms of both acetaldehyde and ethylene proceed through a common surface intermediate. Surface ethoxy species present one

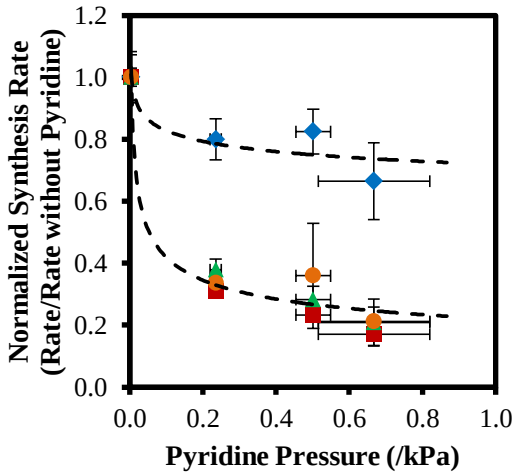


**Figure 17.** Ethylene (■), DEE (◆), acetaldehyde (▲), and ethane (●) synthesis rates from the conversion of 3.3 kPa of ethanol over 0.3 mg of $\gamma$-$Al_2O_3$ at 673 K with a 0.5 kPa co-feed of water normalized to the synthesis rates observed in the absence of pyridine plotted as a function of pyridine partial pressure. The dashed lines serve as a guide for the eye.

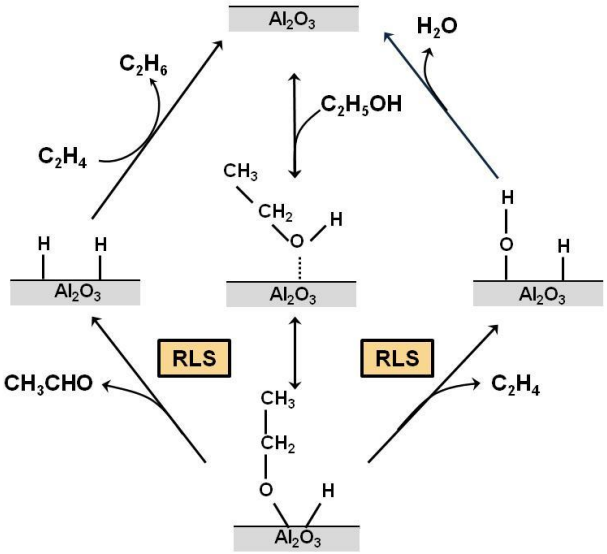


**Figure 18**. Proposed mechanism for the combined synthesis pathways of ethylene and acetaldehyde from a common ethoxy surface intermediate on $\gamma$-$Al_2O_3$.

possible surface intermediate that can act as a precursor to both ethylene and acetaldehyde synthesis (Figure 18). The relative synthesis rates of ethylene and acetaldehyde are therefore determined by the rates of $C_\beta$-H and $C_\alpha$-H bond scission, respectively, of this common surface ethoxy intermediate, consistent with the measured KIEs for ethanol conversion at 623 K (Table 8).

Christiansen et al. found using periodic DFT calculations (PW91 functional) that ethylene synthesis proceeds by the simultaneous cleavage of the $C_\beta$-H bond and C-O bond of an adsorbed ethanol molecule on the $\gamma$-$Al_2O_3$ surface rather than through a surface ethoxy intermediate[67]. This mechanism for ethylene synthesis is also consistent with the data presented in Figure 17 and with the conclusion that ethylene and acetaldehyde synthesis share a common reactive intermediate, in this case an absorbed ethanol molecule instead of an ethoxy intermediate. In this kinetically equivalent

alternative mechanism: (1) acetaldehyde synthesis proceeds through the cleavage of the $C_\alpha$-H bond of a surface ethoxy species that was formed from an absorbed ethanol molecule (as seen in Figures 15 and 18), (2) ethylene synthesis would be kinetically limited by the simultaneous cleavage of the $C_\beta$-H bond and the C-O bond of an adsorbed ethanol molecule, and (3) pyridine would inhibit the adsorption of ethanol onto this shared catalytic site, thereby inhibiting acetaldehyde, ethane, and ethylene synthesis equivalently.

The inhibitory effects by pyridine, measured KIE, and steady state kinetics elucidate the role acidic surface sites, surface bound ethoxy intermediates, and the indirect transfer of hydrogen adatoms to ethylene play in ethanol dehydrogenation on γ-$Al_2O_3$ above 623 K. These conclusions offer crucial considerations for catalytic design of Lewis acidic systems to avoid the synthesis of aldehydes that may be responsible for catalyst deactivation[30,31].

### 3.4 Conclusions

Steady state kinetic measurements of ethanol dehydration and dehydrogenation reactions on γ-$Al_2O_3$ above 623 K reveal: (1) the rates of formation of ethylene, DEE, and acetaldehyde are independent of co-fed water partial pressure, (2) the synthesis rates of ethylene and acetaldehyde possess an order between 0 and 1 for ethanol partial pressure, and (3) the synthesis rate of DEE possesses an ethanol order between 0 and 2. These observations imply that rates of ethylene, DEE, and acetaldehyde formation can be

described by a surface catalyzed mechanism inhibited only by reactive precursors, ethanol monomer species for ethylene and acetaldehyde syntheses and co-adsorbed ethanol dimer species for DEE synthesis, above 623 K. Primary kinetic isotope effects were observed for ethylene and acetaldehyde synthesis at 623 K when $C_2D_5OD$ was used as a reactant but not when $C_2H_5OD$ was used, verifying that the cleavage of a C-H bond is rate limiting for the synthesis of these products, likely the $C_\beta$-H bond for ethylene formation and the $C_\alpha$-H bond for acetaldehyde formation. A kinetic isotope effect was not measured for DEE synthesis at 623 K using either reactant, signifying that the C-O bond of ethanol is cleaved in the rate-limiting step of DEE synthesis. Ethane is produced with the same selectivity as acetaldehyde, indicating that ethane is a co-product of ethanol dehydrogenation. The surface densities of the catalytic sites responsible for ethylene and DEE synthesis on $\gamma$-$Al_2O_3$ at 623 K were estimated to be 0.18 and 1.8 sites $nm^{-2}$, respectively, using in-situ titration with pyridine. Ethylene, acetaldehyde, and ethane syntheses are inhibited to the same extent by pyridine, demonstrating that ethylene and acetaldehyde formation occur though a shared reactive intermediate. An indirect hydrogen transfer mechanism for acetaldehyde synthesis which proceeds through a shared ethoxy intermediate with ethylene synthesis and in which hydrogen adatoms are transferred to ethylene after the rate-limiting step to regenerate the catalyst surface is consistent with the presented conclusions.

**Acknowledgements**

Financial support from The Dow Chemical Company is gratefully acknowledged. We also would like to acknowledge Christopher Czopinski, Marcello Herrera, and Minje Kang for their support in creating catalyst weight and gas chromatograph calibrations, for loading and running this reactor system, and for testing the hydrogenation of ethylene on this catalyst. Reprinted with permission from DeWilde et al., *ACS Catal.* **2014**, *4* (12), pp 4425–4433. Copyright 2014 American Chemical Society.

# *Chapter 4: Kinetics and Site Requirements of Ether Disproportionation on γ-$Al_2O_3$*

## 4.1 Introduction

Alcohols dehydrate over acid catalysts, such as gamma-alumina (γ-$Al_2O_3$)[1,2,36,50,51,58,64], to form olefins and water through a unimolecular pathway or ethers and water through a bimolecular pathway[5,12,13,17,18,20,22,23,57,60,62,73-75]. In previous investigations, pyridine inhibition measurements identified that these parallel alcohol dehydration pathways occur on non-equivalent pools of catalytic sites; concurrently kinetic measurements have demonstrated that, at 488 K, alcohol dehydration is inhibited by non-reactive multimers while at temperatures greater than 623 K the surface is primarily covered with reactive precursors[65,76,77]. Specifically, olefin production from the dehydration of ethanol, 1-propanol, isopropanol, and isobutanol at 488 K was observed to be inhibited by surface dimers composed of alcohol and water while ether synthesis was inhibited by surface trimer species at alcohol pressures larger than 4.2 kPa[77]. The proposed presence of surface multimers at low temperatures is consistent with kinetic measurements of propylene synthesis from 2-propanol dehydration at 373-433 K by De Morgues et al.[11] which demonstrated that the rate of propylene synthesis was independent of 2-propanol pressure above 1.1 kPa while simultaneously being inhibited by co-fed water at water partial pressures below 1.2 kPa. In addition to alcohol dehydration, ethers can also convert on γ-$Al_2O_3$ through two possible reaction pathways: (i) ether hydration,

the reverse reaction pathway of bimolecular alcohol dehydration, and (ii) direct ether disproportionation to form an olefin and an alcohol[16,33-35]. In this work, we identify the prominent ether conversion pathway at 623 K as well as elucidate its kinetics (including the prominent surface species present during reaction) and mechanism.

Negligible quantities of ether were observed from ethanol reactions at 623 K on γ-$Al_2O_3$ at conversions greater than 99% in investigations by Phung et al.[33], suggesting that ether conversion pathways exist on γ-$Al_2O_3$. Reactor effluent DEE partial pressure was observed to go through a maximum with increasing contact time over a bed of γ-$Al_2O_3$ at 571 and 616 K in steady state kinetic measurements of ethanol dehydration by Knözinger and Köhne[34]. The authors additionally observed that, initially (<10% conversion), ethylene and ethanol were synthesized in a nearly 1:1 stoichiometric ratio in kinetic measurements of ether conversion as a function of increasing temperature, and thus conversion, leading them to postulate that ether disproportionation presents a significant ether decomposition pathway on γ-$Al_2O_3$[34]. The 1:1 stoichiometric production of ethylene and ethanol from DEE conversion on γ-$Al_2O_3$ was also observed in more recent investigations at 573 K by Phung and Busca[35]. Similarly, Morávek and Kraus[16] observed nearly equal steady state production of ethylene and ethanol with a much smaller production rate of water from the conversion of DEE on alumina at 523 K, consistent with a prominent ether disproportionation pathway on alumina materials. Furthermore, ethylene synthesis persisted after the DEE feed was stopped, leading the authors to infer that ether disproportionation occurs through the formation of persistent surface alkoxides

that desorb to form ethylene[16]. In more recent investigations, density functional theory (DFT) calculations by Christiansen et al.[67] show that DEE disproportionates on the γ-$Al_2O_3$ surface with an activation energy nearly identical to that of ethylene synthesis from ethanol dehydration (38 and 37 kcal $mol^{-1}$, respectively), consistent with the authors proposal that the rate-limiting step for the two reactions is similar.

DFT calculations (PW 91 functional) of the adsorption and dissociation energies of water on a variety of surface sites on γ-$Al_2O_3$ by both Wischert et al.[4] and Digne et al.[42] noted that these energies were dependent on the coordination of the surface aluminum atom and facet onto which the water molecule adsorbed, demonstrating that the surface of γ-$Al_2O_3$ possesses a distribution of active sites with varying acidities. Moreover, heats of water emersion on alumina samples outgassed at different temperatures (100-600 °C) measured by Hendriksen et al.[49] reveal that the differential heats of adsorption of water decrease (55 to 20 kcal $mol^{-1}$) as the surface hydration of the alumina surface increases, consistent with these computational results. The presence of a distribution in acid site strength was also experimentally observed in both (i) infrared spectroscopic measurements by Morterra and Magnacca[3] as well as independently by Parry[43] and (ii) in $^{15}N$ nuclear magnetic resonance measurements by Ripmeester[44] of pyridine-exposed γ-$Al_2O_3$ samples in which multiple (i) vibrational bands around 1450 $cm^{-1}$ and (ii) peaks with chemical shifts 110 and 134 ppm were attributed to pyridine adsorption onto Lewis acid sites of varying strengths. Similarly, multiple infrared vibrational bands (2238, 2200, and 2165 $cm^{-1}$) on CO-exposed γ-$Al_2O_3$ samples measured

by Zecchina et al.[78], verify the non-uniformity of the γ-$Al_2O_3$ surface. Wischert et al.[72] further supported these conclusions with $^{1}\{H\}^{27}Al$ cross-polarization nuclear magnetic resonance measurements in which a range of both the measured chemical shift (between 10 and 70 ppm) and quadropolar coupling constants (between 5 and 38 MHz) were noted on γ-$Al_2O_3$ samples that were treated at 573 and 773 K. The area of a peak at ~23 ppm attributed to penta-coordinated aluminum atoms was observed to decrease with BaO loading in $^{27}Al$ nuclear magnetic resonance measurements by Kwak et al.[57] on BaO/γ-$Al_2O_3$; peaks attributed to octahedral (0 ppm reference in this study) and tetrahedral (~59 ppm) aluminum atoms were unaffected by the BaO loading. The rate of methanol dehydration to synthesize DME decreased monotonically with BaO loading on these catalytic systems[22], suggesting that these penta-coordinated sites on γ-$Al_2O_3$ are active for ether synthesis. While olefin synthesis was not investigated in these studies, these experiments suggest that multiple types of potential catalytic sites exist on γ-$Al_2O_3$. The diversity and number of acid sites is expected to be a function of temperature and water partial pressure and, based on our prior reports, results in at least two distinct sets of catalytic centers, one which catalyze unimolecular alcohol dehydration and dehydrogenation reactions and another which catalyzes bimolecular alcohol dehydration reactions[65,76]. We report in this study that ether disproportionation occurs on sites that catalyze unimolecular alcohol conversion.

In this investigation, kinetic measurements of methyl propyl ether (MPE), an asymmetric ether, verify that ether disproportionation, rather than ether hydration, is the

predominant ether conversion pathway on γ-$Al_2O_3$ at water partial pressures below 2.0 kPa. Measured DEE disproportion rates are independent of co-fed water partial pressure and are consistent with a proposed mechanism in which reactive DEE-derived ethoxy groups and inhibitory ethanol monomers are the prominent surface species. In-situ pyridine inhibition experiments are used to affirm that the catalytic sites responsible for DEE disproportionation possess similar site requirements and densities (0.3 and 0.2 sites $nm^{-2}$, respectively) as ethylene synthesis from ethanol dehydration.

## 4.2 Materials and methods

### *4.2.1 Catalyst preparation*

Kinetic measurements were carried out on γ-$Al_2O_3$ purchased from the manufacturer (18HPa-150 Catalox, BET surface area = 141 $m^2/g^{-1}$, pore volume = 0.786 $cm^3g^{-1}$). Two batches of catalyst particles, one with particle sizes between 180 and 420 μm (40-80 mesh) for reactions of DEE, ethanol, and water mixtures and one with particle sizes between 180 and 250 μm (60-80 mesh) for measuring MPE kinetics and pyridine inhibition, were prepared by pressing and subsequently sieving γ-$Al_2O_3$ powder. The desired catalyst mass (~1.0 mg) was obtained by individually counting catalyst particles and adding them to a quartz tube reactor filled with acid-washed quartz sand as described in previous reports[65,76]. The catalyst beds were then treated in air and subsequently exposed to 2.2 kPa of water prior to reaction as described previously[76].

*4.2.2 Steady state kinetic measurements*

The reactor system described in previous reports[65,76] was used to gather steady state kinetic measurements on ether conversion. All experiments were performed at a reaction temperature of 623 K using a mixture of liquid feeds, a He carrier gas (Grade 4.7, Minneapolis Oxygen Company) with a flowrate of 9.9 $cm^3\ s^{-1}$ at ambient pressure, and a mixture of 25.0 % $CH_4$ with a balance of Ar (Minneapolis Oxygen Company) fed at 0.017 $cm^3\ s^{-1}$ at ambient pressure to act as an internal standard for gas chromatography analysis. Ether conversions were kept to differential levels (< 10%) by using reactor beds containing 1.0 mg of catalyst.

MPE (97% Sigma Aldrich with 3% methanol as stabilizer) was fed to and vaporized in a flowing He stream to maintain a pressure of 0.8 kPa for kinetic measurements of asymmetric ether conversion. Methanol (99.9% Fisher Scientific) was also fed in these experiments to maintain a partial pressure of 0.2 kPa throughout the catalyst bed. Methanol and 1-PrOH dehydration kinetics were measured in independent investigations by feeding 2.4 to 16.8 kPa of methanol and 1.4 to 9.4 kPa of 1-PrOH (99.9% Sigma Aldrich). Similarly, the kinetics of DEE conversion were measured by varying the partial pressure of ethanol-stabilized DEE (98.1% DEE with 1.0% ethanol Fisher Scientific) between 0.4 and 8.8 kPa. Pyridine inhibition measurements were carried out at 0.02 to 0.08 kPa of pyridine (99+%, Sigma Aldrich) with a co-feed of non-stabilized DEE (99.9% Sigma Aldrich) at 1.4 kPa as well as, in an independent

experiment, a co-feed of 3.5 kPa of ethanol and 1.3 kPa of water. For all experiments used to evaluate alcohol and ether conversion kinetics as well as pyridine inhibition measurements, deionized water was co-fed to establish feed partial pressures between 0.2 and 2.1 kPa.

The composition of the reactor effluent was determined using an online gas chromatograph (GC) with previously describe analytical protocols[65]. The 95% confidence intervals reported in the tables and figures were evaluated from subsequent GC measurements at the same experimental conditions.

*4.2.3 In-situ chemical titrations using pyridine*

Steady state rates and transient profiles of the effluent composition during DEE conversion were measured using an online mass spectrometer on 0.005-0.010 g of γ-$Al_2O_3$ at 623 K and with a 1.5 kPa DEE feed upon the introduction of 0.02-0.05 kPa of pyridine to the feed. These profiles were used to determine the effective catalyst mass that is active for DEE disproportionation in the reactor, as described previously for ethanol dehydration[76]. The density of active sites for DEE disproportionation was estimated by linearly extrapolating the inhibition profile and determining the surface density of pyridine necessary to completely deactivate the DEE disproportionation rate, as shown in previous reports[65,76,77].

*4.2.4 Estimation of kinetic parameters*

Bayesian statistical optimization techniques in the Athena Visual Studio statistical software package (v14.2, W. E. Stewart and M. Caracotsios) were employed to estimate reported kinetic parameters. Calculated 95% marginal highest posterior density intervals were used to determine the reported uncertainties. Independent measurements at the same reactant partial pressures acted as experimental replicates for parameter estimation.

## 4.3 Results and discussion

*4.3.1 Kinetic measurements of MPE conversion*

The product distribution of asymmetric ethers, such as MPE, allow for the rates of ether disproportionation to be deconvoluted from the rates of ether hydration because different products result from the two reactions. The hydration of MPE yields both methanol and propanol while MPE disproportionation will yield methanol and propylene. The rates of ether hydration, $r_{hyd}$, and ether disproportionation, $r_{dis}$, in a differential packed-bed reactor can therefore, be evaluated using Equations 9 and 10 (Figure 19).

$$r_{hyd} = r_{PrOH} + r_{PrOH\ to\ DPE} + r_{PrOH\ to\ C_3H_6} - r_{MPE+MeOH} \quad (9)$$

$$r_{dis} = r_{C_3H_6} - r_{PrOH\ to\ C_3H_6} \quad (10)$$

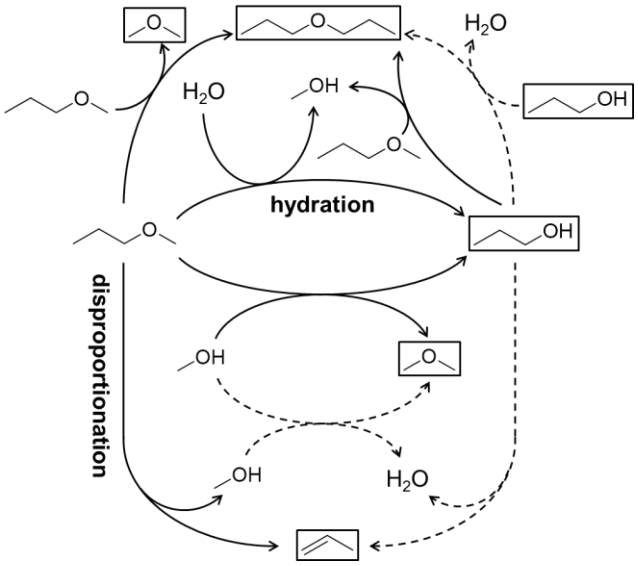


**Figure 19.** Proposed reaction network for MPE conversion on $\gamma$-$Al_2O_3$. The effluent concentrations of compounds highlighted in boxes were measured experimentally, while the other compounds were fed to the reactor. The reactions indicated by dashed arrows signify reactions that were evaluated in independent kinetic measurements.

$r_{C_3H_6}$ and $r_{PrOH}$ represent the net rates of propylene and 1-propanol synthesis, respectively; $r_{PrOH\ to\ DPE}$ and $r_{PrOH\ to\ C_3H_6}$ are the rates of bimolecular and unimolecular 1-propanol dehydration to synthesize dipropyl ether (DPE) and propylene, respectively; and $r_{MPE+MeOH}$ signifies the reaction rate of MPE and methanol to form dimethyl ether (DME) and 1-propanol. The rate of this reaction is given by Equation 11.

$$r_{MPE+MeOH} = r_{DME} - r_{MeOH\ to\ DME} - (r_{DPE} - r_{PrOH\ to\ DPE}) \quad (11)$$

$r_{DME}$ and $r_{DPE}$ are the net rates of DME and DPE synthesis, respectively; $r_{MeOH\ to\ DME}$ represents the rate of methanol dehydration to synthesize DME. The term in the parentheses signifies the rate of DME formation from the reaction of two MPE molecules to form DPE and DME. The reaction sequence described in Equations 9-11 is shown in

Figure 19 and Equations 12-18.

$$C_3H_7OCH_3 + H_2O \rightarrow C_3H_7OH + CH_3OH \quad (12)$$

$$C_3H_7OCH_3 \rightarrow C_3H_6 + CH_3OH \quad (13)$$

$$C_3H_7OCH_3 + CH_3OH \rightarrow C_3H_7OH + CH_3OCH_3 \quad (14)$$

$$2\ C_3H_7OCH_3 \rightarrow C_3H_7OC_3H_7 + CH_3OCH_3 \quad (15)$$

$$2\ CH_3OH \rightarrow CH_3OCH_3 + H_2O \quad (16)$$

$$2\ C_3H_7OH \rightarrow C_3H_7OC_3H_7 + H_2O \quad (17)$$

$$C_3H_7OH \rightarrow C_3H_6 + H_2O \quad (18)$$

Equations 9-11 contain three rates that are not directly measurable in a steady state kinetic measurement of MPE conversion and, thus, were evaluated in independent kinetic measurements: the unimolecular and bimolecular dehydration rates of 1-propanol to synthesize propylene and DPE, respectively, and the dehydration rate of methanol to DME.

The 1-propanol reaction order of the measured propylene synthesis rate from the unimolecular dehydration of 1-propanol on $\gamma$-$Al_2O_3$ at 623 K decreases from 0.6 to 0.4 as the 1-propanol pressure increases from 1.4 to 9.4 kPa (Figure 20a). The reaction order of DPE synthesis from bimolecular 1-propanol dehydration also decreases with increasing alcohol partial pressure (decreasing from 1.7 to 0.7 between 1.4 and 9.4 kPa of 1-propanol; Figure 20b). The methanol order of DME synthesis decreases from 0.9 to 0.7 as methanol pressure is increased from 2.4 to 15.8 kPa (Figure 20c). All dehydration rates at 623 K were observed to be independent of water partial pressure at water partial

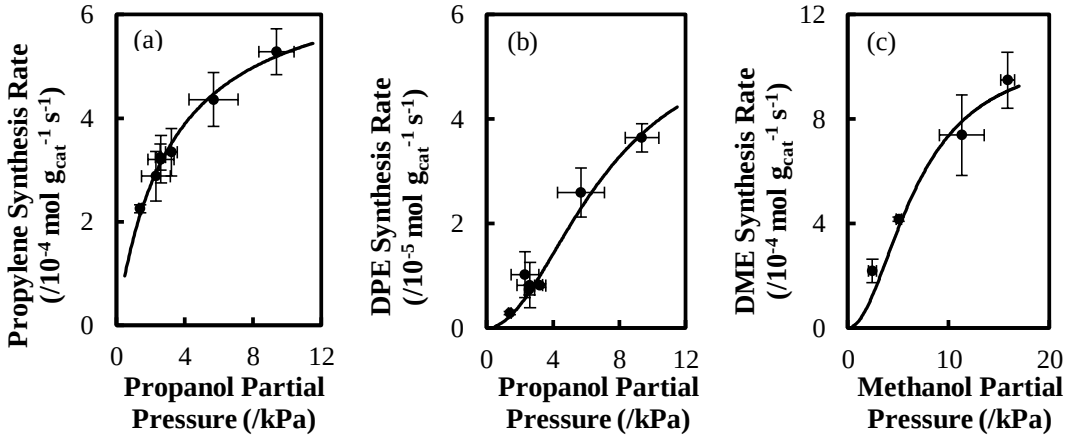


**Figure 20.** (a) Propylene, (b) DPE, and (c) DME synthesis rates over 1.0 mg $\gamma$-$Al_2O_3$ (total volumetric flowrate = 9.9 $cm^3$ $s^{-1}$) at 623 K as a function of fed (a,b) 1-propanol and (c) methanol partial pressure with a co-feed of (a,b) 0.7 kPa or (c) 1.5 kPa of water. Solid lines show kinetic model fits to Equations (a) 19 and (b,c) 20.

pressures up to 2.3 kPa (Figure 21).

The dehydration kinetics of 1-propanol and methanol match previous investigations of ethanol dehydration on $\gamma$-$Al_2O_3$ at 623 K in which dehydration rates were found to be consistent with a mechanism in which only reactive precursors (alcohol monomers for olefin synthesis and alcohol dimers for ether synthesis) cover the active sites during reaction[76]. The rate expressions shown in Equations 19 and 20 can be derived assuming that the reactive precursors prior to the rate-limiting step are the only prominent surface species and are in quasi-equilibrium with the alcohol in the vapor phase.

$$r_{olefin} = \frac{k_{olefin} K_{A1} P_{Alcohol}}{1 + K_{A1} P_{Alcohol}} \tag{19}$$

$$r_{ether} = \frac{k_{ether} K_{A1} K_{A2} P_{Alcohol}^2}{1 + K_{A1} K_{A2} P_{Alcohol}^2} \tag{20}$$

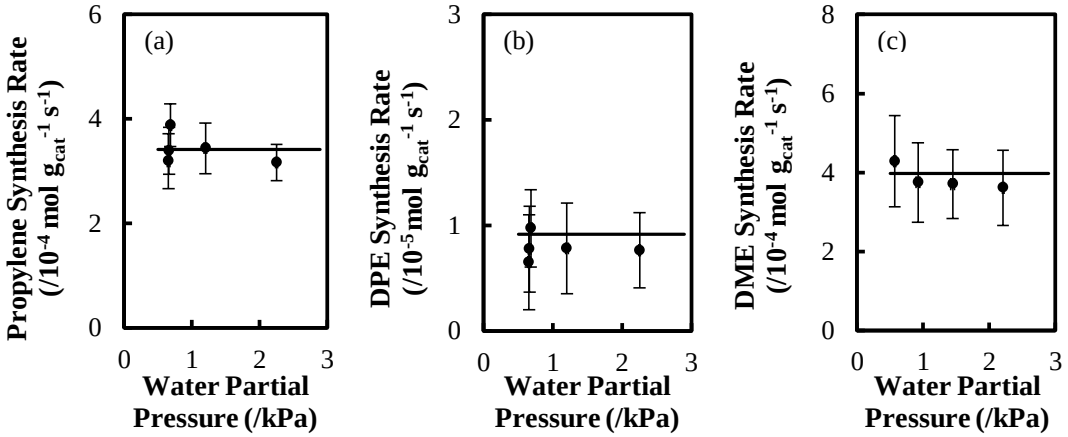


**Figure 21**. (a) Propylene, (b) DPE, and (c) DME synthesis rates from the conversion of (a,b) 3.0 kPa of 1-propanol and (c) 5.2 kPa of methanol over 1.0 mg $\gamma$-$Al_2O_3$ (total volumetric flowrate = 9.9 $cm^3$ $s^{-1}$) at 623 K as a function of water partial pressure. Solid lines show model fits to Equations (a) 19 and (b,c) 20.

**Table 10.** Kinetic parameters corresponding to models for unimolecular and bimolecular dehydration shown in Equations 19 and 20 for the synthesis of propylene, DPE, and DME from alcohol dehydration on $\gamma$-$Al_2O_3$ at 623 K estimated from the data presented in Figures 20 and 21.

| **Propylene (Equation 19)** | | **Dipropyl Ether (Equation 20)** | | **Dimethyl Ether (Equation 20)** | |
|---|---|---|---|---|---|
| $k_{olefin}$ ($/10^{-4}$ $mol_{C_3H_6}$ $s^{-1}$ $g^{-1}$) | $K_{A1}$ ($kPa^{-1}$) | $k_{ether}$ ($/10^{-5}$ $mol_{DPE}$ $s^{-1}$ $g^{-1}$) | $K_{A1}K_{A2}$ ($kPa^{-2}$) | $k_{ether}$ ($/10^{-4}$ $mol_{DME}$ $s^{-1}$ $g^{-1}$) | $K_{A1}K_{A2}$ ($kPa^{-2}$) |
| 6.9 ± 0.9 | 0.32 ± 0.09 | 5.8 ± 1.5 | 0.020 ± 0.009 | 11 ± 2 | 0.022 ± 0.009 |

$r_{olefin}$ and $r_{ether}$ are the olefin and ether synthesis rates. $k_{olefin}$ and $k_{ether}$ signify the intrinsic rate constants for unimolecular and bimolecular alcohol dehydration, respectively. The equilibrium constant to form a surface alcohol monomer is signified by $K_{A1}$ while $K_{A2}$ represents the equilibrium constant for the adsorption of another alcohol molecule to the reactive monomer to form a surface alcohol dimer. $P_{Alcohol}$ represents the

alcohol partial pressure in the catalyst bed. Table 10 summarizes the kinetic parameters of Equations 19 and 20 for 1-propanol and methanol dehydration estimated from the data presented in Figures 20 and 21. Solid lines in Figures 20 and 21 show the models presented Equations 19 and 20 with the estimated kinetic parameters from Table 10. Parity, lag, and normal probability plots for the kinetic models for each reaction are presented in Section 6.4.

The rate of MPE hydration over $\gamma$-$Al_2O_3$ at 623 K, as defined in Equation 9, is negligible in reference to experimental variance and uncertainties at water partial pressures below 2.1 kPa (Figure 22). The calculated rates of 1-propanol dehydration at the effluent 1-propanol partial pressures were at least two orders of magnitude smaller than all other rates in Equations 9-11; therefore, the rates of 1-propanol conversion throughout the bed were neglected in this analysis. Methanol was co-fed to avoid

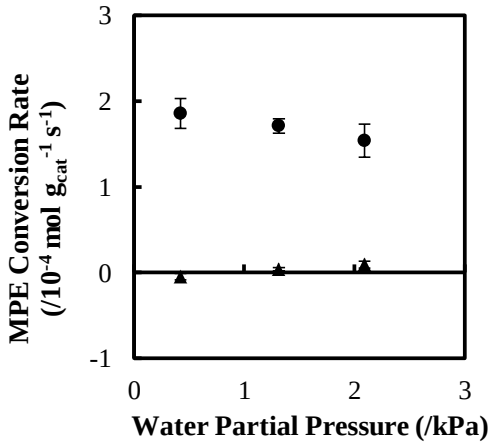


**Figure 22**. The conversion rate of 0.8 kPa of MPE through (●) disproportionation and (▲) hydration on 1.0 mg of $\gamma$-$Al_2O_3$ at 623 K as a function of co-fed water partial pressure. A co-feed of 0.2 kPa of methanol was added to avoid methanol concentration gradients across the reactor.

concentration gradients of methanol across the packed bed that could affect the observed rate of the reaction of methanol and MPE to synthesize DME and 1-propanol. The negligible ether hydration rates lead us to conclude that, at water partial pressures below 2.1 kPa, the measured rate of conversion of light ethers, such as DEE, are primarily a result of ether disproportion. The conclusion that ether disproportionation is the primary ether consumption pathway on $\gamma$-$Al_2O_3$ is consistent with the 1:1 stoichiometric production of ethanol and ethylene at low conversions from DEE conversion over $\gamma$-$Al_2O_3$ at 523-616 K observed previously by Knözinger and Köhne as well as Morávek and Kraus[16,34]. The kinetic dominance of ether disproportionation at low water partial pressures (< 2.1 kPa) allows for the evaluation of the kinetics of DEE disproportionation in absence of complications arising from multiple DEE conversion pathways.

*4.3.2 Steady state kinetic measurements of DEE disproportionation*

The rate of DEE disproportionation at 623 K possesses a DEE partial pressure order between 0 and 1, decreasing with increasing DEE partial pressure (going from 0.6 to 0.2 as DEE partial pressure is increased from 0.4 to 8.5 kPa; Figure 23a). Additionally, DEE disproportionation rates decrease by a factor of 20% when the ethanol partial pressure is increased from 0.3 to 0.5 kPa (DEE pressure = 4.3 kPa), demonstrating that ethanol-derived surface species inhibit DEE conversion at 623 K (Figure 23a). This observation is consistent with measured ethanol dehydration kinetics in which ethanol-derived surface species were observed to be a kinetically relevant species above 623 K[76]. As is the case

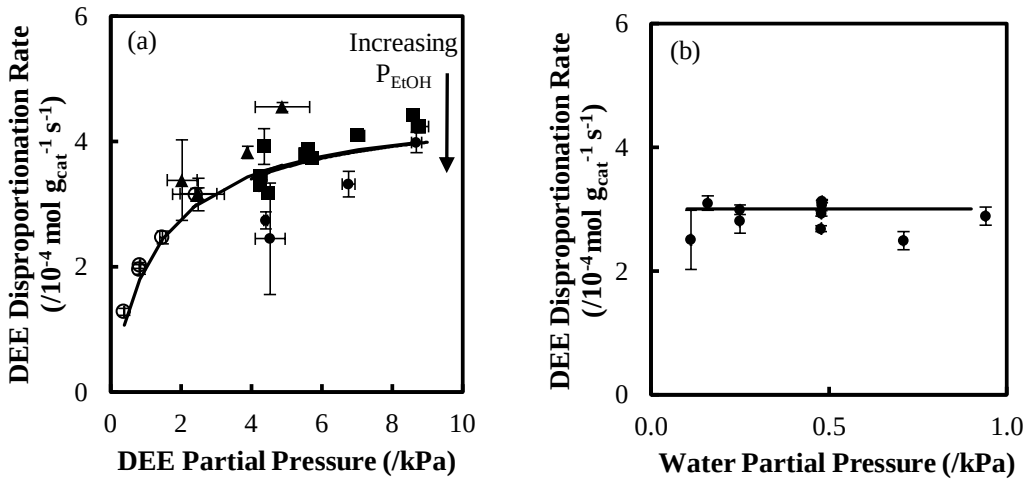


**Figure 23.** DEE disproportionation rates over 1.0 mg of $\gamma$-$Al_2O_3$ at 623 K as a function of (a) DEE partial pressure with a 0.5 kPa water co-feed and (b) co-fed water partial pressure with a feed DEE partial pressure of 2.4 kPa. In the data presented in (a) ethanol was both independently fed and in the DEE feed solution as a stabilizing agent, the average total fed ethanol partial pressure was (○) 0.1 kPa, (▲) 0.2 kPa, (■) 0.3 kPa, and (●) 0.5 kPa. The solid lines show model fits to Equation 21.

with MPE disproportionation (Figure 22) and ethanol dehydration[76] at 623 K, DEE disproportionation rates are independent of water partial pressure below 1.0 kPa of water (Figure 23b), verifying that water-derived surface species are not stable on the catalytically active sites of $\gamma$-$Al_2O_3$ at 623 K.

A mechanism for the disproportionation of DEE that is consistent with the steady state kinetic measurements shown in Figure 23 is presented in Figure 24. In this mechanism, DEE first adsorbs onto an empty catalytic site on the $\gamma$-$Al_2O_3$ surface. The DEE then dissociates to form two $C_2$ surface species, likely two surface ethoxy species, one of them comprising a lattice oxygen atom. The surface ethoxy containing the lattice oxygen then undergoes decomposition via cleavage of the $C_\beta$-H and C-O bonds to form a gas phase ethylene molecule and a surface-bound hydrogen adatom in a manner

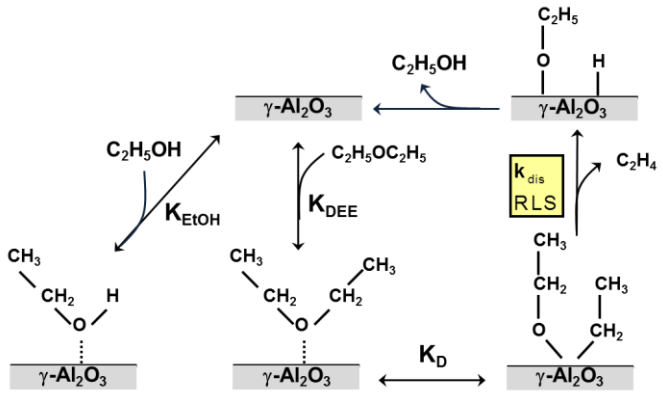


**Figure 24.** The proposed mechanism for DEE disproportionation on γ-$Al_2O_3$.

analogous to the decomposition of ethoxy species in the postulated mechanism for unimolecular ethanol dehydration reported previously[65]. The surface-bound hydrogen adatom and the remaining surface-bound ethoxy species recombine to synthesize ethanol and regenerate the catalyst surface.

The rate-limiting step of the mechanism depicted in Figure 24 is similar to that for ethylene synthesis from ethanol dehydration on γ-$Al_2O_3$ discussed in our previous report[65,76]. In these reports, a primary kinetic isotope effect (KIE) for ethylene synthesis was only observed when the C-H bonds of the ethanol were deuterated ($r_H/r_D$ = 2.4 at 488 K and $r_H/r_D$ = 1.9 at 623 K), verifying that C-H bond cleavage, likely that of a $C_\beta$-H bond, was rate-limiting for ethylene synthesis. Similarly, Knözinger and Scheglila[60] measured a primary KIE for the dehydration of *tert*-, *sec*-, and *iso*-butanol only when the $C_\beta$-H bond of the reactant was deuterated. Considering the rate-limiting step for ethylene formation is the same for both ethanol dehydration and DEE disproportionation, the rate equation for DEE disproportionation, $r_{dis}$, shown in Equation 21 can be derived assuming that chemisorbed ethanol and surface ethoxy species formed from dissociated DEE are the

prominent surface species on the active sites and are in quasi-equilibrium with gas phase ethanol and DEE.

$$r_{dis} = \frac{k_{dis} K_{DEE} K_D P_{DEE}}{1 + K_{DEE} K_D P_{DEE} + K_{EtOH} P_{EtOH}} \quad (21)$$

$k_{dis}$ is the intrinsic rate constant for DEE disproportionation. $K_{DEE}$ and $K_{EtOH}$ signify the equilibrium constants of adsorption for DEE and ethanol, respectively. $K_D$ is the equilibrium constant for dissociation of an adsorbed DEE molecule into two surface ethoxy groups, one containing an oxygen atom from the reactant molecule and another containing a lattice oxygen atom. $P_{DEE}$ and $P_{EtOH}$ respectively represent the partial pressures of DEE and ethanol. The values for the kinetic parameters $k_{dis}$ and $K_{DEE}$ of Equation 21 were estimated from the data in Figure 23 and are compiled in Table 11. The equilibrium constant for the adsorption of ethanol to form chemisorbed species that are reactive for ethylene synthesis from dehydration, $K_{EtOH}$, was evaluated previously (0.22 ± 0.17 $kPa^{-1}$)[76] and was held constant in the parameter estimation for DEE disproportionation (Equation 21). The solid line in Figure 23 shows the fit of the kinetic model presented in Equation 21. A statistical analysis of the residual errors of this kinetic model,

**Table 11.** Kinetic parameters for DEE disproportionation on γ-$Al_2O_3$ at 623 K estimated using the model presented in Equation 21 and the data presented in Figure 23.

| Parameter | $k_{dis}$ ($/10^{-4}$ mol $s^{-1}$ $g^{-1}$) | $K_{DEE}K_D$ ($kPa^{-1}$) | $K_{EtOH}$ ($kPa^{-1}$) |
|---|---|---|---|
| Value | 4.6 ± 0.5 | 0.78 ± 0.32 | 0.22 ± 0.17 |

including parity, lag, and normal probability plots, is presented in Section 6.5.

The value for the intrinsic rate constant for DEE disproportionation, $(4.6 \pm 0.5)x10^{-4}$ mol $s^{-1}$ $g^{-1}$, is approximately a factor of two lower than the previously reported value for unimolecular dehydration of ethanol on $\gamma$-$Al_2O_3$ to form ethylene at 623 K, $(9.4 \pm 3.3)x10^{-4}$ mol $s^{-1}$ $g^{-176}$. We postulate that the comparable values in the rate constants for these steps correspond to similarities in the proposed rate-limiting steps; in both reactions, the $C_\beta$-H bond of a $C_2$ surface species, postulated to be an ethoxy group, is cleaved in the rate-limiting step to form ethylene[65]. This result is supported by the previously mentioned DFT calculations of Christiansen et al.[67] in which the calculated barrier for DEE disproportionation (38 kcal $mol^{-1}$) was nearly equivalent to that of unimolecular ethanol dehydration (37 kcal $mol^{-1}$).

The form of the rate equation presented in Equation 21 is consistent with an alternative mechanism in which adsorbed DEE, rather than ethoxy groups formed by DEE dissociation, directly disproportionates in the rate-limiting step to form ethylene, a surface ethoxy group, and a surface hydrogen adatom. The direct decomposition of ethers as well as alcohols was proposed by Roy et al.[23] and Christiansen et al.[45,67] as the reaction pathway with the lowest calculated (density functional theory; PW 91) activation energies (38 and 37 kcal $mol^{-1}$ for DEE and ethanol respectively). The direct decomposition of adsorbed ethanol, rather than the decomposition of ethoxy groups, was also discussed as an alternative mechanism for unimolecular ethanol dehydration in previous reports[65,76,77], demonstrating that the concluded similarities in the rate-limiting

steps of DEE disproportionation and unimolecular ethanol dehydration are still valid with the alternative mechanism. Both potential mechanisms are kinetically equivalent; thus, the functional form of Equation 21, the kinetic parameters presented in Table 11, and the site requirement analysis discussed in Section 4.3.3 would be unaffected by the choice of the modeled mechanism.

*4.3.3 DEE disproportionation site requirements and density on γ-$Al_2O_3$*

In previous investigations, the degree of inhibition of measured steady state reaction rates by pyridine was used to probe the site requirements of ethanol dehydration and dehydrogenation on γ-$Al_2O_3$. Specifically, pyridine inhibited DEE synthesis to a lesser

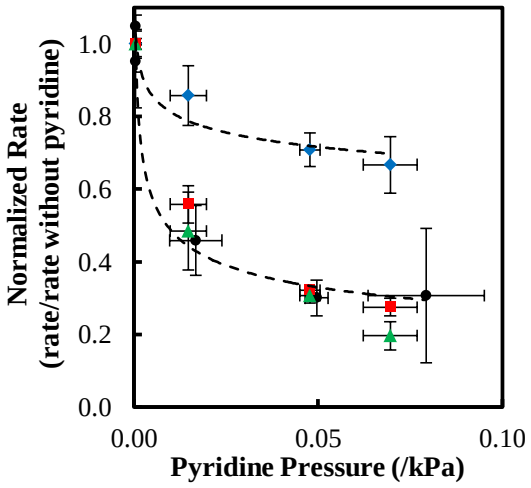


**Figure 25.** The rate of (●) DEE disproportionation from the conversion of 1.4 kPa of DEE as well as the independently evaluated (■) ethylene, (♦) DEE, and (▲) acetaldehyde synthesis rates from the conversion of 3.5 kPa of ethanol with a 1.3 kPa water co-feed on γ-$Al_2O_3$ at 623 K normalized to their rates in absence of pyridine as a function of co-fed pyridine partial pressure. The dashed lines serve as a guide for the eye.

extent than ethylene or acetaldehyde synthesis from the conversion of ethanol, demonstrating that unimolecular reactions of ethanol occur on a separate pool of catalytic sites from bimolecular ethanol dehydration[65,76].

The rate of DEE disproportionation at 623 K is inhibited by pyridine to the same extent as ethylene and acetaldehyde synthesis from ethanol dehydration and dehydrogenation and to a greater extent than DEE synthesis from bimolecular ethanol dehydration (Figure 25). This result demonstrates that DEE disproportionation occurs on catalytic sites that adsorb pyridine equivalently to those that are active for unimolecular ethanol dehydration and dehydrogenation, revealing the similar site requirements for these chemistries. Furthermore, the different extents of inhibition of DEE synthesis and disproportionation by pyridine verifies that the pool of catalytic sites responsible for bimolecular ethanol dehydration and, thus, its reverse reaction DEE hydration is not equivalent to the pool responsible for DEE disproportionation. The similar site requirements and rate constants for ethylene synthesis from ethanol dehydration and DEE disproportionation reinforces the mechanism proposed in Figure 24 in which ethylene is formed in a rate-limiting step that involves the cleavage of a $C_\beta$-H bond of a surface ethoxy species as was the case for unimolecular ethanol dehydration.

Previously, transient in-situ titrations of ethanol dehydration over $\gamma$-$Al_2O_3$ at 623 K with pyridine estimated the surface density of catalytic sites responsible for ethylene synthesis to be 0.2 sites $nm^{-2}$ [76]. The density of active sites was evaluated by analyzing the decay in available catalyst mass for DEE disproportionation after pyridine was

introduced to the reactor feed using measured reactor effluent compositions, Equation 21, and previously evaluated kinetics for ethanol dehydration[76]. To estimate the catalytic site density from this transient deactivation profile, we assume that initially (far from equilibrium) each molecule of pyridine that enters uniquely adsorbs onto one of the catalytic sites and that every catalytic site for DEE disproportionation is equivalent. We then determine the total pyridine uptake that would completely shut down DEE disproportionation by extrapolating the initial linear decay of the calculated available catalyst mass upon introduction of pyridine to the feed stream (example in Figure 26). Using this technique at different pyridine pressures and catalyst loadings, the average pyridine uptake necessary to completely shut down DEE disproportionation on $\gamma$-$Al_2O_3$ at 623 K was determined to be $(8.4 \pm 0.5)x10^{-5}$ mol $gcat^{-1}$, corresponding to 0.3 sites $nm^{-2}$

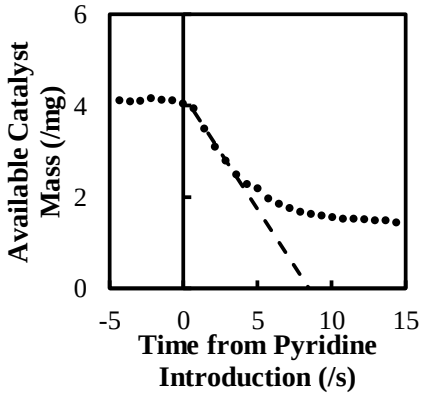


**Figure 26.** Catalyst mass available for the disproportionation of 1.5 kPa of DEE over 0.005 g of $\gamma$-$Al_2O_3$ at 623 K (total gas flowrate = 9.9 $cm^3$ $s^{-1}$) as a function of time after the introduction of 0.05 kPa of pyridine to the feed. The dashed line shows the linear extrapolation used to determine the pyridine uptake necessary to completely deactivate the rate of DEE disproportionation.

(Table 12). This estimation of site density represents an upper bound because pyridine could adsorb onto non-active sites during the titration. The comparable estimated catalytic site densities for DEE disproportionation and ethylene synthesis from ethanol dehydration (0.3 and 0.2 sites $nm^{-2}$, respectively) reinforce the conclusion that the site requirements of these two reactions are similar[76]. The nonequivalent nature of the catalytic sites that catalyze DEE disproportionation and those that are active for DEE synthesis from ethanol dehydration on $\gamma$-$Al_2O_3$ is illustrated by the 6-fold difference in estimated catalytic site densities at 623 K (0.3 and 1.8 sites $nm^{-2}$ for DEE disproportionation and synthesis, respectively)[76].

Christiansen et al.[45] calculated that energy barriers for ethylene synthesis from ethanol dehydration differ among the facets of $\gamma$-$Al_2O_3$ (37, 30, and 28 kcal $mol^{-1}$ for the (100), (110), and (111) facets, respectively) while the activation energies for DEE synthesis did not differ substantially (35, 34, and 32 kcal $mol^{-1}$ for the (100), (110), and (111) facets, respectively). The discrepancy in the calculated activation energies for

**Table 12.** Estimated pyridine surface density necessary to completely deactivate the sites for DEE disproportionation over $\gamma$-$Al_2O_3$ at 623 K determined from in-situ pyridine titrations at different catalyst loadings and pyridine partial pressures. The reported errors are 95% confidence intervals evaluated using independent titrations.

| **Pyridine Uptake ($/10^{-5}$ mol $g^{-1}$)** | **Catalyst Mass** | |
|---|---|---|
| **Pyridine Pressure** | **0.010 g** | **0.005 g** |
| **0.02 kPa** | 7.7 ± 0.5 | 9.5 ± 1.5 |
| **0.05 kPa** | 7.2 ± 0.5 | 9.0 ± 1.1 |

unimolecular and bimolecular alcohol dehydration on different facets of $\gamma$-$Al_2O_3$ is consistent with our conclusion that at least two non-equivalent pools of catalytic sites exist on the $\gamma$-$Al_2O_3$ surface. These calculations allow us to postulate the identity of the active surfaces for the two pools of the catalytic sites. We propose that unimolecular reactions of ethanol and DEE occur preferentially on higher-indexed facets of $\gamma$-$Al_2O_3$, (110) and (111), while bimolecular dehydration and ether hydration can occur on each of the three prominent facets ((100), (110), and (111)), reflected by our measured 6-fold difference in catalytic site densities for DEE synthesis from ethanol dehydration and DEE disproportionation. Electron diffraction patterns and transmission electron microscopy images of plate-like $\gamma$-$Al_2O_3$ particles synthesized by Kovarik et al.[25] demonstrate that the (110) and (111) facets dominate the external surfaces of these particles while the surfaces in the particle pores primarily comprise the (100) and (111) facets. Furthermore, the authors concluded, based on observed surface reconstructions, that the surface energies of these exposed facets increase in the following manner: (100), (111), and (110)[25]. We propose that pyridine preferentially adsorbs onto the facets with higher surface energies, (110) and (111). Therefore, the observation that ethylene and acetaldehyde synthesis from ethanol dehydration and DEE disproportionation are inhibited by pyridine to a greater extent than DEE synthesis (Figure 25) is consistent with our postulate that only these higher energy surfaces catalyze unimolecular reactions on $\gamma$-$Al_2O_3$ while bimolecular reactions can also be activated by the (100) surface. The postulate that multiple pools of catalytic sites exist on $\gamma$-$Al_2O_3$ is consistent with the microkinetic model

of ethanol dehydration developed by Christiansen et al.[45] in which DEE and ethylene synthesis could not both be described with complete accuracy using only the (111) facet. Based on our postulate, we predict that transitional alumina phases which predominantly feature the (111) and (110) facets, such as η- or θ-$Al_2O_3$[79], will produce ethylene with higher selectivity than γ-$Al_2O_3$. This prediction will be the subject of future investigations.

One complication that may alter our prediction is the stability of surface hydroxyl groups on each surface facet for each alumina. In a previous report[76], we determined that the density of catalytic sites that catalyze DEE synthesis from ethanol dehydration increased from 0.1 to 1.8 sites $nm^{-2}$ as the reaction temperature was increased from 488 to 623 K. We postulated that this increase in site density was a result of a lower density of surface hydroxyl groups at higher reaction temperatures. DFT calculations (PW91) by Digne et al.[41,42] determined that the density of surface hydroxyl groups on the (100) and (110) facets of γ-$Al_2O_3$ at 488 K was 8.8 and 11.8 OH $nm^{-2}$, respectively; At 623 K, the calculated density decreased to 0 and 8.9 OH $nm^{-2}$, respectively, supporting our explanation for the increased site density at higher temperatures.

The derived kinetics and site requirements for DEE disproportionation in this report describe one of the necessary DEE conversion pathways to model the reaction network of ethanol dehydration on γ-$Al_2O_3$ to selectively form ethylene. These DEE conversion pathways explain the negligible DEE yields from ethanol dehydration on γ-$Al_2O_3$ at very high conversions (>99%) at 623 K observed by Phung et al.[33] The reported

kinetic model for DEE disproportionation and those derived previously for ethanol dehydration[65,76,77] comprise a mechanistic picture capable of rigorously describing the conversion pathways of ethanol on $\gamma$-$Al_2O_3$.

## 4.4 Conclusions

Steady state kinetic measurements of MPE conversion on $\gamma$-$Al_2O_3$ at 623 K confirm that ether hydration rates are negligible compared to ether disproportionation rates at water partial pressures below 2.0 kPa. Measured DEE disproportionation rates possess a DEE reaction order between 0 and 1 (between 0.4 and 8.5 kPa of DEE) and are independent of co-fed water partial pressure. A mechanism in which the rate-limiting step is ethylene formation from a surface ethoxy group and surface-bound ethanol monomers and DEE-derived ethoxy groups primarily cover the catalytic sites describes the measured DEE rates. The estimated intrinsic rate constants for DEE disproportionation and ethylene synthesis from ethanol dehydration[76] on $\gamma$-$Al_2O_3$ are within a factor of two, demonstrating the similarities in the rate-limiting steps of these reactions. DEE disproportionation rates are inhibited by pyridine to the same extent as ethylene synthesis rates from ethanol dehydration on $\gamma$-$Al_2O_3$ and to a greater extent than DEE synthesis rates from bimolecular dehydration. The estimated density of catalytic sites responsible for DEE disproportionation (0.3 sites $nm^{-2}$) is comparable to that of ethylene synthesis from ethanol dehydration (0.2 sites $nm^{-2}$). These results verify that (i) unimolecular dehydration of ethanol and DEE disproportionation possess similar site requirements,

supporting the common rate-limiting steps conjectured for each reaction, and (ii) bimolecular ethanol dehydration and DEE disproportionation occur on non-equivalent catalytic sites.

**Acknowledgements**

We would like to thank The Dow Chemical Company and the University of Minnesota Doctoral Dissertation Fellowship for their financial support. We would also like to thank Mr. Marcello Herrera and Mr. Minje Kang helpful technical discussions.

# *Chapter 5: Unpublished results – Mechanistic Pathways of Byproducts of Acrylic Acid Synthesis from Acrolein Oxidation over Mixed-Metal Oxides*

## 5.1 Introduction

The worldwide annual demand of acrylic acid, a ubiquitous chemical platform used in the production of superabsorbent polymers, coatings, and many other commercial products[80,81], was 5.8 million metric tons as of 2014 and is projected to have a demand of 8.8 million metric tons by 2022 – an estimated market of $23 billion[82]. Industrially, acrylic acid is synthesized through a two-step sequential process in which propylene is first oxidized over a reducible mixed-metal oxide catalyst to form acrolein which is subsequently further oxidized in a separate reactor over a different reducible metal oxide catalyst to produce acrylic acid[83-86]. Acetaldehyde, acetic acid, CO, and $CO_2$ are all observed byproducts of acrolein oxidation[84,87-92]. The formation of undesired acids and aldehydes, beyond reducing acrylic acid yield, contributes to both reactor fouling and premature polymerization of acrylic acid in downstream processing[88]. Herein, we investigate the synthesis and consumption pathways of byproduct formation during the oxidation of acrolein over a commercial mixed-metal oxide catalyst.

Metal oxides that contain both molybdenum and vanadium form the basis of one of the most commonly-studied catalysts for acrolein oxidation both industrially[80,81,83,88,93] and in the published literature[85,89-92,94-101]. Various metal additives, including W, Mn, Fe, Sb, Cr, Sr, and Cu, have also been used to improve catalyst stability and acrylic acid

selectivity[80,81,83,87,89,98]. Andrushkevich et al.[91,94-96] investigated several Mo-V-O samples active for acrolein oxidation using both X-ray diffraction (XRD) and infrared (IR) spectroscopy and identified diffraction patterns and absorption bands attributed to the presence of $VMo_3O_{11}$, $VMo_2O_8$, and $V_6Mo_4O_{25}$ as well as separate molybdate and vanadate domains. These observations demonstrate a structural complexity to reducible oxide systems beyond that attributed to catalyst composition upon modification by additives and promoters. In these investigations, the highest acrylic acid selectivity (>90%) was measured in catalyst samples that possessed the $VMo_3O_{11}$ phase[91,94-96]; this method of investigation, however, is performed ex-situ and focuses on bulk phase composition and, thus, cannot account for any reaction-induced restructuring of the catalyst surface. Acrolein oxidation rates (4% acrolein, 10% oxygen, and 20% water feed) over a Mo-V-W-O catalyst synthesized by Ovsitser et al.[97] increased monotonically until achieving steady state after 10, 20, and 120 h at reaction temperatures of 573, 553, and 533 K, respectively. This long activation period is indicative of structural changes of the catalyst surface induced by acrolein oxidation. The authors supported this postulate with transmission electron microscope (TEM) images in which the formation of a new $(MoVW)_5O_{14}$ phase present in surface nanocrystalites was observed on the used catalyst samples[97]. Given the compositional, structural, and surface complexity of Mo-V-O catalysts, we focus our efforts on constructing a reaction network for acrolein oxidation and byproduct formation over a commercial catalyst, thereby providing a mechanistic and kinetic description of acrolein oxidation pathways over mixed-metal oxides.

Separate desorption peaks of acrolein, acrylic acid, and carbon dioxide at 347, 467, and 657 K, respectively, were observed in temperature programmed desorption (TPD) measurements (under a He sweep gas) of acrolein-doused Mo-V-O samples performed by Tichý et al.[101], demonstrating that acrolein can be oxidized in absence of gaseous oxygen by lattice oxygen or by strongly-adsorbed oxygen species. The authors concluded that the separate desorption peaks for acrylic acid and carbon dioxide are a result of two different structures of adsorbed acrolein on different sites, one that undergoes partial oxidation at 467 K and one, more strongly bound species, that only desorbs through complete oxidation at 657 K. Partial and complete oxidation over Mo-V-O in absence of gaseous oxygen is also evinced by acrylic acid and carbon dioxide production in alternating oxidation (feeding 10% oxygen in nitrogen) and reduction (feeding 5% acrolein in nitrogen) reactions at 527 K performed by Vogel et al.[100] The authors additionally heated the oxidized V-Mo-O catalyst from 373 to 773 K under the reducing 5% acrolein (balance nitrogen) flow and observed that acrylic acid was produced in a broad temperature range between 473 and 673 K while a sharp production peak for both carbon dioxide and acrylic acid was measured at 723 K[100]. These transients in acrylic acid and carbon dioxide production led the authors to also postulate that multiple pools of active oxygen sites, either lattice oxygen atoms or persistent oxygen-derived surface species, are present on the surface and are activated at different temperatures. These analyses, however, are inherently stoichiometric and therefore may not probe the relevance of any observed active oxygen pools during catalysis.

Acrolein conversion over silica-supported Mo-V oxides at 487 K was observed to be independent of feed acrolein concentration between 3 and 10% (total system pressure unspecified), but was found to increase with oxygen feed composition (3 to 13%) in steady state measurements by Machek et al.[99], leading the authors to postulate that the rate-limiting step of acrolein oxidation is the re-oxidation of the catalyst surface after acrylic acid synthesis. This postulate is consistent with the absence of any kinetic isotope effect for acrylic acid synthesis at 573 K on Mo-V-O noted by Tichý et al.[92] when feeding acrolein that was deuterated on the carbonyl hydrogen, verifying that C-H bond cleavage is not rate-limiting. Acrolein conversion at 487 K over V-Mo-O increased as the water feed composition was increased from 10 to 30%; Machek et al.[99] thus concluded that water and/or water-derived surface intermediates can also act as oxidants to promote acrylic acid synthesis. This conclusion, however, neglects the participation of any other possible surface species that could be formed by water. The intensity of the IR band at 1425 $cm^{-1}$, attributed to ammonium ions adsorbed onto the surface of ammonia-exposed Mo-V-O, was larger for catalyst samples dosed with water prior to ammonia exposure[102], verifying that (i) hydroxyl groups capable of protonating ammonia are present in these catalytic systems and (ii) water exposure increases the density of these groups.

The published investigations on acrolein oxidation presented here focus mostly on the mechanism of acrylic acid synthesis, while byproduct formation pathways are often neglected. These studies were also performed using pure acrolein feeds and, thus, do not account for any effects of the byproducts of propylene oxidation, such as acetaldehyde,

acetone, or acetic acid, present in the feed of industrial acrolein oxidation processes. Typically, steady state kinetic measurements over V-Mo-O systems were performed at single pass conversions greater than 15%, making enumeration of reaction rates difficult; the highly exothermic nature of acrylic acid synthesis ($\Delta H_{rxn}$ = -270 kJ $mol^{-1}$ at 500 K) raises additional concerns of heat transfer in packed bed reactors with high single pass conversions. To address these points, we have constructed a dual-packed bed recirculating system that produces acrolein in-situ over a propylene oxidation catalyst, thereby introducing byproducts formed during acrolein synthesis into the influent of the acrolein oxidation reactor; these byproducts may change both the structure and function of the acrolein oxidation metal oxide catalyst. Additionally, the recirculating reactor system behaves as a batch reactor for acrolein oxidation with low single pass conversions (<1%), minimizing concerns of heat and concentration gradients across the catalyst bed and allowing for the quantification of the reaction rates of all species as acrolein conversion increases to >85%.

In this work, the reaction pathways of byproduct formation during the oxidation of acrolein over a commercial catalyst provided by our collaborators at The Dow Chemical Company are probed. Kinetic measurements with propylene, oxygen, and water co-feeds elucidate that (i) propylene inhibits acrylic and acetic acid syntheses but promotes the synthesis rate of acetone, (ii) all quantifiable rates, aside from those of ethylene and butadiene syntheses, have a positive, but fractional, order dependence in oxygen partial pressure, and (iii) water has no kinetic effect beyond promoting acetone synthesis rates.

Preliminary kinetic models for acrylic acid and acetone syntheses are presented and the model parameters are fit to measured rates.

## 5.2 Materials and methods

### *5.2.1 Reactor system*

A recirculating dual-packed bed reactor system was used to investigate the kinetics of acrolein oxidation (Schematic in Figure 27). This system comprises (i) a 500 $cm^3$ stainless steel volume, (ii) a recirculation pump (Metal Bellows MB-21), (iii) an in-loop online gas chromatograph, and (iv) two packed bed reactors that could be added to the recirculation loop using 4-way valves. An Agilent 6890 N gas chromatograph (GC) outfitted with both an HP-Plot/Q column (30 m x 320 μm x 20 μm), to separate oxygenates, and a CP Molsieve 5A column (25 m x 320 μm x 30 μm), to separate permanent gases, was used to analyze the reactant and product compositions; concentrations were quantified with a thermal conductivity detector and a flame ionization detector arranged in series. The recirculation pump achieves a volumetric recirculation rate greater than 8.3 $cm^3\ s^{-1}$ when the acrolein oxidation reactor is included in the loop and a flowrate of 4.2 $cm^3\ s^{-1}$ when the larger packed bed (Section 5.2.2) of the propylene oxidation reactor is in the loop. All components of the system are kept above 358 K with either resistive heat tape or in a Quality Lab Model 40GC lab oven to prevent any undesired condensation of the reaction products. The recirculation loop pressure was

monitored by an Omegadyne 0-150 psig pressure transducer located at the outlet of the recirculation pump. Both reactors contained catalyst beds supported by quartz wool in 1/4'' OD quartz tubes. The tubes were placed in clamshell furnaces constructed in-house from cylindrical aluminum blocks each heated by two 6'' Omega stainless steel heating cartridges. Each furnace was insulated by a layer of glass wool and insulation tape. Furnace temperatures were maintained by Watlow temperature controllers connected to type K thermocouples placed on the quartz tubes directly outside of the middle of the catalyst beds. At the end of each experimental run, effluent gases were bubbled through a 1M sodium bisulfite solution to complex any remaining acrolein before being vented into a fume hood.

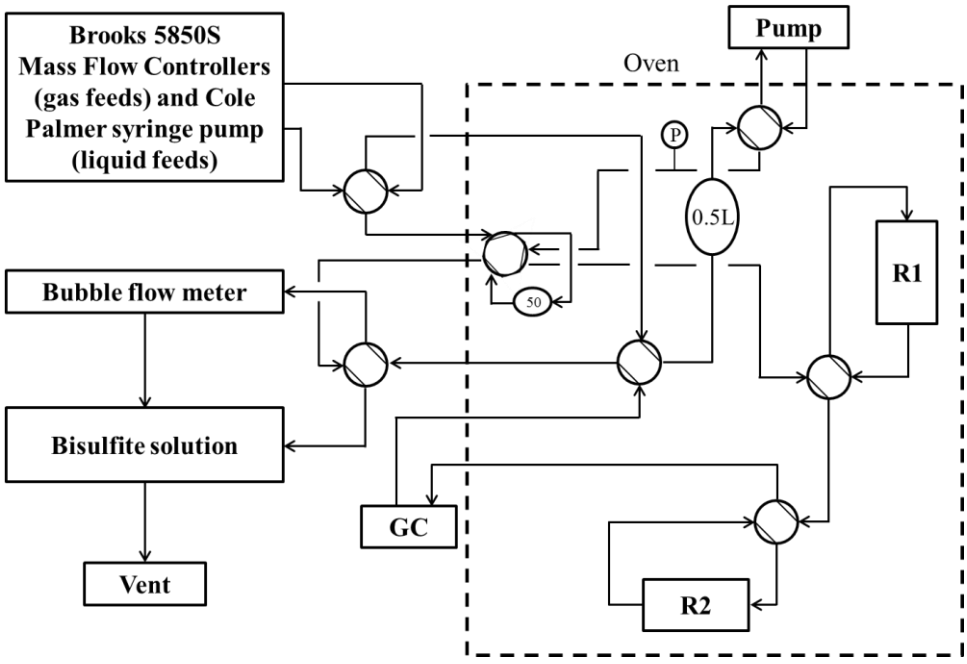


**Figure 27.** Schematic of the recirculating dual-packed bed reactor system used to investigate acrolein oxidation.

*5.2.2 Catalyst pretreatment*

Acrolein was generated in-situ from the oxidation of propylene over a commercial catalyst (referred to as R1 in this document), while the oxidation of acrolein was investigated over a different commercial mixed-metal oxide (R2 in this document). Both catalysts were provided by The Dow Chemical Company. Ovsitser et al.[97] observed that Mo-V-O samples that were thermally treated in an inert atmosphere at 813 K did not display the >90 h activation period at 543 K observed on untreated samples. Following this observation, the R2 catalyst was treated in UHP air (Zero grade, Matheson Gas) for >24 h at 583 K prior to reaction at 498 K. The R1 reactor was loaded with 0.11 g of R1 catalyst (particle sizes between 180 and 425 μm) diluted in 1.0 g of Acros Organics sand (152–422 μm particle size), while the R2 reactor was loaded with 4.5 mg of the R2 commercial catalyst (particle size: 180-425 μm) and 0.11 g of sand. After each experiment, the R1 catalyst was treated overnight in UHP air at 623 K while the R2 catalyst was treated in He (Grade 4.7, Minneapolis Oxygen Company) at 498 K.

*5.2.3 Measurement of acrolein oxidation kinetics*

Acrolein was generated in-situ from propylene oxidation over the commercial R1 catalyst to avoid the toxicity hazards associated with feeding liquid acrolein directly into the system. An initial feed composition comprising 1.9 mol% propylene (99.97%, Matheson Gas), 20 mol% UHP air, 1.4 mol% deionized water, and balance He was loaded into the recirculation loop (without either reactor initially included in the loop) using Brooks 5850S Mass Flow Controllers for the gaseous feeds and a Cole Palmer

syringe pump for the water feed. The system pressure was increased to 120 kPa using a shut-off valve at the effluent of the system before the recirculation loop was isolated and recirculation initiated by the pump. The R1 reactor was then introduced to the recirculation loop and the initial propylene-containing feed underwent oxidation for 3.2 ks at 623 K to achieve propylene conversions >85%. At this point, the R1 reactor was removed from the loop and the R2 reactor (held at 498 K) was introduced to the loop for 1.0 ks to overcome an induction period observed on untreated R2 catalyst samples (see Section 6.6) before being isolated from the loop again and purged with He. After the initial exposure of the R2 catalyst, a pulse of product or reactant co-feed (pure He for baseline kinetics) was added to the system by incorporating a 50 $cm^3$ mixing volume filled with the desired concentration of the co-fed compound into the recirculation loop using a 6-way valve (Figure 27). The composition of the recirculating gas mixture was then measured with neither reactor present in the recirculation loop and taken as the initial feed composition for the evaluation of acrolein oxidation kinetics (a standard initial composition profile is shown in Table 13). Once the composition of the initial feed was quantified using an in-line gas chromatograph, the R2 reactor was added to the system and the transient profiles of the product compositions were monitored for 8-10 h before the reactor effluent was purged out of the system. The R1 and R2 catalysts were subsequently treated in the manner described in Section 5.2.1. An initial complete reaction cycle detailed above was performed before the data mentioned in this report was collected to allow for any reaction-induced activation that may occur on either catalyst.

**Table 13.** Baseline initial R2 feed composition ranges after (i) exposing a reaction mixture (1.9 mol% propylene, 20% UHP air, balance He) to 0.11 g of R1 catalyst at 623 K for 3.2 ks, (ii) exposing the R1 effluent to 4.5 mg of R2 catalyst for 1.0 ks, and (iii) an addition of a 50 $cm^3$ He-filled volume to the system. Total pressure was 130 kPa.

| Compound | Partial Pressure (/kPa) |
|---|---|
| Propylene | 0.23-0.25 |
| Oxygen | 3.1-3.5 |
| Water | 4.3-4.6 |
| Acrolein | 2.0-2.2 |
| Acrylic acid | 0.27 (unchanged within error) |
| $CO_2$ | 0.13-0.17 |
| CO | 0.09-0.11 |
| Acetaldehyde | 0.025-0.030 |
| Acetic acid | 0.020-0.021 |
| Acetone | $(4.2\text{-}4.7)\times10^{-4}$ |
| Ethylene | $(1.0\text{-}1.1)\times10^{-3}$ |
| Benzene | $(5.6\text{-}6.0)\times10^{-4}$ |
| Butadiene | $(2.3\text{-}2.8)\times10^{-4}$ |
| Allyl Alcohol | $(4.3\text{-}4.6)\times10^{-4}$ |

*5.2.4 Evaluation of rates and kinetic parameters for acrolein oxidation*

The rate of each compound was evaluated by a second- or first-order (for compounds with constant rates within experimental error) polynomial fit to the transient composition profile of the reactor effluent during reaction. Kinetic parameters for postulated models were estimated from measured rates using Bayesian statistical optimization techniques in the Athena Visual Studio software package (v14.2, W. E. Stewart and M. Caracotsios). Reported confidence intervals for model parameters reflect 95% marginal highest posterior density intervals.

## 5.3 Results and discussion

### *5.3.1 Transient kinetic behavior of acetic acid and acetaldehyde without co-feeds*

Acrolein and acetaldehyde conversion and transient composition profiles of each of the products during oxidation of the baseline initial feed mixture (shown in Table 13) at 498 K over the R2 commercial catalyst are presented in Figures 28 and 29. Deviations in the initial amounts of different hydrocarbons in Figure 29 are a result of variations in R1 catalyst performance among three baseline replicate experiments prior to reaction over the R2 catalyst. Allyl alcohol is completely consumed within 7.2 ks of reaction and will not be discussed in this work, as its consumption rate is not quantifiable using our current analytical procedure. A carbon balance of 100 ± 3 % was maintained over all measurements. Acrylic acid is the predominant product of acrolein oxidation with a carbon selectivity >98% up to acrolein conversions >85%. While the transient behaviors of other compounds during the baseline experiment will not be discussed in this subsection, they have been included in Figure 29 for completeness.

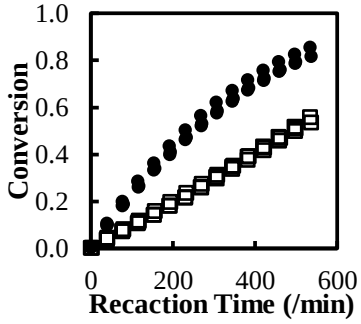


**Figure 28.** Acrolein (●) and acetaldehyde (□) conversion as a function of reaction time for three baseline replicate experiments over 4.5 mg of commercial R2 catalyst at 498 K. Initial feed compositional ranges are listed in Table 13 (inerts: 20 kPa of nitrogen, balance He). Total system partial pressure = 130 kPa.

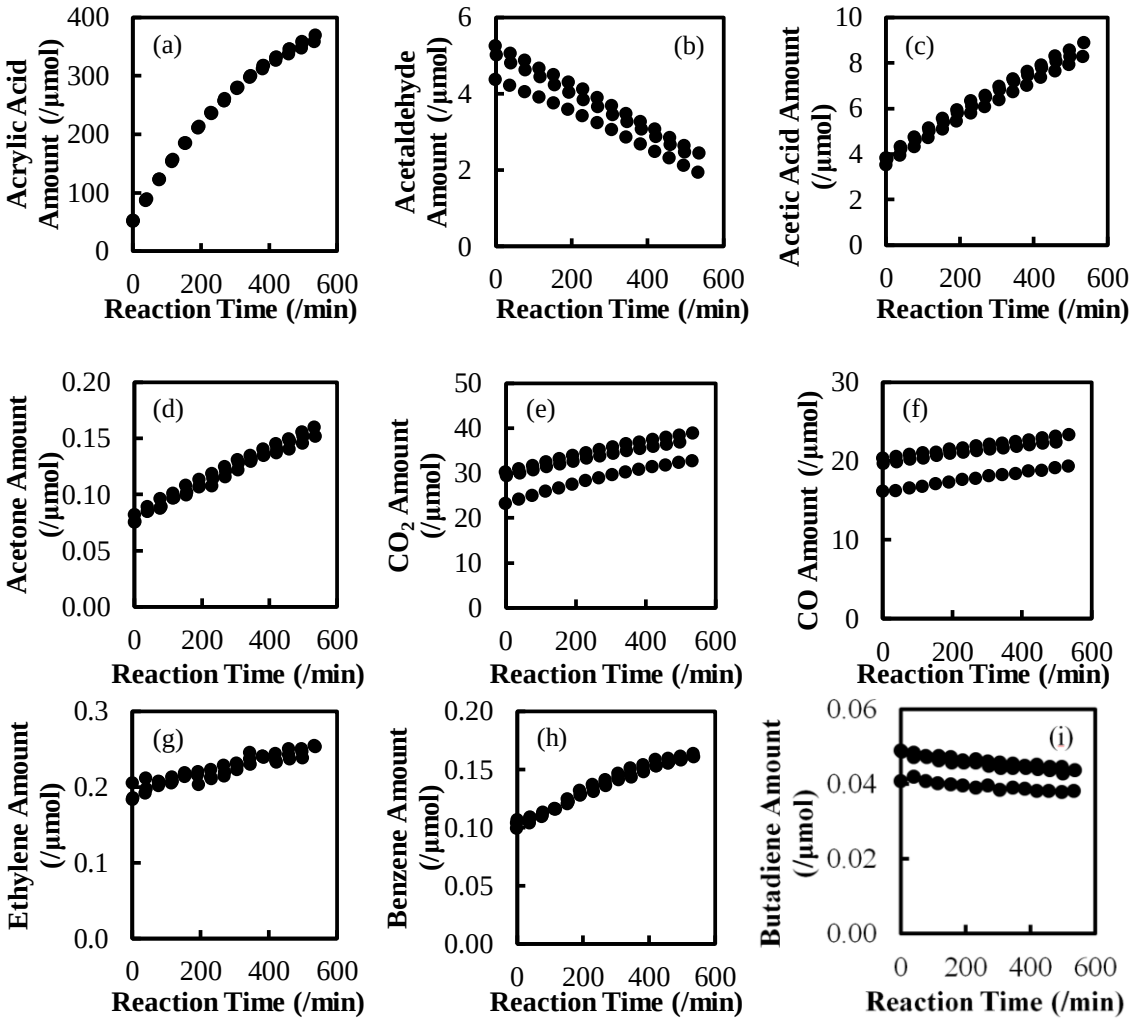


**Figure 29.** (a) Acrylic acid, (b) acetaldehyde, (c) acetic acid, (d) acetone, (e) $CO_2$, (f) CO, (g) ethylene, (h) benzene, and (i) butadiene amounts as a function of reaction time over 4.5 mg of the commercial R2 catalyst for three baseline replicate experiments at 498 K. Initial feed compositional ranges are listed in Table 13 (inerts: 20 kPa of nitrogen, balance He). Total system partial pressure was 130 kPa.

Acetic acid synthesis rates monotonically decrease from 2.4 to 1.6 μmol $min^{-1}$ $g_{cat}^{-1}$ as acrolein conversion approaches 80% (Figure 30a). Conversely, acetaldehyde is consumed at an increasing net rate over the same timeframe (Figure 30b), despite the ~50% conversion of acetaldehyde at the end of the experiment (Figure 28). The replicate with lower initial rates for both compounds had a lower acetaldehyde R2 feed pressure from the R1 effluent (0.025 kPa compared to 0.029 and 0.030 kPa). The larger values of acetic acid synthesis rates compared to net acetaldehyde consumption rates and the observation that acetic acid rates decrease with increasing acrolein conversion while acetaldehyde consumption rates increase imply that acetic acid is synthesized through an additional pathway besides acetaldehyde oxidation. The apparent increase in the net consumption rate of acetaldehyde as the reaction proceeds (and as acetaldehyde partial pressure drops, Figure 28) could be a result of a simultaneous decrease in the rate of acetaldehyde production (from the dissociation of acrolein, for example) and of

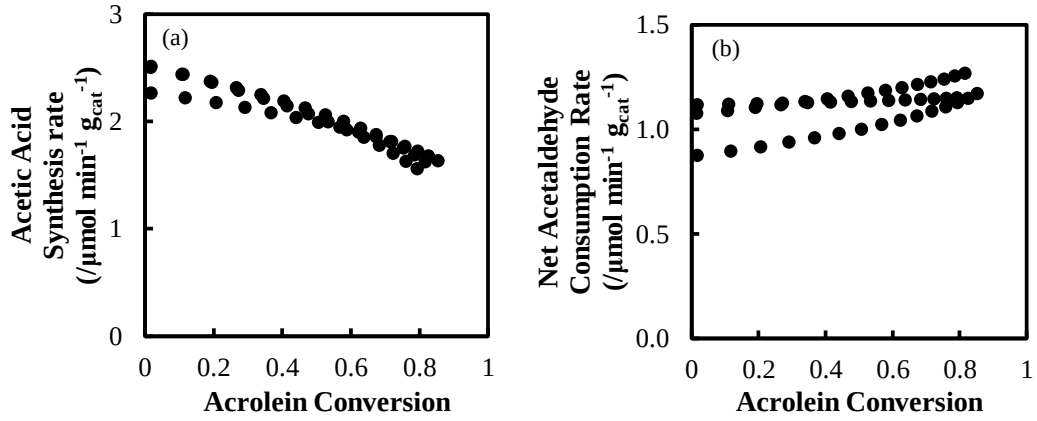


**Figure 30.** (a) Acetic acid synthesis and (b) acetaldehyde consumption rate as a function of acrolein conversion over 4.5 mg of commercial R2 catalyst at 498 K and 130 kPa total pressure. Three baseline replicates are presented with initial feed compositional ranges are listed in Table 13 (inerts: 20 kPa of nitrogen, balance He).

acetaldehyde oxidation. Specifically, acrolein is consumed more quickly than acetaldehyde as the reaction proceeds (Figure 28); thus, the net consumption rate of acetaldehyde would increase if acetaldehyde consumption and synthesis rates are proportional to acetaldehyde and acrolein partial pressures, respectively. This hypothesis will be addressed by co-feeding different partial pressures of acetaldehyde into the initial feed.

*5.3.2 Effects of propylene and water pressure on rate and selectivity of acrolein oxidation*

**Acrylic and acetic acid propylene pressure dependencies**

The initial synthesis rate of acrylic acid decreases from 213 to 176 to 173 μmol $min^{-1}$ $g_{cat}^{-1}$ as the initial propylene partial pressure increases from 0.24 to 1.1 to 1.9 kPa, respectively (Figure 31), demonstrating a slight (~ -0.1 order) inhibition by propylene on acrylic acid synthesis rates. Acetic acid synthesis displays a similar propylene partial

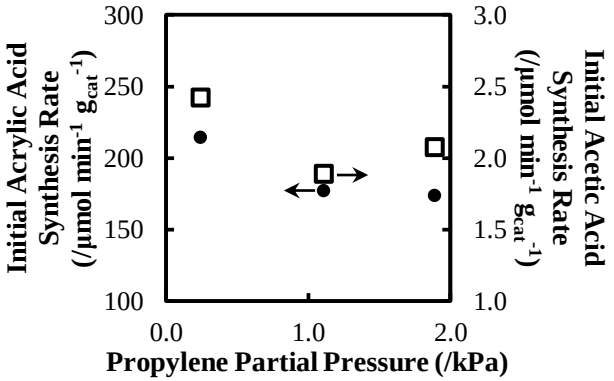


**Figure 31.** Initial acrylic (●) and acetic (□) acid synthesis rates at 498 K and 130 kPa total system pressure over 4.5 mg of R2 commercial catalyst as a function of co-fed propylene partial pressure. All other feed compounds were maintained in the composition ranges listed in Table 13 (inerts: 20 kPa of nitrogen, balance He).

dependence with initial rates of 2.4, 1.9, and 2.1 μmol $min^{-1}$ $g_{cat}^{-1}$ at 0.24, 1.1, and 1.9 kPa of propylene, respectively (Figure 31). This inhibition cannot be simply explained with a Langmuir-Hinshelwood-type coverage of the oxidation sites by propylene, leading us to postulate that propylene somehow changes the surface distribution of oxidation sites. The propylene partial pressure in industrial applications, however, would be expected to be much lower (larger propylene conversions in R1); thus, the observed inhibition by propylene may not be important in commercial acrylic acid production conditions.

**Effects of propylene partial pressure on butadiene net rates**

The average net synthesis rates of butadiene increase (evaluated using first order fits to composition profiles) from -1.8 (net consumption) to 0.42 to 2.0 (net production) nmol $min^{-1}$ $g_{cat}^{-1}$ as the propylene pressure is changed from 0.24 to 1.1 kPa to 1.9 kPa (Figure 32a). The positive propylene reaction order of the net butadiene synthesis rate verifies that butadiene is synthesized from a propylene-derived reaction intermediate; we postulate that this intermediate is a $C_6$ species formed from the dimerization of propylene that rapidly decomposes to synthesize butadiene. We will co-feed $C_6$ olefins, such as hexadiene, in the future to probe $C_6$ decomposition pathways over the commercial R2 catalyst.

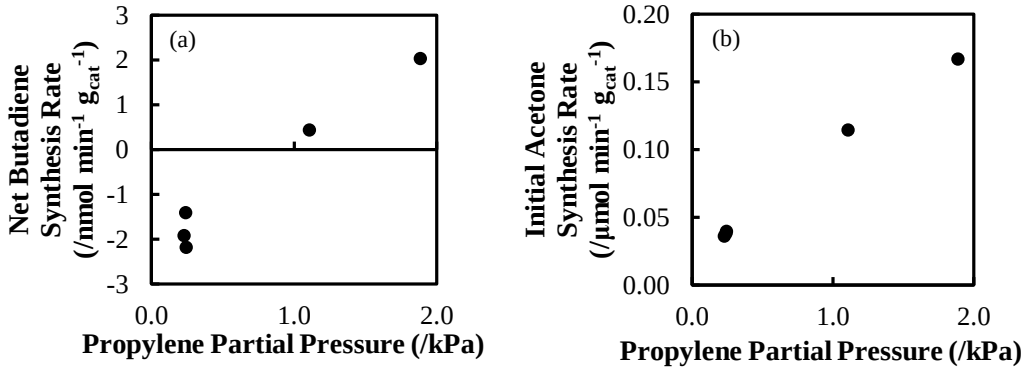


**Figure 32.** (a) Net butadiene and (b) initial acetone synthesis rates at 498 K over 4.5 mg of R2 commercial catalyst as a function of co-fed propylene partial pressure. Total system pressure = 130 kPa. All other feed compounds were maintained in the composition ranges listed in Table 13 (inerts: 20 kPa of nitrogen, balance He).

**Effects of propylene and water co-feeds on acetone synthesis rates**

Initial net acetone synthesis rates display an approximate first order dependence (0.7) on propylene partial pressure below 2.0 kPa of co-fed propylene (Figure 32b), demonstrating that acetone is a product of propylene oxidation. Acetone was the predominant (>50% selectivity) product of propylene oxidation at 10% propylene conversion in steady state kinetic investigations conducted by Erenburg et al.[102] over a Mo-V-O catalyst at 553 K, reinforcing our conclusion that acetone is derived from propylene oxidation over the commercial catalyst. Acetone synthesis rates increase from 0.038 to 0.046 μmol

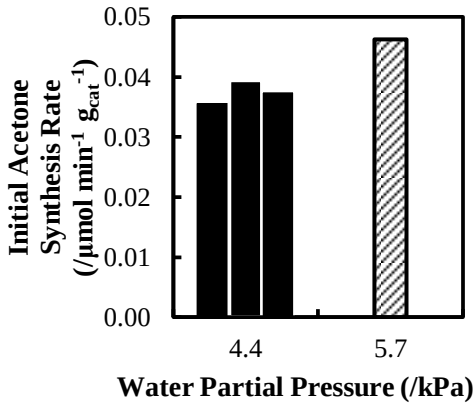


**Figure 33.** Initial acetone synthesis rates at 498 K over 4.5 mg of R2 catalyst for three kinetic measurements at 4.4 kPa of water and one with a 5.7 kPa of water co-feed. Total pressure = 130 kPa. All other feed compounds were within the composition ranges listed in Table 13 (inerts: 20 kPa of nitrogen, balance He).

$min^{-1}$ $g_{cat}^{-1}$ as the water partial pressure is increased from 4.4 to 5.7 kPa (Figure 33). A near first order water pressure dependence of acetone production rates from propylene oxidation over Mo-V-O at 573 K between 9 and 18 kPa of water was measured by Erenburg et al.[102] Furthermore, as briefly mentioned in Section 5.1, the authors also observed that exposing catalyst samples to water prior to IR spectroscopy measurements of ammonia-dosed Mo-V-O samples resulted in an increased peak intensity at 1425 $cm^{-1}$, which the authors attributed to the formation of ammonium ions on Brønsted acid sites[102]. These observations led the authors to conclude that surface hydroxyl groups are active in the synthesis of acetone from propylene oxidation on Mo-V-O. We extend this conclusion to the commercial R2 catalyst system to describe the simultaneous positive order dependencies of acetone synthesis rates on both propylene and water partial pressures.

### *5.3.3 Kinetic dependencies of hydrocarbon synthesis rates in acrolein oxidation on oxygen partial pressure*

The initial rates of all quantified products, with the exceptions of ethylene and butadiene, increase with increasing oxygen partial pressure between 3 and 11 kPa (Figure 34). The oxygen partial pressure dependencies of the initial rates of these compounds, however, decrease with increasing oxygen partial pressure (Figure 34). The observed disparity in the acetone rates at 5.8 kPa of oxygen can be accounted for by different propylene partial pressures in the initial feed to R2 (0.22 and 0.29 kPa); the ratios of the

initial rates and the propylene partial pressures thus collapse to the same value (0.22 μmol $min^{-1}$ $g_{cat}^{-1}$ $kPa^{-1}$).

Apparent reaction orders in oxygen ($n_{app}$), as evaluated from a regression of a simple power law model, for each compound are recorded in Figure 34; all compounds show similar fractional order dependencies (~0.5). The similarities in oxygen orders for

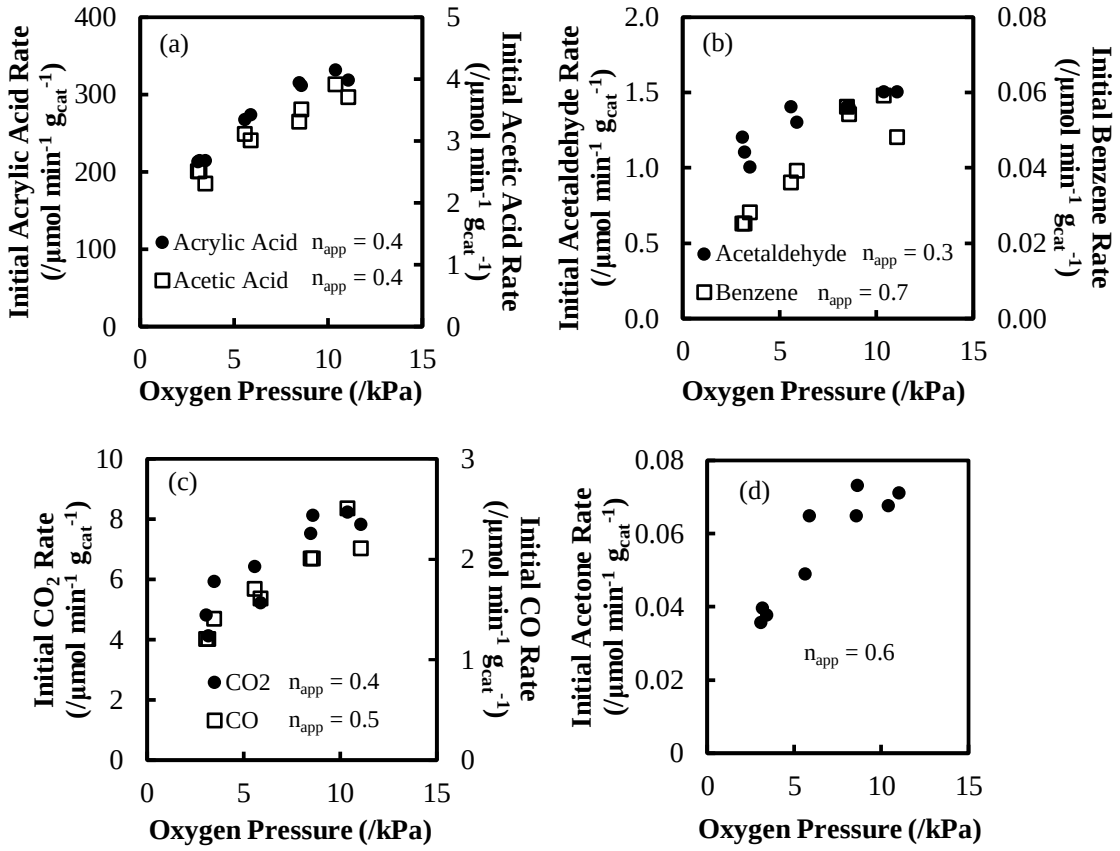


**Figure 34.** Initial synthesis (and consumption for acetaldehyde) rates of (a) acrylic acid and acetic acid, (b) acetaldehyde and benzene, (c) $CO_2$ and CO, and (d) acetone during acrolein oxidation over 4.5 mg of R2 catalyst at 498 K as a function of initial oxygen pressure. Table 13 shows the composition ranges of all other compounds (inerts: 20 kPa nitrogen, balance He). Total pressure = 130 kPa. The apparent reaction orders in oxygen ($n_{app}$) are included within each plot.

all compounds, despite the expectation that synthesis mechanisms would differ among compounds containing different functionalities, signify that oxygen plays a role in changing the distribution of sites on the catalyst surface. Kolosov et al.[103] employed electron paramagnetic resonance (EPR) on silica-supported molybdenum oxide samples that have been exposed to $N_2O$ at 373 K and measured signals with g-factors of 2.021 and 2.006 which were assigned to the formation of adsorbed $O^-$ anionic species on the oxide surface. Furthermore, the authors observed that samples exposed to oxygen at room temperature produced signals with g-factors of 2.017, 2.010, and 2.004 ascribed to adsorbed electrophilic $O_2^-$ species[103]. These results demonstrate that a distribution of potentially active oxygen species comprising adsorbed electrophilic $O^-$ and $O_2^-$ species as well active lattice oxygen species (discussed in Section 5.1) may be present on reducible metal oxides. We postulate that changing the oxygen partial pressure alters the relative distribution of these oxygen species and of reduced catalyst vacancies, thereby affecting the synthesis rates of the majority of quantified compounds in a similar manner (~0.5 order).

### *5.3.4 Preliminary kinetic models for acrylic acid and acetone synthesis*

**Acrylic acid synthesis model**

We have demonstrated that (i) propylene acts to inhibit the rate of acrylic acid synthesis (Section 5.3.2), (ii) oxygen plays a critical role in dictating the rates of most observed products, presumably by altering the distribution of active oxygen species on

the surface (Section 5.3.3), and (iii) water promotes the synthesis of acetone but does not affect the synthesis rate of any other compound (Section 5.3.2). Equations 22-25 show reaction steps that describe: (i) the synthesis of acrylic acid (AA) from the oxidation of acrolein (Acr) by a lattice oxygen ($O_L$), (ii) reoxidation by gaseous oxygen of the catalyst vacancy (V) produced by lattice oxygen removal, (iii) the reversible formation of surface hydroxyl groups (OH) from the dissociation of water on lattice oxygen sites, and (iv) the reversible adsorption of propylene onto open lattice oxygen sites to form an inhibitory propylene adsorbate ($O_L$–$C_3H_6$).

$$O_L + Acr \xrightarrow{k_1} V + AA \tag{22}$$

$$V + O_2 \xrightarrow{k_2} O_L + \tfrac{1}{2}O_2 \tag{23}$$

$$O_L + H_2O \xleftrightarrow{K_{H_2O}} OH + Inactive\ hydroxyl \tag{24}$$

$$O_L + C_3H_6 \xleftrightarrow{K_{C_3H_6}} O_L\text{–}C_3H_6 \tag{25}$$

The choice to model lattice oxygen atoms as the oxidant for acrylic acid synthesis is motivated by the stoichiometric production of acrylic acid in absence of gaseous oxygen observed in TPD measurements on acrolein-doused Mo-O-V by Tichý et al.[101] and alternating reduction and oxidation cycles performed by Vogel et al.[100] (see Section 5.1).

Assuming that the total number of catalytic sites is constant ($O_L + V + OH = L_{total}$), the surface concentrations of active lattice oxygen sites ($[O_L]$) and active hydroxyl groups ([OH]) can be determined from Equations 22-25 and expressed as:

$$[O_L] = \frac{L_{total}}{1 + \frac{k_1}{k_2}\frac{P_{Acr}}{P_{O_2}} + K_{H_2O}P_{H_2O} + K_{C_3H_6}P_{C_3H_6}} \quad (26)$$

$$[OH] = K_{H_2O}P_{H_2O}[O_L] \quad (27)$$

Where $P_{Acr}$, $P_{O_2}$, $P_{H_2O}$, and $P_{C_3H_6}$ denote the gas phase partial pressures of acrolein, oxygen, water, and propylene, respectively.

The kinetic expression for the rate of acrylic acid synthesis ($r_{acrylic}$) shown in Equation 28 can be derived assuming that (i) acrolein is oxidized with surface lattice oxygen (Equation 22), (ii) the surface coverage of hydroxyl groups is much lower than that of open lattice oxygen sites, and (iii) the coverage of propylene-derived surface species is significant. Assumptions (ii) and (iii) are supported by the lack of any observed effect of water partial pressure on acrylic acid synthesis and by the measured inhibition of acrylic acid synthesis rates by propylene, respectively (Section 5.3.2).

$$r_{acrylic} = \frac{k_{app}P_{Acr}}{1 + \frac{k_1}{k_2}\frac{P_{Acr}}{P_{O_2}} + K_{C_3H_6}P_{C_3H_6}} \quad (28)$$

The apparent rate constant for acrylic acid synthesis is represented by $k_{app}$.

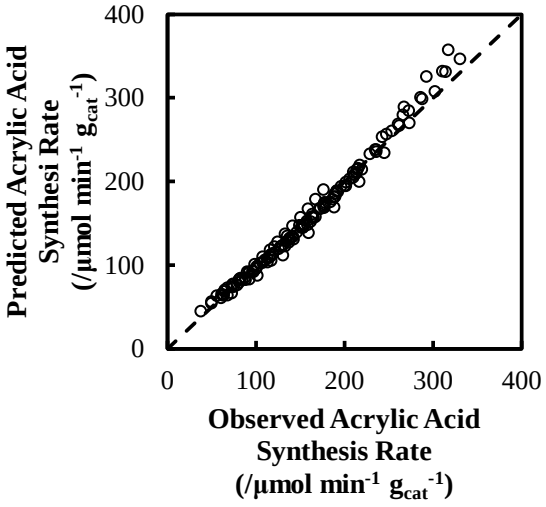


**Figure 35.** Parity plot for the model of the rate of acrylic acid synthesis from acrolein oxidation at 498 K over 4.5 mg of R2 commercial catalyst presented in Equation 28. The dashed line denotes perfect model prediction.

**Table 14.** Estimated parameter values and 95% confidence intervals for the acrylic acid synthesis model presented in Equation 28.

| Parameter | $k_{app}$ (/μmol min$^{-1}$ g$_{cat}^{-1}$) | $\frac{k_1}{k_2}$ | $K_{C_3H_6}$ (/kPa$^{-1}$) |
|---|---|---|---|
| **Value** | 263 ± 8 | 2.4 ± 0.2 | 0.41 ± 0.07 |

The kinetic parameters in Equation 28 were fit to 142 measurements over 12 experiments with different initial oxygen, propylene, and water partial pressures. The estimated values and 95% confidence intervals for each parameter are catalogued in Table 14, and Figure 35 shows the parity plot for the fit. The high carbon selectivity (>98%) of acrylic acid allows us to approximate that the rate of acrylic acid synthesis from acrolein oxidation is within error of the measured net rate of acrylic acid synthesis. In other words, the rate of acrylic acid consumption is much smaller than its rate of generation and is, thus, not quantitatively important in dictating acrylic acid composition profiles and can be neglected in the mathematical model. The rate of acrylic acid consumption could be important, however, to the net synthesis rates of other compounds.

An alternative, but mathematically similar, kinetic model (Equation 29) can be

proposed in which propylene acts as an additional reducing agent of a lattice oxygen site (with a rate constant denoted by $k_3$) rather than an inactive adsorbate on the lattice oxygen site.

$$r_{acrylic} = \frac{k_{app} P_{Acr}}{1 + \frac{k_1}{k_2}\frac{P_{Acr}}{P_{O_2}} + \frac{k_3}{k_2}\frac{P_{C_3H_6}}{P_{O_2}}} \quad (29)$$

This model, however, provides a slightly poorer fit to the experimental data (30% larger sum of squared errors). Neither model can describe the propylene inhibition behavior discussed in Section 5.3.2 in which acrylic acid rates decreased as the initial propylene pressure was increased from 0.24 to 1.1 kPa but not when it was further increased to 1.9 kPa, necessitating further model refinement with additional measurements employing oxygenate co-feeds.

**Preliminary kinetic model for acetone synthesis rates**

We have observed the net acetone synthesis rate is (i) nearly first order in propylene partial pressure (Section 5.3.2), (ii) positive order in water partial pressure (Section 5.3.2), and (iii) promoted by oxygen to a fractional order (Section 5.3.3). Taking this into consideration, a rate expression (shown in Equation 30) for the synthesis rate of acetone from propylene ($r_{acetone}$) can be dervied from Equations 26 and 27 by assuming that (i) surface hydroxyl groups are the active sites for acetone synthesis and, as was the case for acrylic acid synthesis, (ii) hydroxyl group coverage is sparse relative to open lattice oxygen sites, and (iii) adsorbed propylene species block lattice oxygen sites.

$$r_{acetone} = \frac{k_{acetone} P_{C_3H_6} P_{H_2O}}{1 + \frac{k_1}{k_2}\frac{P_{Acr}}{P_{O_2}} + K_{C_3H_6} P_{C_3H_6}} \quad (30)$$

The apparent rate constant for propylene oxidation to acetone is indicated by $k_{acetone}$. To test the robustness of the postulated surface model for acrylic acid synthesis, the initial net synthesis rates of acetone (spanning 12 experiments) were used to fit the apparent rate constant for propylene oxidation ($k_{acetone}$) while holding $\frac{k_1}{k_2}$ and $K_{C_3H_6}$ at the values reported in Table 14. The estimated value of the rate constant is 0.079 ± 0.008 μmol $min^{-1}$ $g_{cat}^{-1}$ and the parity plot for the fit is presented in Figure 36. Despite being a single parameter fit, the model describes the data except at the highest propylene partial pressure (and, thus, highest acetone synthesis rate), supporting the utility of the surface model developed for acrylic acid synthesis.

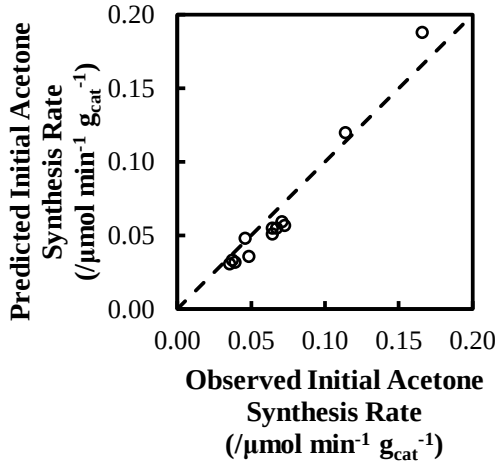


**Figure 36.** Parity plot of the model presented in Equation 30 for the initial synthesis rate of acetone over 4.5 mg of R2 catalyst at 498 K using the values for the parameters in Table 14. The dashed line denotes perfect model prediction.

Only initial rates were used to fit Equation 30 in an effort to minimize the contribution of acetone consumption to the measured net acetone synthesis rates; modeling the change in acetone consumption rates as the reaction proceeds is inapposite without additional

information provided by measurements using acetone as a co-feed. The partial pressures of other components, such as oxygen, could also affect the rate of any acetone consumption pathways at the initial conditions and may also be an additional source of error for any deviations from parity seen in Figure 36.

The models presented in this section are preliminary in nature and can be further improved upon with a larger set of initial conditions using different oxygenate co-feeds. The utility of the approach, however, remains the same as was described for ethanol conversion in Chapters 2-4. Namely, that the initial development of a kinetic model provides a powerful tool to employ (in conjunction with titrations or isotope tracers) to understand the behavior of the active surface of a catalyst under reaction conditions, unlike more traditional ex-situ characterization methods.

### 5.4 Conclusions and future work

Acrolein oxidation at 498 K over a commercial catalyst provided by The Dow Chemical Company was investigated using a dual-packed bed recirculating reactor system. The synthesis rate of acetic acid was larger than the consumption rate of acetaldehyde; additionally, acetic acid synthesis rates decreased as acetaldehyde consumption rates increased with increasing acrolein conversion, verifying that acetic acid is formed from at least one pathway in addition to acetaldehyde oxidation. Acrylic and acetic acid synthesis rates were inhibited as the initial propylene partial pressure was increased from 0.24 to 1.1 kPa, but remained unchanged as the partial pressure was

further increased to 1.9 kPa, revealing that propylene may act to alter the distribution of active sites for acrylic and acetic acid synthesis. The initial net synthesis rates of acetone were measured to be approximately first order in the partial pressures of both propylene and water, consistent with the postulate that acetone is synthesized from the oxidation of propylene over surface hydroxyl groups generated from water dissociation on the catalyst surface. A positive order dependence in propylene pressure was observed for butadiene synthesis, demonstrating that butadiene is synthesized from a propylene-derived reaction intermediate. The addition of oxygen to the initial reaction mixture increased the synthesis (and consumption for acetaldehyde) rates of all compounds excluding ethylene and butadiene. Furthermore, all of the affected species displayed a fractional order dependence in oxygen, leading us to hypothesize that a common suite of catalytic sites, some being redox centers, is used in the reaction network and the relative distribution of the sites is dictated by the gas phase pressure of oxygen. A postulated redox kinetic model with an additional term allowing for propylene adsorption onto the catalyst active sites was capable of describing the observed acrylic acid synthesis rates. Moreover, the kinetic parameters from this model could also be used to describe the initial net synthesis rates of acetone, demonstrating its robustness.

In the immediate future, oxygenate species, particularly acetaldehyde, acetic acid, acetone, and acrylic acid, will be co-fed in an effort to identify the connectivity and measure the rate dependencies of each individual step of the oxidation reaction network at 498 K. The network will then be further developed by tracking the isotopologue

distributions of each species upon introducing $^{13}C$-labeled reactants. Once a reaction network is constructed, titrants and $^{18}O$-labeled probes (oxygen and water) can be employed to determine the identities and densities of the active sites for the acrolein oxidation network.

**Acknowledgements**

I would like to thank our collaborators at The Dow Chemical Company for funding this project, providing the catalysts used in this work, and for the many helpful technical discussions. I would also like to acknowledge Linh Bui for his assistance with the construction and troubleshooting of the reactor system as well as his help with the analysis of the gathered data. Finally, I would like to extend my thanks to Jake Miller for both his support in gathering the data presented here and for his continuation of this project.

## *Chapter 6: Appendix – Statistical Analysis of Presented Model Residuals and Approach to Evaluating Kinetics during Catalyst Transients*

### 6.1 Analysis of residual error in kinetic models for ethanol dehydration at 498 K

The residual error for the proposed kinetic model for ethylene synthesis presented in Equation 3 is normally distributed as shown by the normal probability plot presented in Figure 9. Slight deviations in the distribution of the residual error for the proposed model presented in Equation 5 for DEE synthesis from a normal distribution are observed at the largest residual values associated with data at high ethanol pressures (4.2 kPa, deviations seen in Figures 6b and 7d) (Figure 37b).

A positive correlation is observed in the residual lag plots for both ethylene and

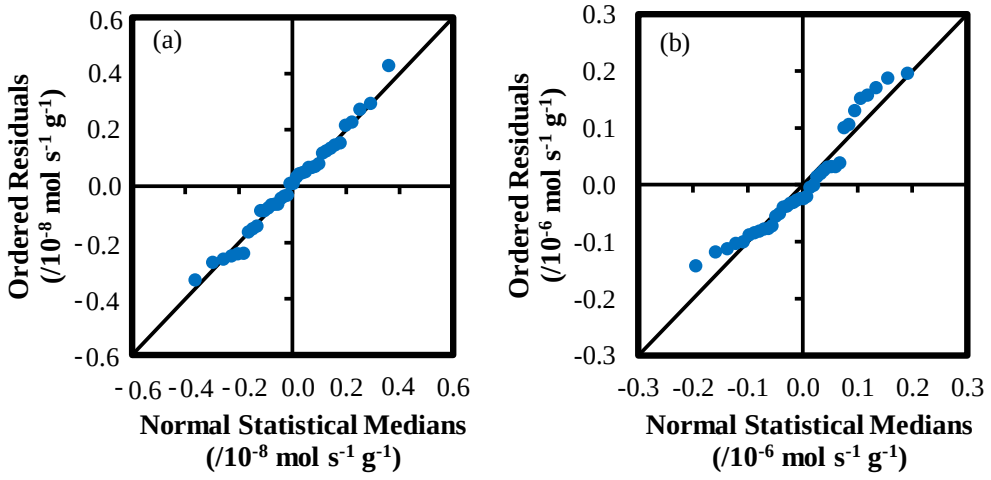


**Figure 37.** Normal probability plots for the residual error in predicted site time yields from the kinetic models presented in (a) Equation 3 for ethylene sythesis and (b) Equation 5 for DEE synthesis based upon the data presented in Figures 6 and 7. The solid line represents a perfect normal distribution in the model residuals.

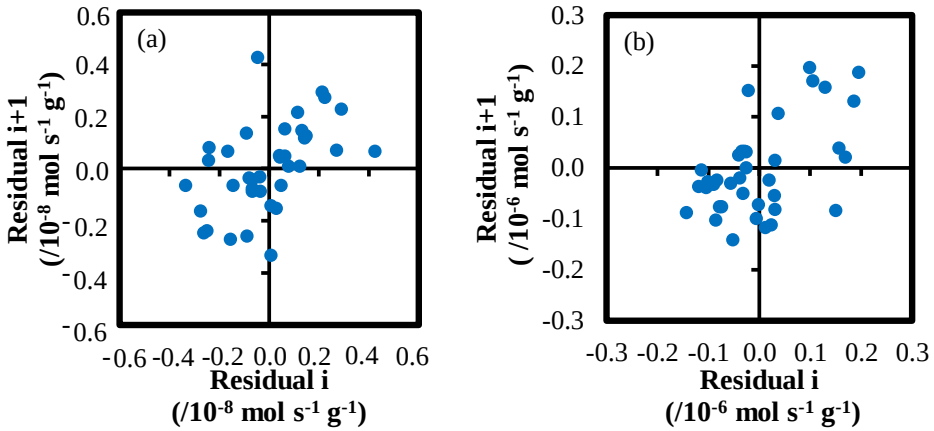


**Figure 38.** Lag plots for the residual error in predicted site time yields from the kinetic models presented in (a) Equation 3 for ethylene sythesis and (b) Equation 5 for DEE synthesis based upon the data presented in Figures 6 and 7. The residuals are ordered such that the data points of a single water pressure data presented in Figure 6 or a single ethanol pressure presented in Figure 7 are grouped together.

DEE synthesis (Figure 38). In these plots, the residuals are ordered such that all of the data for given water pressure for the data given in Figure 6 or a given water pressure for the data given in Figure 7 are together. Thus, the observed correlation in the lag plots and the observed mostly normal distribution of the errors overall is merely an indication that the residual errors of the model are consistently positive or negative for most of the constant water and constant ethanol partial pressure data sets, but across the entire data set the errors are balanced and normally distributed as can be seen in Figures 6 and 7.

These observations are indicative that either experimental bias exists between data sets or the model neglects a particular aspect of the system. The six independent measurements for site time yields at the same ethanol and water pressures presented in Figure 6 and 7 are within the 95% confidence intervals for the instrumental error determined from successive measurements at the same experimental conditions, indicating that experimental bias is unlikely to contribute significantly to the observed

error in the model. One possible source of error in the model may stem from the assumption that all of the active sites for ethylene or DEE synthesis are equivalent while it is possible that at reaction conditions there exists a group of active sites with a distribution of acid strengths as suggested by the infrared spectroscopy measurements by Parry[43] and Morterra and Magnacca[3] and the density functional theory calculations (Perdew–Wang 91 generalized gradient-corrected exchange–correlation functional) performed by Digne et al.[42] and by Wischert et al.[4]. By approximating a distribution of sites as a single type of site with a mean acid strength, the equilibrium constants for adsorption on each site is approximated with a single value, potentially causing discrepancies between the model and the observed synthesis rates at the extreme values in measured water or ethanol partial pressures. Further investigation on the distribution of active sites present under reaction condition is needed, however, to verify the extent of the error caused by this approximation.

A similar model to the one presented in Equation 3 in which water monomers were assumed to be a dominant surface species instead of water dimers was also fit to the experimental data presented in Figures 6 and 7. The resulting variance ratio, defined as the ratio of the mean square error due model fit and the mean square error due to experimental variance (determined from replicate measurements), for the water monomer model (1.70) was found to be larger than the model presented in Equation 3 (1.07). The superior statistical fit for the model presented in Equation 3 indicates that water dimer inhibition provides a more accurate description of the measured kinetics than inhibition

by water monomers. The variance ratio of a kinetic model excluding ethanol dimer inhibition also possessed a higher variance ratio than the model presented in Equation 3 (1.42), demonstrating the kinetic relevance of inhibition by these species at high ethanol pressures.

An additional term associated with inhibition by water dimers could be proposed to describe the observed -1.3 order inhibition by water on the rate of DEE synthesis at the lowest tested ethanol pressure (0.9 kPa) at 488 K. The estimated 95 % confidence interval of the kinetic parameter associated with this term was, however, larger than the value of the estimated parameter (0.25 and 2.00, respectively). This inaccuracy stems from the lack of measurements at experimental conditions at which water dimers play an important kinetic role. For this reason, water dimers were not considered to be an important species in the analyzed regime of ethanol and water partial pressures (1.9 - 7.0 kPa and 0.4 - 2.2 kPa, respectively) at 488 K and were excluded from the proposed kinetic model.

### 6.2 Deactivation of ethanol dehydration and dehydrogenation on $\gamma$-$Al_2O_3$ at 648 K

Ethylene, diethyl ether (DEE), and acetaldehyde synthesis rates were observed to deactivate to 94%, 74%, and 70% of their initial rates, respectively, after altering the ethanol feed partial pressure to 0.5 mg of $\gamma$-$Al_2O_3$ at 648 K between 0.8 and 5.3 kPa over the course of 7 h (Figure 39). The synthesis rates of ethylene, DEE, and acetaldehyde as a function of ethanol partial pressure in absence of deactivation were evaluated by using a reference condition for each experiment (for the data presented in Figure 39, the

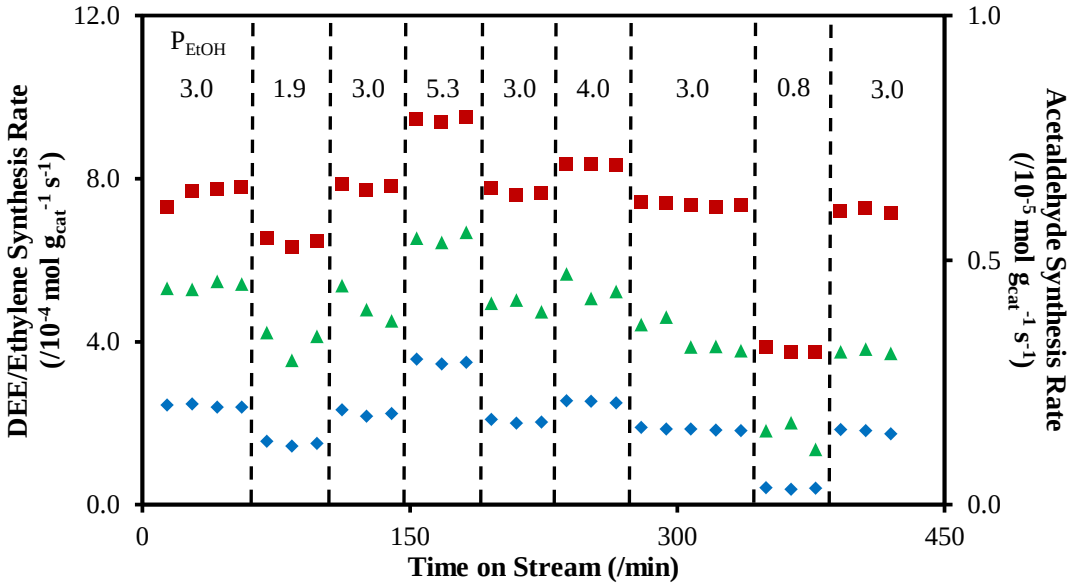


**Figure 39.** Synthesis rates of ethylene (■), DEE (◆), and acetaldehyde (▲) as a function of time on stream and ethanol partial pressure over 0.5 mg of γ-$Al_2O_3$ (total volumetric flowrate = 9.9 $cm^3$ $s^{-1}$) at 648 K with a 0.4 kPa water co-feed. The dotted lines serve as a guide for the eye to separate changes in ethanol partial pressure as a function of time.

reference condition was 3.0 kPa of ethanol in the feed). The reference condition for each experiment was repeated after each other experimental condition (Figure 39). The evaluated rates for each product at an experimental condition were multiplied by the ratio of the synthesis rates evaluated at the first reference condition time range of the experiment and those evaluated at the reference condition time range that immediately followed the experimental condition of interest to determine the synthesis rates in absence of deactivation reported in Figures 11 and 12. For the example given in Figure 39, the rate of DEE synthesis at 5.3 kPa reported in Figure 11 was evaluated by multiplying the measured rate by the ratio of the rates of DEE synthesis at the initial reference 3.0 kPa condition and the third 3.0 kPa condition.

The effect of deactivation on the synthesis rates of the products could also be

accounted for by fitting the deactivation profile of the reference condition with a time-dependent exponential decay function. The synthesis rates of ethylene, DEE, ethane, and acetaldehyde in absence of deactivation would then be estimated using the fitted time-dependent function. The estimated synthesis rates using the reference condition method and the time-dependent exponential decay are within model and experimental error of each other, indicating that either method could be used to determine the synthesis rates in absence of deactivation. The reference condition method was favored in this investigation as it does not assume any deactivation kinetics a-priori.

### 6.3 Analysis of experimental and residual error for ethanol conversion kinetics above 623 K

The large relative errors in Figures 13 and 14 are a result of the difficulty quantifying ethane production in this reaction system. Similarly to acetaldehyde, the concentration of ethane in the effluent (<100 ppm) makes it difficult to distinguish from the baseline noise. Additionally, the GC peak for ethane lies on the tail of the much larger ethylene peak, resulting in a slight overestimate of the quantity of ethane produced. The production of ethane, however, is unlikely to exceed that of acetaldehyde as no other species have been observed in the reactor effluent that would indicate an additional source of hydrogen for either direct or indirect ethylene hydrogenation.

The kinetic models presented in Equations 6-8 for ethylene, DEE, and acetaldehyde syntheses accurately predict the measured synthesis rates relative to the measured experimental error at 648 and 673 K and the synthesis rates of DEE and acetaldehyde at

623 K (Figure 40). The residual errors of each of the models are ordered randomly (Figure 41) and are distributed normally (Figure 42) at 648 and 673 K. While the residual errors for each model are distributed normally at 623 K (Figure 42), the residual errors appear to possess a positive dependence on the previous residual error at 623 K (Figure 41), indicating that at least one systematic error exists in either the experimental procedure or in the model. This is further indicated by the deviations of the experimental data from the model presented in Equation 6 for ethylene synthesis at 623 K (Figures 11 and 40).

One possible source of error in the experimental procedure arises from inconsistencies in weighing and loading catalyst in the reactor. Over the course of the experiments discussed in this study, two batches of catalyst were prepared by pressing and sieving powdered $\gamma$-$Al_2O_3$. The transition from one batch to the next occurred at the beginning of the experimental study when the steady state kinetic measurements at 623 K were collected. While the average mass of an individual pressed and sieved catalyst particle was measured using a balance after preparing each batch of catalyst, individual catalyst particles were counted loaded into the reactor for each experiment (Figure 43). For the kinetic measurements taken at 623 K, the first batch of catalyst was used and possessed a larger variance in particle sizes (180-420 μm) than that of the second batch used for all other kinetic measurements (180-250 μm). The large particle size range of the first batch of catalyst may have led to the catalyst loading in each experimental run to be different, causing a systematic error in the system. The effect of this error seems larger

for ethylene synthesis because of the smaller experimental errors evaluated for this product, making systematic and model errors more pronounced relative to the measured experimental error.

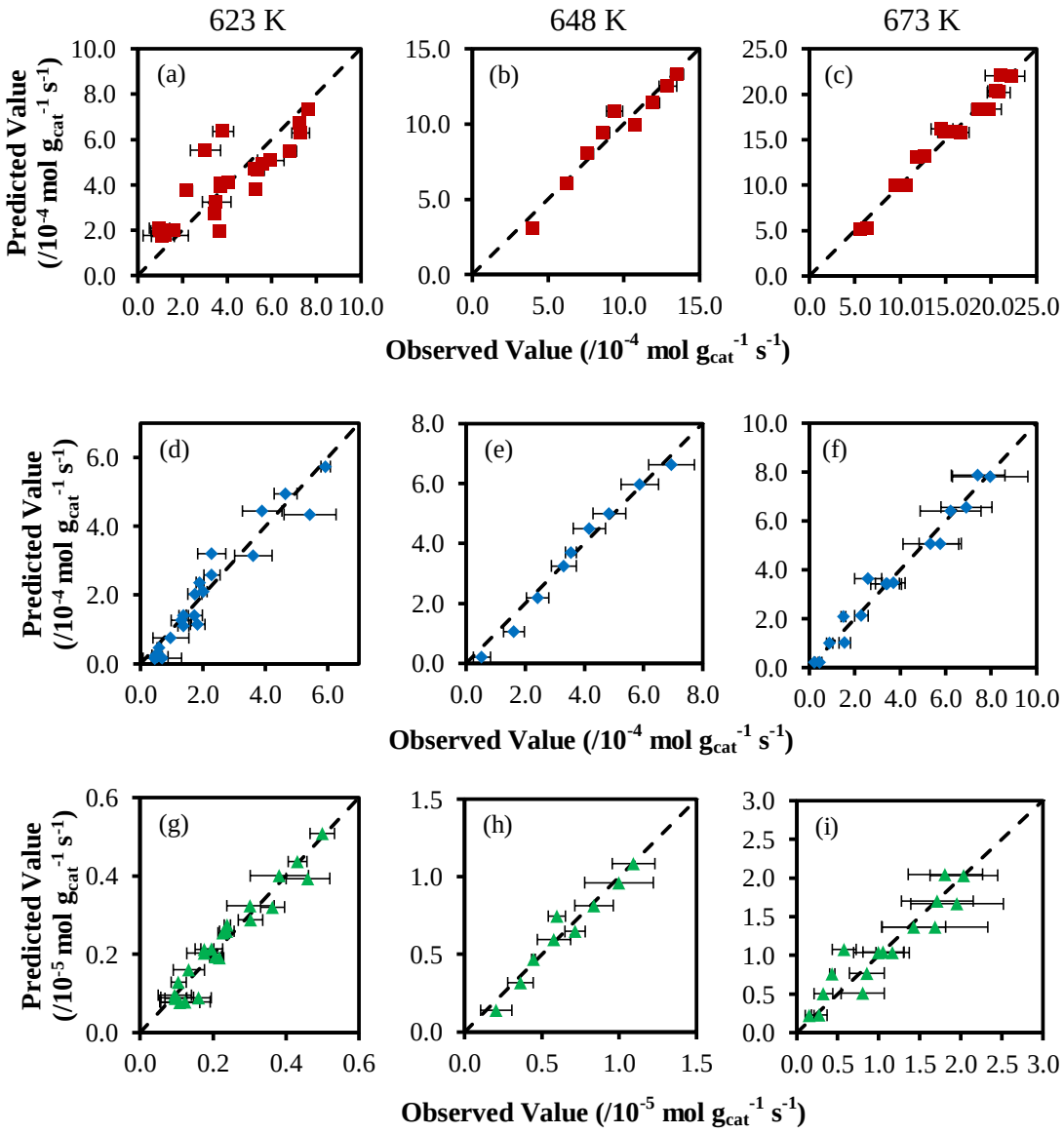


**Figure 40.** Parity plots for the kinetic model for (a-c) ethylene (■), (d-f) DEE (◆), and (g-i) and acetaldehyde (▲) synthesis rates at (a,d,g) 623 K, (b,e,h) 648 K, and (c,f,i) 673 K on γ-$Al_2O_3$ presented in Equations 6-8 and the data presented in Figures 11 and 12. The dotted line represents perfect model prediction.

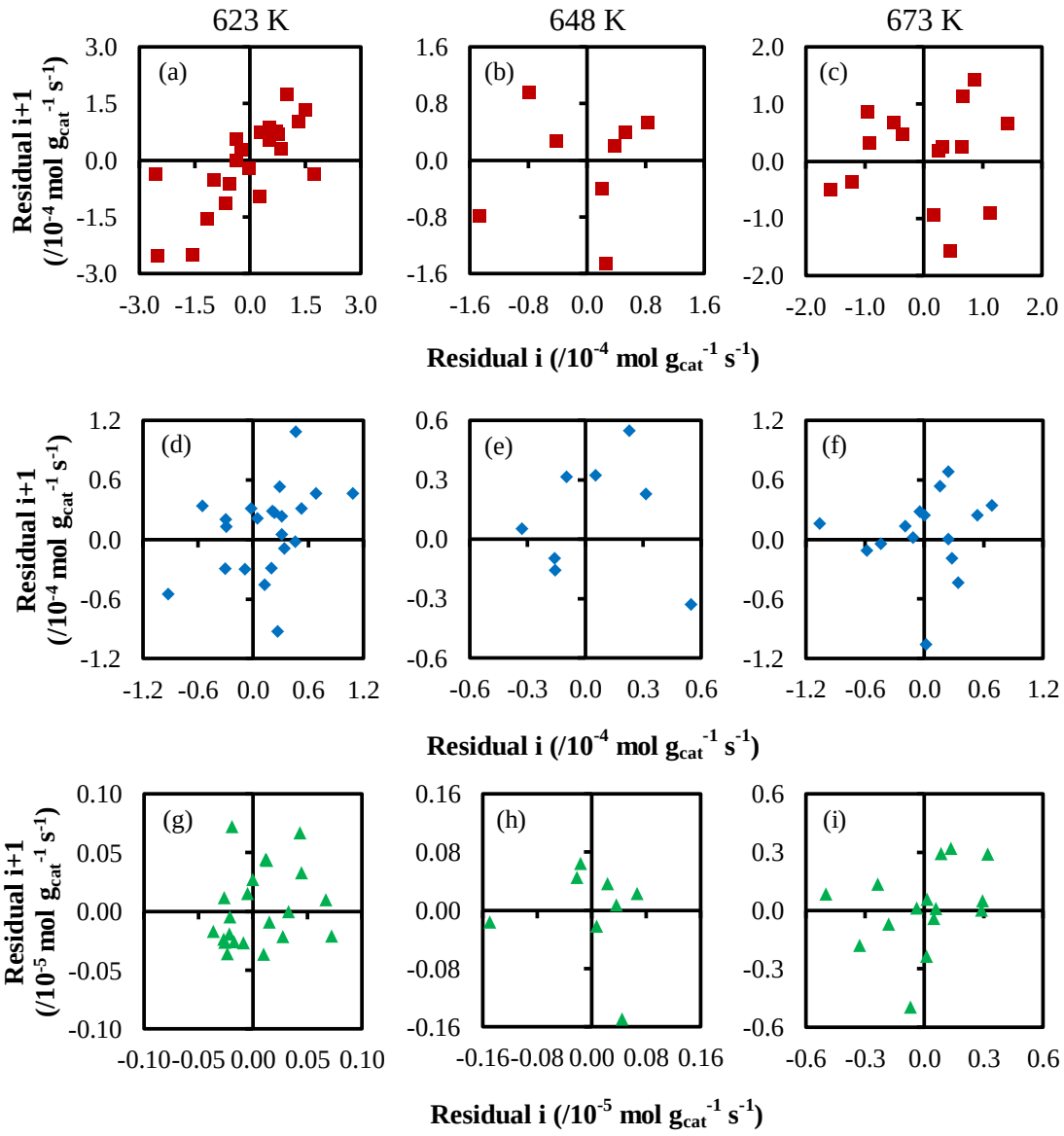


**Figure 41.** Lag plots for residual errors of the kinetic models of Equations 6-8 for (a-c) ethylene (■), (d-f) DEE (◆), and (g-i) acetaldehyde (▲) synthesis rates at (a,d,g) 623 K, (b,e,h) 648 K, and (c,f,i) 673 K on $\gamma$-$Al_2O_3$ relative to the data presented in Figures 11 and 12.

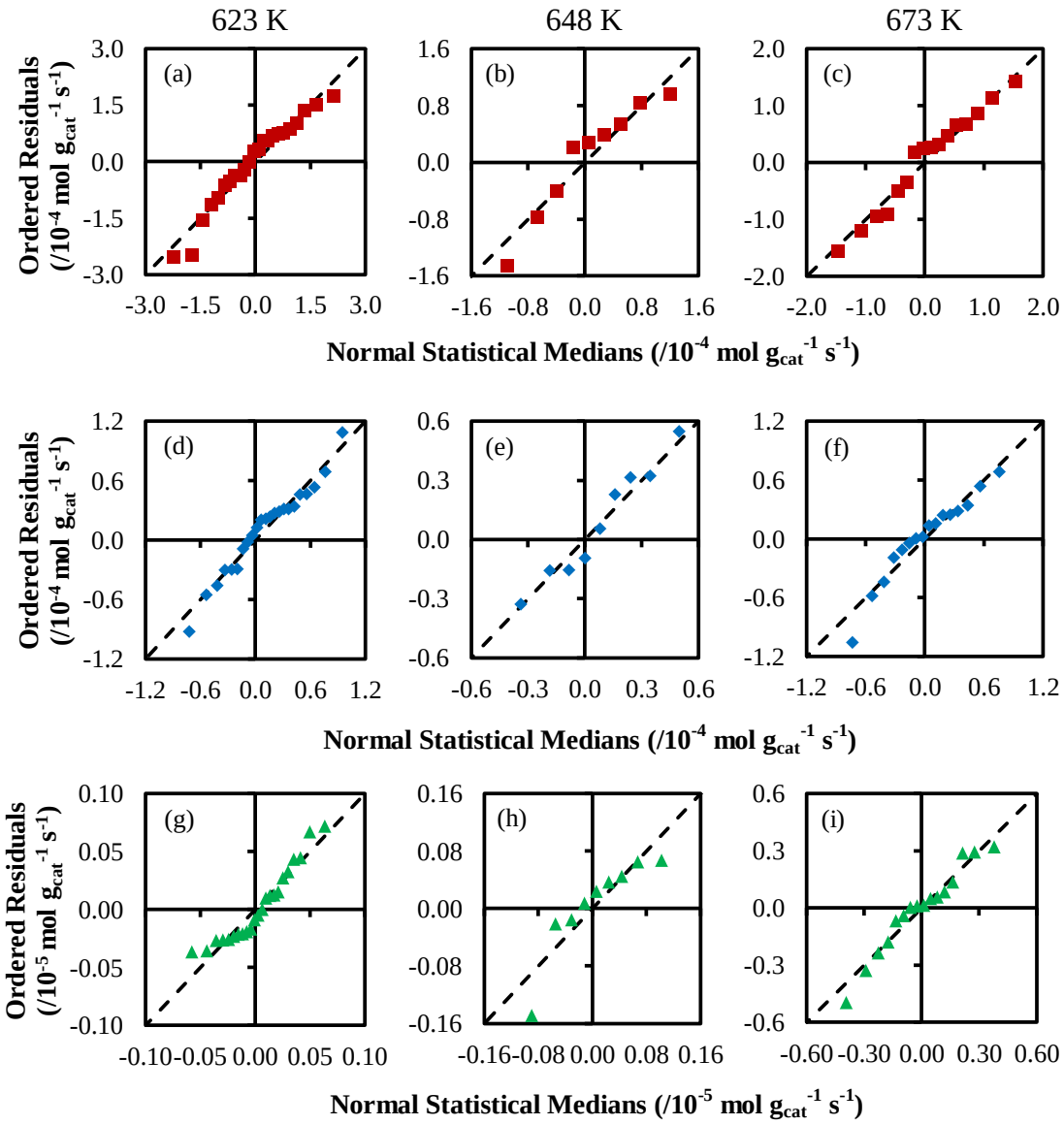


**Figure 42.** Normal probabitlity plots for the residual errors of the kinetic models presented in Equations 6-8 for (a-c) ethylene (■), (d-f) DEE (◆), and (g-i) acetaldehyde (▲) synthesis rates at (a,d,g) 623 K, (b,e,h) 648 K, and (c,f,i) 673 K on $\gamma$-$Al_2O_3$ compared to the data presented in Figures 11 and 12. The dotted lines represent a perfectly normal distribution of residual errors.

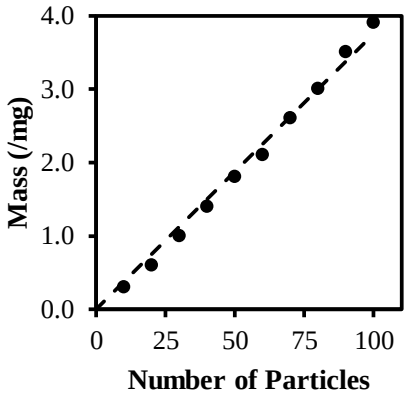


**Figure 43.** Calibration curve used to determine the number of catalyst particles (particle sizes between 180 and 420 μm) needed to achieve the desired catalyst loading in the steady state kinetic measurements presented in Figures 11 and 12. The dashed line shows a linear least squares fit to the data.

### 6.4 Residual error analysis for 1-propanol and methanol dehydration models

The kinetic models for 1-propanol and methanol dehydration on γ-$Al_2O_3$ at 623 K presented in Equations 19 and 20 rigorously describe the steady state kinetic measurements shown in Figures 20 and 21 within experimental error (Figure 44). Additionally, the residual errors of the kinetic models for propylene and DME synthesis possess no dependence on the preceding error (Figure 45a and 45c). Furthermore, the distribution of residual errors for each dehydration model is very close to a perfect normal distribution (Figure 46). The residual errors for the kinetic model for the synthesis of DPE from the dehydration of 1-propanol presented in Equation 20 are positively correlated with the proceeding residual error when the data is ordered in chronological order of acquisition (Figure 45b), indicating that a small systematic error exists in either the model or the experimental data. The data point with the highest residual error in Figure 45b corresponds with the measurement of Figure 20b taken at 2.3 kPa with the

largest range in experimental variance in both measured rate and ethanol partial pressure (represented by the 95 % confidence error bars in Figure 20b). This larger variance is one possible source of experimental systematic error in this system. The model for the synthesis of DPE also appears to under-predict the mean of the experimental measurements shown in Figure 20b, which also contributes to the positive order dependence in Figure 45b; this under-prediction, however, is within experimental variance and, therefore, not indicative of model inaccuracy.

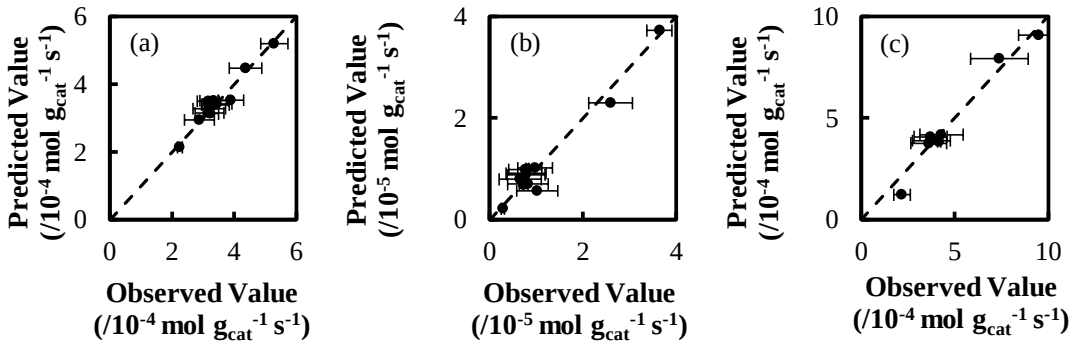


**Figure 44.** Parity plots for the kinetic models for (a) propylene and (b) DPE synthesis from 1-propanol dehydration as well as (c) DME synthesis from methanol dehydration presented in Equations 19 and 20 and the steady state kinetic measurements shown in Figures 20 and 21. Perfect model prediction is shown with the dashed line.

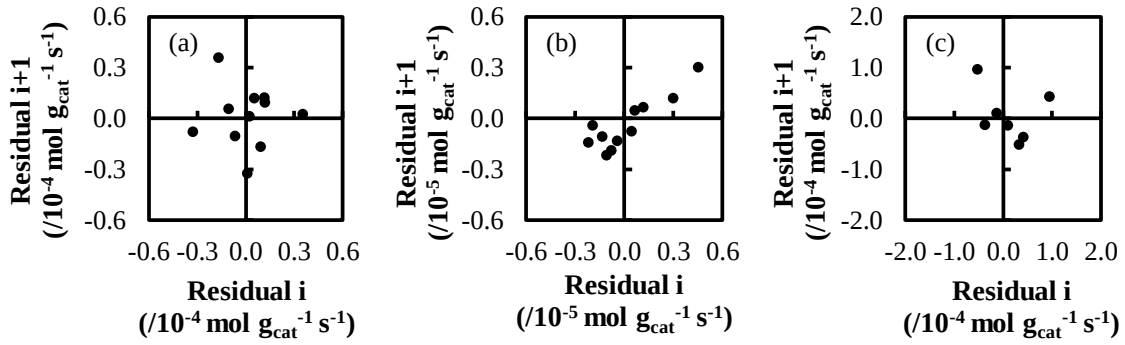


**Figure 46.** Lag plots of the residual errors in the models for the kinetics of (a) propylene and (b) DPE synthesis from 1-propanol dehydration and (c) DME synthesis from methanol dehydration presented in Equations 19 and 20 and the steady state kinetic measurements shown in Figures 20 and 21.

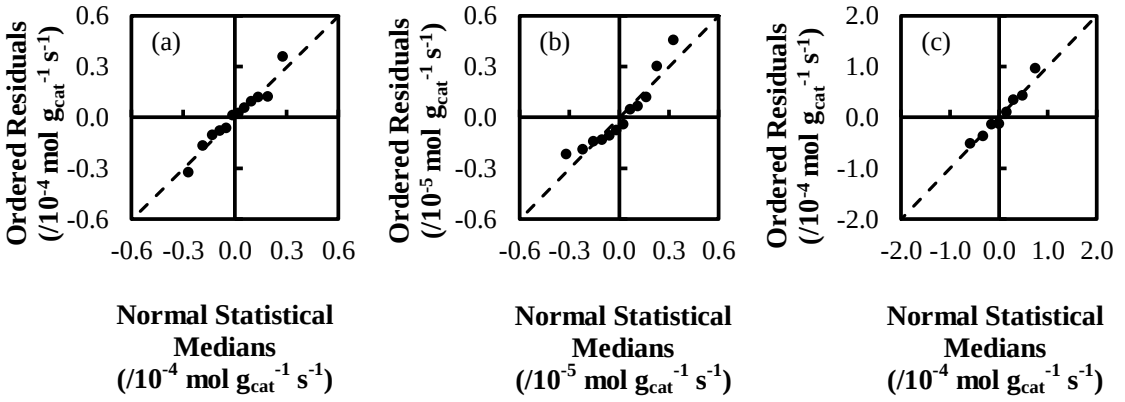


**Figure 45.** Normal probability plots of the residual errors in the kinetic models for (a) propylene and (b) DPE synthesis from 1-propanol dehydration and (c) DME synthesis from methanol dehydration presented in Equations 19 and 20 and the steady state kinetic measurements shown in Figures 20 and 21. A completely normal distribution of residual errors is shown with the dashed line.

### 6.5 Residual error analysis of the kinetic model for DEE disproportionation

The kinetic model for the disproportionation of DEE presented in Equation 21 both accurately describes the measured experimental data (Figure 47a) and possesses residual errors that are normally distributed (Figure 47c). The residual errors appear to possess a

positive dependence to the proceeding residual error (Figure 47b), which would, as with DPE synthesis above, indicate a systematic error. This positive dependence, however, is dominated by a single measured rate with a large experimental error in Figure 23a ($0.65 \times 10^{-4}$ mol $g_{cat}^{-1}$ $s^{-1}$ 95% confidence interval compared to the average $0.15 \times 10^{-4}$ mol $g_{cat}^{-1}$ $s^{-1}$) at 2.0 kPa of DEE that lies above the model prediction. This uncertainty could be a result of fluctuations in the feed solution and, thus, fluctuations in DEE partial pressures and, therefore, may not be representative of the measurement set as a whole.

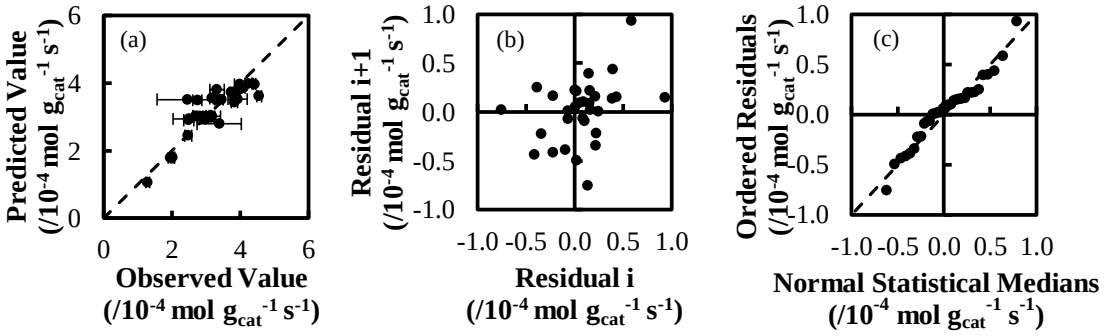


**Figure 47.** (a) Parity plots for the model fit as well as (b) lag and (c) normal probability plots for the residual errors of the kinetic model for DEE disproportionation presented in Equation 21 using the steady state kinetic measurements shown in Figure 23. The dashed lines represent (a) perfect model prediction and (c) a perfectly normal distribution of residual errors.

### 6.6 Induction period of the untreated commercial acrolein oxidation catalyst

The initial acrolein consumption rate over 2.9 mg of an R2 catalyst sample that was not treated in UHP air at 623 K and that did not undergo the 1.0 ks exposure to the R1effluent prior to reaction, as outlined in Section 5.2.3, was 60% larger than other measured rates below 15% acrolein conversion (Figure 48). The larger initial rate compared to rates at similar acrolein pressures (<15% conversion) signifies that the R2 commercial catalyst undergoes a short (<2.4 ks, the data collection frequency) induction period. The initial acrolein consumption rate was only 15% larger than the other measured rates (<15% conversion) in a separate experiment in which the R2 catalyst was exposed to the R1 effluent mixture for 2.0 ks prior to reaction (Figure 48, see Section 5.2.3 for exposure procedure). All data presented in Chapter 5 was, therefore, gathered over a catalyst sample that was exposed to the R1 effluent prior to reaction.

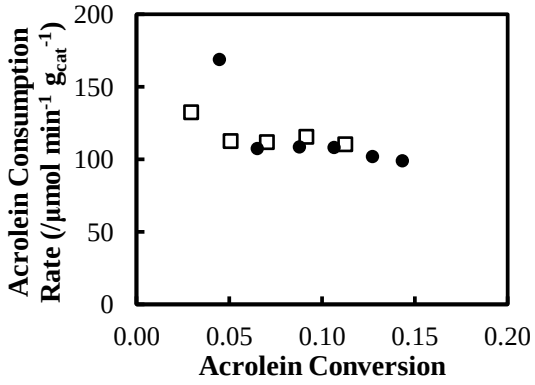


**Figure 48.** Acrolein consumption rate at 498 K and 130 kPa over 2.9 mg of untreated R2 catalyst samples that were (●) not exposed to the R1 effluent prior to reaction and (□) exposed to the R1 effluent for 2.0 ks prior to reaction as a function of acrolein conversion. Feed compositions ranges are listed in Table 13, Section 5.2.3 (inerts: 20 kPa nitrogen, balance He). Rates were determined from three-point linear regressions around each measurement.

## *Chapter 7: Bibliography*


1. Chorkendorff, I.; Niemantsverdriet, J. W. In *Catalyst Supports: Alumina;* Wiley-VCH: **2007**; Vol. 2nd edition, pp 193-195-193-195.

2. Kogel, J. E.; Trivedi, N. C.; Barker, J. M.; Krukowski, S. T., Eds.; In Society for Mining, Metallurgy, and Exploration: Englewood, CO, **2006**; , pp 1568.

3. Morterra, C.; Magnacca, G. *Catal. Today* **1996**, *27*, 497-532.

4. Wischert, R.; Laurent, P.; Copéret, C.; Delbecq, F.; Sautet, P. *J. Am. Chem. Soc.* **2012**, *134*, 14430-14449.

5. Knözinger, H. *Angew. Chem. Int. Ed.* **1968**, *7*, 791-805.

6. Chiang, H.; Bhan, A. *J. Catal.* **2010**, *271*, 251-261.

7. Spivey, J. J.; Dooley, K. M.; Serrano, D. P.; Sousa-Aguiar, E. F.; Tada, M.; Kuhn, J.; Jaras, S. G.; Parvulescu, V.; Matsushima, T.; Murzin, D.; de Klerk, A.The Royal Society of Chemistry: **2011**; Vol. 23, pp 360-349.

8. Huber, G. W.; Iborra, S.; Corma, A. *Chem. Rev.* **2006**, *106*, 4044-4098.

9. Production: Growth is the Norm.*Chemical & Engineering News Archive* **2006**, *84*, 59-68.

10. Greenler, R. G. *J. Chem. Phys.* **1962**, *37*, 2094-2100.

11. de Mourgues, L.; Peyron, F.; Trambouze, Y.; Prettre, M. *J. Catal.* **1967**, *7*, 117-125.

12. Knözinger, H.; Bühl, H.; Ress, E. *J. Catal.* **1968**, *12*, 121-128.

13. Knözinger, H.; Bühl, H.; Kochloefl, K. *J. Catal.* **1972**, *24*, 57-68.

14. Kibby, C. L.; Lande, S. S.; Hall, W. K. *J. Am. Chem. Soc.* **1972**, *94*, 214-220.

15. Knoezinger, H.; Stuebner, B. *J. Phys. Chem.* **1978**, *82*, 1526-1532.

16. Morávek, V.; Kraus, M. *J. Catal.* **1984**, *87*, 452-460.

17. DeCanio, E. C.; Nero, V. P.; Bruno, J. W. *J. Catal.* **1992**, *135*, 444-457.

18. Shi, B. C.; Davis, B. H. *J. Catal.* **1995**, *157*, 359-367.

19. Cai, S.; Sohlberg, K. *J. Mol. Catal. A: Chem.* **2003**, *193*, 157-164.

20. Clayborne, P. A.; Nelson, T. C.; DeVore, T. C. *Appl. Catal. , A* **2004**, *257*, 225-233.

21. Pan, Y.; Liu, C.; Ge, Q. *Langmuir* **2008**, *24*, 12410-12419.

22. Kwak, J.; Mei, D.; Peden, C. F.; Rousseau, R.; Szanyi, J. *Catal. Lett.* **2011**, *141*, 649-655.

23. Roy, S.; Mpourmpakis, G.; Hong, D.; Vlachos, D. G.; Bhan, A.; Gorte, R. J. *ACS Catal.* **2012**, *2*, 1846-1853.

24. Gabrienko, A. A.; Arzumanov, S. S.; Toktarev, A. V.; Stepanov, A. G. *J. Phys. Chem. C* **2012**, *116*, 21430-21438.

25. Kovarik, L.; Genc, A.; Wang, C.; Qiu, A.; Peden, C. H. F.; Szanyi, J.; Kwak, J. H. *J. Phys. Chem. C* **2013**, *117*, 179-186.

26. Kalló, D.; Knözinger, H. *Chem. Ing. Tech.* **1967**, *39*, 676-680.

27. Kieffer, R.; Hinderman, J. P.; El Bacha R.; Kiennemann, A.; Deluzarche, A. *React. Kinet. Catal. Lett.* **1982**, *21*, 17-21.

28. Chokkaram, S.; Srinivasan, R.; Milburn, D. R.; Davis, B. H. *J. Mol. Catal. A: Chem.* **1997**, *121*, 157-169.

29. Joubert, J.; Delbecq, F.; Sautet, P. *J. Catal.* **2007**, *251*, 507-513.

30. Skinner, M. J.; Michor, E. L.; Fan, W.; Tsapatsis, M.; Bhan, A.; Schmidt, L. D. *ChemSusChem* **2011**, *4*, 1151-1156.

31. Chavez Diaz, C. D.; Locatelli, S.; Gonzo, E. E. *Zeolites* **1992**, *12*, 851-857.

32. Fang, Z.; Wang, Y.; Dixon, D. A. *J. Phys. Chem. C* **2015**, *119*, 23413-23421.

33. Phung, T. K.; Lagazzo, A.; Rivero Crespo, M. Á; Sánchez Escribano, V.; Busca, G. *J. Catal.* **2014**, *311*, 102-113.

34. Knözinger, H.; Köhne, R. *J. Catal.* **1966**, *5*, 264-270.

35. Phung, T. K.; Busca, G. *Chem. Eng. J.* **2015**, *272*, 92-101.

36. Lippens, B. C.; De Boer, J. H. *Acta Crystallogr.* **1964**, *17*, 1312-1321.

37. Levin, I.; Brandon, D. *J. Am. Ceram. Soc.* **1998**, *81*, 1995-2012.

38. Pinto, H. P.; Nieminen, R. M.; Elliott, S. D. *Phys. Rev. B* **2004**, *70*, 125402.

39. Langer, V.; Křestan, J.; Smrčok, L. *Acta Crystallogr. Sect. C* **2006**, *62*, i83-i84.

40. Lee, M. -.; Cheng, C.; Heine, V.; Klinowski, J. *Chem. Phys. Lett.* **1997**, *265*, 673-676.

41. Digne, M.; Sautet, P.; Raybaud, P.; Euzen, P.; Toulhoat, H. *J. Catal.* **2002**, *211*, 1-5.

42. Digne, M.; Sautet, P.; Raybaud, P.; Euzen, P.; Toulhoat, H. *J. Catal.* **2004**, *226*, 54-68.

43. Parry, E. P. *J. Catal.* **1963**, *2*, 371-379.

44. Ripmeester, J. A. *J. Am. Chem. Soc.* **1983**, *105*, 2925-2927.

45. Christiansen, M. A.; Mpourmpakis, G.; Vlachos, D. G. *J. Catal.* **2015**, *323*, 121.

46. Knözinger, H.; Ratnasamy, P. *Catal. Rev.* **1978**, *17*, 31-70.

47. Morterra, C.; Cerrato, G.; Meligrana, G. *Langmuir* **2001**, *17*, 7053-7060.

48. Wischert, R.; Copéret, C.; Delbecq, F.; Sautet, P. *Angew. Chem. Int. Ed.* **2011**, *50*, 3202-3205.

49. Hendriksen, B. A.; Pearce, D. R.; Rudham, R. *J. Catal.* **1972**, *24*, 82-87.

50. Slade, R. C. T.; Southern, J. C.; Thompson, I. M. *J. Mater. Chem.* **1991**, *1*, 563-568.

51. Cesteros, Y.; Salagre, P.; Medina, F.; Sueiras, J. E. *Chem. Mater.* **1999**, *11*, 123-129.

52. Winfeild, M. E.; Emmet, P. H.Reinhold In *Catalysis*, NY, **1960**; Vol. VII.

53. Coster, D.; Blumenfeld, A. L.; Fripiat, J. J. *J. Phys. Chem.* **1994**, *98*, 6201-6211.

54. Liu, X.; Truitt, R. E. *J. Am. Chem. Soc.* **1997**, *119*, 9856-9860.

55. Soled, S. L.; McVicker, G. B.; Murrell, L. L.; Sherman, L. G.; Dispenziere Jr., N. C.; Hsu, S. L.; Waldman, D. *J. Catal.* **1988**, *111*, 286-295.

56. Baertsch, C. D.; Komala, K. T.; Chua, Y.; Iglesia, E. *J. Catal.* **2002**, *205*, 44-57.

57. Kwak, J. H.; Hu, J. Z.; Kim, D. H.; Szanyi, J.; Peden, C. H. F. *J. Catal.* **2007**, *251*, 189-194.

58. Kwak, J. H.; Peden, C. H. F.; Szanyi, J. *J. Phys. Chem. C* **2011**, *115*, 12575-12579.

59. Pines, H.; Haag, W. O. *J. Am. Chem. Soc.* **1961**, *83*, 2847-2852.

60. Knözinger, H.; Scheglila, A. *J. Catal.* **1970**, *17*, 252-263.

61. Zotov, R. A.; Molchanov, V. V.; Volodin, A. M.; Bedilo, A. F. *J. Catal.* **2011**, *278*, 71.

62. Knözinger, H.; Scheglila, A.; Watson, A. M. *J. Phys. Chem.* **1968**, *72*, 2770-2774.

63. Zecchina, A.; Bordiga, S.; Spoto, G.; Scarano, D.; Spano, G.; Geobaldo, F. *J. Chem. Soc. Faraday Trans.* **1996**, *92*, 4863-4875.

64. Kostestkyy, P.; Yu, J.; Gorte, R. J.; Mpourmpakis, G. *Catal. Sci. Technol.* **2014**, *4*, 3861-3869.

65. DeWilde, J. F.; Chiang, H.; Hickman, D. A.; Ho, C. R.; Bhan, A. *ACS Catalysis* **2013**, *3*, 798-807.

66. Jenness, G. R.; Christiansen, M. A.; Caratzoulas, S.; Vlachos, D. G.; Gorte, R. J. *J. Phys. Chem. C* **2014**, *118*, 12899-12907.

67. Christiansen, M. A.; Mpourmpakis, G.; Vlachos, D. G. *ACS Catal.* **2013**, *3*, 1965-1975.

68. Shimizu, K.; Kon, K.; Shimura, K.; Hakim, S. S. M. A. *J. Catal.* **2013**, *300*, 242.

69. Nondek, L.; Sedláček, J. *J. Catal.* **1975**, *40*, 34.

70. Li, M.; Wu, Z.; Overbury, S. H. *J. Catal.* **2013**, *306*, 164.

71. Amenomiya, Y.; Chenier, J. H. B.; Cvetanovic, R. J. *J. Catal.* **1967**, *9*, 28-37.

72. Wischert, R.; Florian, P.; Copéret, C.; Massiot, D.; Sautet, P. *J. Phys. Chem. C* **2014**, *118*, 15292-15299.

73. Dabbagh, H. A.; Zamani, M.; Davis, B. H. *J. Mol. Catal. A: Chem.* **2010**, *333*, 54-68.

74. Schiffino, R. S.; Merrill, R. P. *J. Phys. Chem.* **1993**, *97*, 6425-6435.

75. Matyshak, V. A.; Berezina, L. A.; Sil'chenkova, O. N.; Tret'yakov, V. F.; Lin, G. I.; Rozovskii, A. Y. *Kinet. Catal.* **2009**, *50*, 111-121.

76. DeWilde, J. F.; Czopinski, C. J.; Bhan, A. *ACS Catal.* **2014**, *4*, 4425-4433.

77. Kang, M.; DeWilde, J. F.; Bhan, A. *ACS Catal.* **2015**, *5*, 602-612.

78. Zecchina, A.; Platero, E. E.; Areán, C. O. *J. Catal.* **1987**, *107*, 244-247.

79. Busca, G. In *Chapter Three - Structural, Surface, and Catalytic Properties of Aluminas;* Friederike C. Jentoft, Ed.; Academic Press: **2014**; Vol. 57, pp 319.

80. Bauer, W. In *Acrylic Acid and Derivatives;* Seidel, A., Bickford, M., Eds.; John Wiley & Sons, Inc: **2000**; Vol. 1, pp 342-369.

81. Kampe, P.; Giebeler, L.; Samuelis, D.; Kunert, J.; Drochner, A.; Haab, F.; Adams, A. H.; Ott, J.; Endres, S.; Schimanke, G.; Buhrmester, T.; Martin, M.; Fuess, H.; Vogel, H. *Phys. Chem. Chem. Phys.* **2007**, *9*, 3577-3589.

82. Grand View Research Inc *Acrylic Acid Market Analysis, by Product (Acrylate Esters, Glacial Acrylic Acid), by End-use (Surfactants and Surface Coatings, Organic Chemicals, Adhesives, Textiles, Water Treatment, Personal Care Products), Bio Acrylic Acid Downstream Potential and Segment Forecasts to 2022*. **September 2015**.

83. Devaux, J. F.; Dubois, J. L. Arkema, France Patent US 2013/0324758 A1, **2013**.

84. Dubois, J. L. PA, United States Patent US 2009/0018362 A1, **2009**.

85. Tichy, J. *Appl. Catal. , A* **1997**, *157*, 363.

86. Grzybowska, S. *Top. Catal.* **2000**, *11*, 23-42.

87. Sadakane, M.; Watanabe, N.; Katou, T.; Nodasaka, Y.; Ueda, W. *Angew. Chem. Int. Ed.* **2007**, *46*, 1493-1496.

88. Charendorff, M.; Juliette, J. J.; Mendoza, J.; Shah, R. PA, United States Patent US 2013/0281737 A1, **2013**.

89. Chen, C.; Kosuke, N.; Murayama, T.; Ueda, W. *ChemCatChem* **2013**, *5*, 2869-2873.

90. Qiu, C.; Chen, C.; Ishikawa, S.; Murayama, T.; Ueda, W. *Top. Catal.* **2014**, *57*, 1163-1170.

91. Andrushkevich, T. V. *Catal. Rev. Sci. Eng.* **1993**, *35*, 213-259.

92. Tichy, J.; Machek, J.; Svachula, J. *React. Kinet. Catal. Lett.* **1984**, *25*, 231-235.

93. Dieterle, M.; Petzoldt, J.; Muller-Engel, K.; Arnold, H. VA, United States Patent Pub. No.: US 2004/0192963 A1, **2004**.

94. Andrushkevich, T. V.; Plyasova, L. M.; Kuznetsova, G. G.; Bondareva, V. M.; Gorshkova, T. P.; Olenkova, I. P.; Lebedeva, N. I. *React. Kinet. Catal. Lett.* **1979**, *12*, 463-467.

95. Davydov, A. A.; Kuznetsova, T. G.; Andrushkevich, T. V. *React. Kinet. Catal. Lett.* **1986**, *30*, 173-178.

96. Kuznetsova, T. G.; Andrushkevich, T. V.; Gorshkova, T. P. *React. Kinet. Catal. Lett.* **1986**, *30*, 149-156.

97. Ovsitser, O.; Uchida, Y.; Mestl, G.; Weinberg, G.; Blume, A.; Jager, J.; Dieterle, M.; Hibst, H.; Schlogl, R. *J. Mol. Catal. A: Chem.* **2002**, *185*, 291.

98. DeGroot, P. B.; Levy, L. B. *J. Catal.* **1982**, *76*, 393.

99. Machek, J.; Svachula, J.; Tichy, J. In *Selective Oxidation of Aldehydes over V-Mo-Ox/SiO2 Catalysts;* Cortes Corberan, V., Vic Bellon, S., Eds.; Elsevier Science: **1994**; pp 845-852.

100. Vogel, H.; Bohling, R.; Hibst, H. *Catal. Lett.* **1999**, *62*, 71-78.

101. Tichy, J.; Svachula, J.; Machek, J.; Allachverdova, N. C. *React. Kinet. Catal. Lett.* **1986**, *31*, 159-166.

102. Erenburg, E. M.; Andrushkevich, T. V.; Popova, G. Y.; Davydov, A. A.; Bondareva, V. M. *React. Kinet. Catal. Lett.* **1979**, *12*, 5-11.

103. Kolosov, A. K.; Shvets, V. A.; Kazansky, V. B. *Chem. Phys. Lett.* **1975**, *34*, 360.

## Biography

I was born in Corvallis, OR to Janice, a clerk, and Francis DeWilde, an electrician, in March of 1989. After living in Valemount, British Columbia for a few years, we returned to Albany, OR in 1993, where I spent the majority of my childhood. I attended South Albany High School in 2003 where I discovered my affinity toward mathematics and the sciences and where my interest in engineering, in particular chemical engineering, was sparked. I graduated from high school in 2007 and planned to immediately pursue a career in engineering.

Directly after graduating high school, I attended Linn-Benton Community College to start my educational path toward a career in chemical engineering. Later, I would receive my Bachelor's degree in Chemical Engineering from Oregon State University. During the summer of my junior year of my undergraduate education, I received my first opportunity to perform research at the University of Minnesota under Professor Andreas Stein through the National Nanotechnology Infrastructure Network REU program. In this research experience, I investigated techniques for the production of thermally-stable photonic crystals. This experience led me to further my education by pursuing my Doctorate at the University of Minnesota.

Over my last 5 years here, I have grown as a scientist, created a network of friends and colleagues, and, most importantly, met my current wife, Esha. I will fondly look back at everything my time here has provided me. Moving forward, I will be working as a research scientist at The Dow Chemical Company in Midland, MI where I will be focusing on the design and development of industrial reactor systems.